Design and Characterization of Microfabricated Three-Dimensional Millimeter-Wave Components

by

Kenneth J. Vanhille

B.S., Utah State University, 2002

M.S., University of Colorado, 2005

A thesis submitted to the

Faculty of the Graduate School of the

University of Colorado in partial fulfillment

of the requirements for the degree of

Doctor of Philosophy

Department of Electrical and Computer Engineering

2007

This thesis entitled:
Design and Characterization of Microfabricated Three-Dimensional Millimeter-Wave Components
written by Kenneth J. Vanhille
has been approved for the Department of Electrical and Computer Engineering

Prof. Zoya Popović

Prof. Dejan Filipović

Date

The final copy of this thesis has been examined by the signatories, and we find that both the content and the form meet acceptable presentation standards of scholarly work in the above mentioned discipline.

Vanhille, Kenneth J. (Ph.D., Electrical Engineering)

Design and Characterization of Microfabricated Three-Dimensional Millimeter-Wave Components

Thesis directed by Prof. Zoya Popović

This thesis presents the analysis, design, and measurement of air-filled millimeter-wave rectangular coaxial components microfabricated on 150-mm silicon wafers. There is currently considerable interest in the application of new fabrication techniques for the implementation of classical microwave devices to improve performance while reducing size. In addition, the enabling of the design of novel, heretofore unrealizable devices is of interest. The air-filled transmission lines presented in this thesis have advantages over traditional planar transmission lines in that they are non dispersive, possess high isolation, are amenable to dense integration and sharp turn radii, are low loss for their cross section, and are much smaller than rectangular or circular metallic waveguides for a given frequency. As an example, a 50-Ω line with a 250 μm by 250 μm cross section has the first higher order mode starting at 450 GHz, the losses are 0.22 dB/cm at 26 GHz, and the isolation between two adjacent lines with a center-to-center separation of 300 μm is better than 60 dB/cm. In a multi-layer configuration, vias and crossovers with excellent broadband performance are quite naturally implemented. Millimeter-wave designs on both the component and subsystem levels are of interest.

Air-filled, copper rectangular coax lines and devices with cross sections between 125 μm by 300 μm and 630 μm by 700 μm are fabricated by Rohm and Haas Electronic Materials LLC according to designs from this thesis. The research focus is the development of usable, high-quality millimeter-wave components which demonstrate the merits of this technology. *Ka*-band components have been designed, fabricated, and tested. Scaling in frequency has been investigated up to *W*-band, and the presently used fab-

rication process could conceivably be used at frequencies into the hundreds of GHz. Connections to probe-based test equipment and standard circuit lines are designed. A method of de-embedding the probe structures of four-port data using the two-port TRL model is developed and shown to agree with simulations.

Among other components, this thesis presents the design and comprehensive analysis of half-wave metallic cavity resonators fabricated using this technology. To the best of the author's knowledge, the measured quality factor of these resonators comes closer to the theoretical maximum than those of other microfabricated TE_{101} cavity resonators operating above 10 GHz. Branch line couplers with compensation of the reactances of the associated T junctions are designed for operation at 36 GHz, fabricated and measured. Several other components have been fabricated, including directional couplers, high-repeatability probe structures, and Lange couplers.

Dedication

to Vanessa, James, Ellie, and eternity together

Acknowledgements

I wish to thank the many wonderful people that I have worked with around the lab and everywhere else.

I am grateful to Zoya Popović for her support, direction, encouragement and example. I also appreciate Dejan Filipović and his complete dedication to the cause. The following names are not necessarily in order, but are all important. A special thank you to Milan Lukić, my office mate and friend; Jacques Loui, for his zest for life and research; Patrick Bell, for his willingness to call the kettle black, Nestor Lopez, for his genuine intellectual curiosity; Charles Dietlein, for his not-so-useless trivia; John O'Brien for his good-natured ability to put up with me; Milos Jankovic and the funky bunch; Sébastien Rondineau, whose sneaking around makes me laugh; and Yongjae Lee, my fellow family man. A big thanks to the rest of the group members, Jarka Hladisova, Adam Sadoff, and Rachael Tearle.

This has been an undertaking by a very many people in a very many places. Therefore, I would be remiss to neglect mentioning several of the most important people from several of our most important collaborators. This work has been supported by DARPA under the 3-D MERFS program and Rohm and Haas Electronic Materials, LLC. A special thanks is due Dan Fontaine and those individuals at BAE Systems who have helped make this possible, including Gil Potvin. Some of the data presented here was collected by them in their laboratories. Chris Nichols, David Sherrer, Jean-Marc Rollin and the Rohm and Haas Microfabrication team deserve a big thanks and

congratulations. Without them, I'd just have a bunch of marginally interesting electromagnetic models. It's a stretch, but without me, they might just have a bunch of copper. Wendy Wilkins and the Mayo measurement team have been extremely helpful with their measurement capabilities for some of the data that is presented here.

Finally, I appreciate the support and love of my parents and family. I am grateful to Grandpère who has made the financial struggle of a grad student with a family a little less of a struggle. I must thank Anna Hughes for her friendship to my family during our time in Boulder.

Contents

Chapter

Tables

Table

Figures

Figure

Chapter 1

Introduction

Rectangular coaxial transmission lines (rectacoax) have several interesting properties that have made them an enabling technology for the development of high-performance millimeter-wave systems. The losses in the lines are lower than traditional millimeter-wave transmission lines such as microstrip and CPW. Another benefit of these transmission lines is single-mode TEM operation to 450 GHz for a 50-Ω transmission line whose cross section is 250 μm by 250 μm [1]. These lines are also highly isolated, as the outer conductor is a natural shield for the fields contained within the transmission line. Two 50-Ω transmission lines with a shared 70-μm wall and small holes between the lines for the fabrication process have isolation of better than 60 dB/cm at 26 GHz. These benefits will be further quantified in Section 1.1. The important dimensions of a rectacoax transmission line are indicated in Figure 1.1(a).

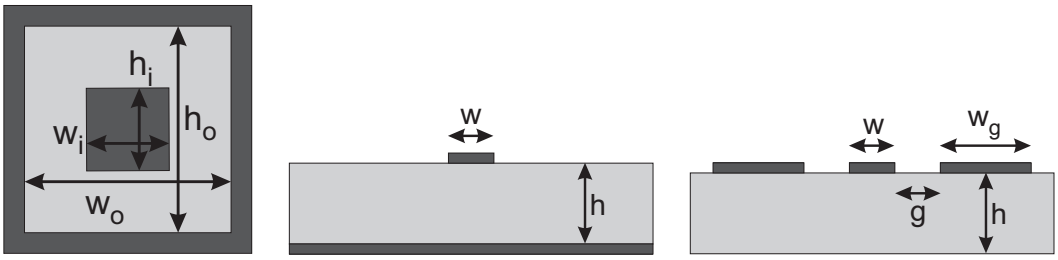

Figure 1.1: The cross sections of (a) the rectacoax, (b) the microstrip, and (c) the coplanar waveguide. The values of the dimensions in Table 1.1 correspond to the dimensions indicated in this figure.

Microfabricated rectacoax lines have been the subject of several recent research thrusts [2–6], although previous work for rectangular coaxial transmission lines fabricated using classical machining for satellite beam forming networks in the *C*- and *Ku*-bands exists [7, 8]. Air-filled copper-plated transmission lines of several varieties, including rectacoax, with measured performance to 40 GHz are presented in [2]. Thick-metal surface micromachining for air-filled transmission lines in a CMOS compatible process are presented in [3]. Devices fabricated using nickel with more than 40 layers are reported in [4]. Other attempts have been made to laser-machine each metal layer of the coaxial lines and assemble all the layers together to form the device [5]. In [6], motions toward a CMOS compatible process for the fabrication of air-filled rectacoax lines are presented, however the full structure has not been demonstrated. The center conductor is perforated to provide customize characteristic impedances and is supported using periodic polyimide columns.

Microfabrica, Van Nuys, California, has developed a microfabrication technique named the Electrochemical Fabrication Process, EFAB$^{\text{TM}}$ [4, 9, 10]. This process uses layer-by-layer deposition of a series of structural and sacrificial metals, reaching layer counts near 40. Upon completion of the deposition, the sacrificial metal is etched away and air-metal structures remain. Many millimeter-wave devices have been fabricated using this method [4, 10–17]. One of the main drawbacks of this technology has been the fact that nickel has been used as the structural material, having a relatively low conductivity, ($\sigma = 1.74e7S/m$). Recent work has been done to electroplate a thin layer of gold on the walls ($\sigma = 4.5e7S/m$), giving better loss performance [17].

The PolyStrata$^{\text{TM}}$ process, developed by Rohm and Haas Electronic Materials, is another method of microfabricating rectacoax. Advantages of this fabrication process compared to the previously mentioned techniques include the use of copper structural metal for low losses, the ability to integrate dielectric support straps with the process, and the ability to deposit thick layers (tens of microns).

The outline of the remainder of this chapter is as follows.

- Section 1.1 discusses some of the reasons for using rectacoax. A comparison is made with other millimeter-wave transmission-line technologies and theoretical limits of rectacoax are discussed.
- The fabrication process used for the PolyStrata^{TM} devices is described in Section 1.2.
- The organization of the ensuing chapters of the dissertation is outlined in Section 1.3.

1.1 Properties of Rectacoax

A treatise extolling the virtues of a particular transmission-line medium may be more appropriately contained within the quasi-philosophical musings of Prof. Thomas H. Lee [18, 19], however there are several properties of rectacoax that make it advantageous compared to traditional millimeter-wave transmission lines such as microstrip and coplanar waveguide. A few of the properties that are of interest are the low-loss characteristics, the dispersion of the transmission line, the isolation measured between adjacent lines, and the ready integrability into multilayer environments. These parameters will be examined for rectacoax, microstrip, and coplanar waveguide, as shown in Figure 1.1.

The size of microstrip lines used for signal routing in MMICs is often dependent on the intended operating frequency. Some flexibility exists for transmission lines intended for *Ka*-band operation with thicknesses of 50 μm and 100 μm [20, 21], among others. Gallium Arsenide (GaAs) MMICs operating at *V*-band are often built on 100-μm GaAs wafers [22]. At *W*-band, 50-μm GaAs wafers are standard for MMICs [23, 24]. Many other microstrip configurations exist, but these sizes will be adequate to see general trends.

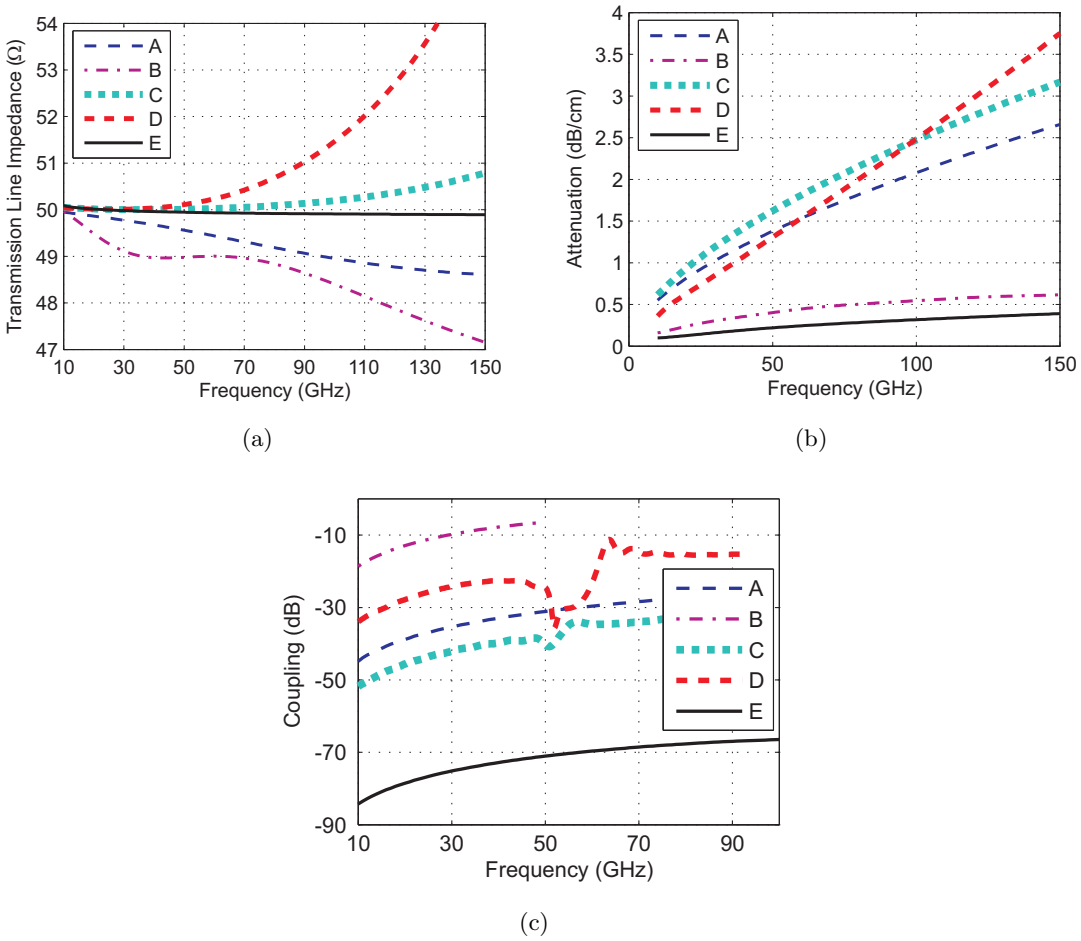

Figure 1.2: The (a) characteristic impedance, (b) attenuation/cm, and (c) coupling over 1 cm for center-to-center line spacings of 700 μm for several microstrip, coplanar waveguide, and rectacoax lines are compared. Table 1.1 describes the geometries used to create the curves presented here.

Table 1.1: The dimensions in microns (corresponding to Figure 1.1) for the transmission lines that are compared in Figure 1.2.

Microstrip									
A	w	34	–	–	–	–	h	50	GaAs
B	w	144	–	–	–	–	h	200	GaAs
Coplanar Waveguide									
C	w	40	g	23	w_g	86	h	125	GaAs
D	w	140	g	60	–	–	h	200	Alumina
Rectacoax									
E	w_i	100	w_o	250	h_i	100	h_o	250	Air

The dimensions of coplanar waveguide transmission lines are slightly less standardized, as the center conductor and gaps are chosen somewhat independently of the substrate thickness. A *V*-band subharmonic mixer fabricated on GaAs is designed using finite-ground coplanar waveguide with the dimensions of C in Table 1.1 [25]. A *W*-band coplanar waveguide on alumina uses coplanar waveguide with the dimensions of D in Table 1.1 [26].

The rectacoax cross section that is used for comparison is a 50-Ω transmission line as used in the five-layer rectacoax wafers that have been fabricated, and are described in Section 1.2. The first higher order mode for this transmission line has a cutoff frequency at 450 GHz. The measured loss at 26 GHz for these lines is 0.22 dB/cm.

Figure 1.2 shows a comparison of the characteristic impedance, attenuation, and isolation with respect to frequency for the five transmission line geometries in Figure 1.1 with the dimensions in Table 1.1. A and B are two microstrip dimensions, C is coplanar waveguide with finite ground widths, D is coplanar waveguide with infinite ground widths and E is rectacoax with 200 μm release holes with a periodicity of 700 μm. The attenuation of Figure 1.2(b) does not include dielectric losses, which would give larger losses for transmission lines A-D, while not significantly altering those of E. The coupling in Figure 1.2(c) is calculated using the Moment Method in Ansoft Designer for A-D. Ansoft HFSS is used to calculate the coupling for the rectacoax. It is seen that B is the only transmission line that has nearly the same losses as the rectacoax, yet the isolation is less than 10 dB above 30 GHz. Rectacoax provides the best results for optimizing both attenuation and isolation.

It is worth taking further examination of the loss mechanisms in coaxial transmission lines for the purpose of highlighting the advantage of air-filled coaxial cable over that of coaxial cable with a dielectric, lossless or otherwise. We start with the per-unit-length equations for the transmission-line parameters of a circular coaxial cable [27]:

$$R' = \frac{R_s}{2\pi}\left(\frac{1}{a}+\frac{1}{b}\right) \tag{1.1}$$

$$L' = \frac{\mu}{2\pi}\ln(\ b/a) \tag{1.2}$$

$$G' = \frac{2\pi\sigma}{\ln(b/a)} \tag{1.3}$$

$$C' = \frac{2\pi\epsilon}{\ln(b/a)} \tag{1.4}$$

where a is the outer radius of the inner conductor and b is the inner radius of the outer conductor, R_s is the surface resistivity, and σ is the conductivity of the fill dielectric. We also know that the general formulas for the complex propagation constant, γ, and the characteristic impedance, Z_0, of a transmission line are

$$\gamma = \sqrt{(R'+j\omega L')\,(G'+j\omega C')} \tag{1.5}$$

$$Z_0 = \sqrt{\frac{(R'+j\omega L')}{(G'+j\omega C')}} \tag{1.6}$$

Assuming the losses due to the dielectric and conductors are small (G', $R' \simeq 0$), the phase constant is

$$\beta = \omega\sqrt{L'C'} \tag{1.7}$$

Now, we will make the assumption that we have a perfect dielectric and G'=0. The attenuation constant, α, is

$$\alpha = \frac{\sqrt{\pi\epsilon f}}{2\sqrt{\sigma_c}}\left(\frac{1}{a}+\frac{1}{b}\right)\frac{1}{\ln b/a} \tag{1.8}$$

We are interested in the lowest possible per-unit-length attenuation for a given size of coax. For a given Z_0 and b, we are thus interested in sweeping ϵ_r, calculating a based on these values, and finding the α. Using Eq. 1.6 and Eq. 1.8 with the values defined in Eq. 1.1 – Eq. 1.4, the value of a is

$$a = \frac{b}{\exp\left(\frac{2\pi Z_0\sqrt{\epsilon}}{\sqrt{\mu}}\right)} \tag{1.9}$$

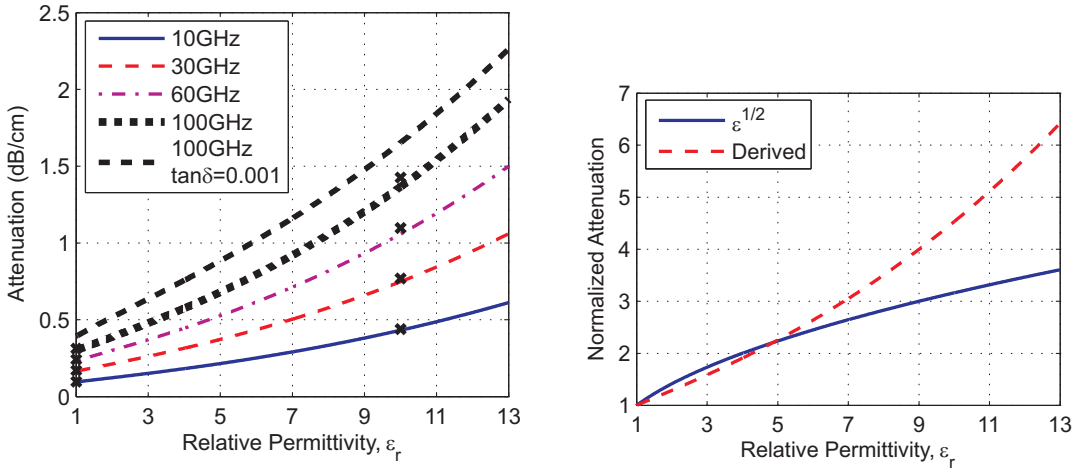

(a) (b)

Figure 1.3: (a) The losses of circular coax are shown for a 1-cm length of line. The diameter of the outer conductor is 250 μm and the relative permittivity is swept, while changing the inner diameter to maintain 50 Ω. 10, 30, 60 and 100 GHz are shown with one curve for 100 GHz with a loss tangent ($\tan\delta$) of 0.001. Comparison with HFSS is made for ϵ_r=1,10 for validation. (b) Comparison of Eq. 1.10 to $\sqrt{\epsilon_r}$ is made. This shows that the losses do not scale with $\sqrt{\epsilon_r}$ – the losses do not simply scale up proportionally to the electrical length of the line scaling down as ϵ_r increases.

Figure 1.3(a) shows the attenuation at four frequencies for relative permittivities between 1 and 13. These are calculated using the real part of Eq. 1.5 Eq. 1.9. Eq. 1.8 is not used because we also examine dielectric losses at 100 GHz. We have HFSS data marked with 'x' as validation.

We are now interested in understanding how α relates to the relative permittivity. Inserting Eq. 1.9 into Eq. 1.8 and substituting in the intrinsic impedance of free space, $\eta_0 = \sqrt{\mu_0/\epsilon_0}$, we see the relation between α and ϵ_r is

$$\alpha \propto \exp\left(\frac{2\pi Z_0\sqrt{\epsilon_r}}{\eta_0}\right) + 1 \tag{1.10}$$

Figure 1.3(b) provides interesting insight into the behavior of the added losses as the dielectric, even lossless dielectric, is introduced into the coaxial line. A first reaction might be to believe the loss is simply originating from the shortening of the electrical length of the line so that if the physical size of $\sqrt{\epsilon_r}\times length$ shrinks, the losses scale proportionally. We see that this is not the case and the actual dependence is also influenced by the characteristic impedance of interest.

Although the examination of the losses in a circular coaxial transmission line has been presented, these conclusions are extendible to rectacoax. Specific frequency behavior may change with different dimensions and characteristic impedances, but the general trends hold. For a given physical length of transmission line we have seen that the isolation and attenuation for a given size are best using air-filled rectacoax.

1.2 PolyStrata^{TM} Fabrication

The PolyStrata^{TM} process, developed by Rohm and Haas Electronic Materials, consists of sequentially depositing layers of metal and photoresist with high aspect ratios (2:1) [28]. Current design procedures have the rectacoax components fabricated on a

low-resistivity silicon substrate using a sequence of standard photolithographic steps, as depicted in Figure 1.4. The requirement for the host substrate upon which the devices are fabricated is only that it be flat. Low-resistivity silicon is used for the devices reported in [29, 30]. High-resistivity silicon is used for the devices reported in [31, 32]. The copper layer thicknesses range from 10 μm to 100 μm. The fabrication is conducted following the steps outlined in Figure 1.4. The copper is electroplated in $S1$ to a height greater than the required layer height and then, using chemical-mechanical polishing (CMP), the layer is planarized to the desired height. In $S2$, the negative photoresist is spun onto the wafer, and exposed with the corresponding mask. An etchant is then used to remove the photoresist where the copper will then be electroplated. The copper is electroplated to a level above the photoresist and CMP is used to planarize the photoresist and copper as shown in $S3$. A layer for the polymer straps is spun on, patterned, and selectively etched, leaving periodically-placed 18-μm-tall dielectric straps for the support of the rectacoax center conductors ($S4$). This process continues until the final step, $S11$ or Sn, which involves removing the remaining photoresist, leaving a wafer filled with air-filled millimeter-wave components whose center conductors are supported with dielectric straps. The fill ratio of dielectric to air is less than 0.5% for most transmission lines.

Devices fabricated using wafer runs with five- and ten-metal-layer processes (depicted in Figure 1.4) have been designed and characterized. The layer thicknesses used in the five-layer process are 10 μm, 75 μm, 100 μm, 75 μm, and 50 μm. A 50-Ω transmission line with these layers has a center conductor that is 100 μm by 100 μm with a 75 μm gap on the top, bottom, and sides. The 10-layer process allows more flexibility for the design of the transmission lines. Dimensions are shown in Figure 1.5 for the most commonly used transmission lines. 35.4-Ω transmission lines are used for the branch-line couplers described in Chapter 4.

A few examples of devices fabricated with the PolyStrata$^{\mathrm{TM}}$ process are shown in

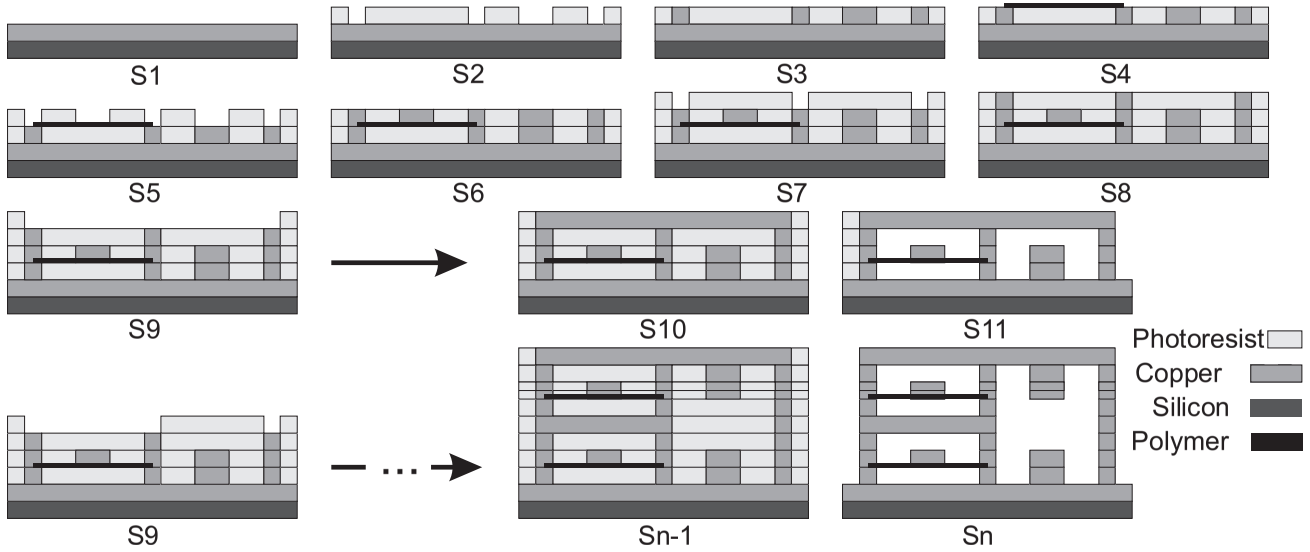

Figure 1.4: Basic fabrication steps for the PolyStrata^{TM} process. Many potential devices are possible using this process, among them are the transmission lines and loaded resonator cross sections shown here. The first nine steps ($S1$–$S9$) are identical for the five-layer and ten-layer structures.

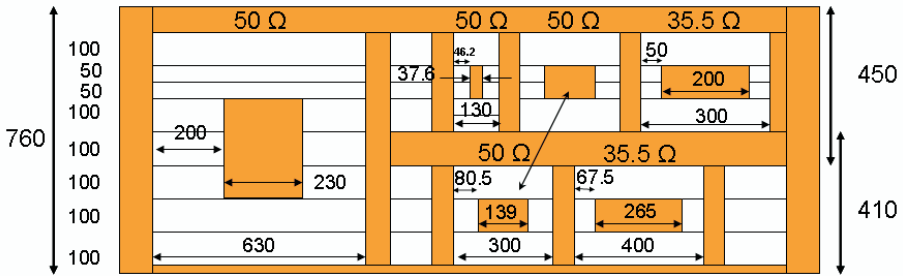

Figure 1.5: The dimensions of several of the transmission lines used in the 10-layer fabrication process.

Figure 1.6. The scale is indicated for each of the photographs. An SEM image is shown in Figure 1.6(a) for several devices fabricated using the five-layer process, including branch-line couplers, cavity resonators, and isolation test structures. A photograph of two pairs of branch-line couplers operating at 36 GHz is shown in Figure 1.6(b). Each pair of branch-line couplers share release holes, yet 50 dB isolation is maintained between the stacked couplers over the frequency band of interest. A 4-port Butler matrix is shown in Figure 1.6(c), implemented using rectacoax. The probing structures for the four input and output ports on either side of the coupler are visible. 200 μm by 100 μm wide columns of copper permeate the visible wafer to decrease stresses caused by large uninterrupted tracts of photoresist during the fabrication process.

For further references containing work employing the PolyStrata^{TM} fabrication process the reader is referred to the following sources. The modeling of some of the effects of realistic non-idealities in the transmission-line cross section such as under- and over-etching of the layers is analyzed in [1]. The effects of two-dimensional surface roughness, both transverse to and with the direction of current flow, on losses and the propagation constant are examined in [33]. The first attempts at the analysis of three-dimensional surface roughness using 3-D finite element method (FEM) is presented in [34]. Several rectacoax devices are presented in [32]. [31] contains the performance results of a few high-Q quasi-planar cavity resonators that are compatible with this

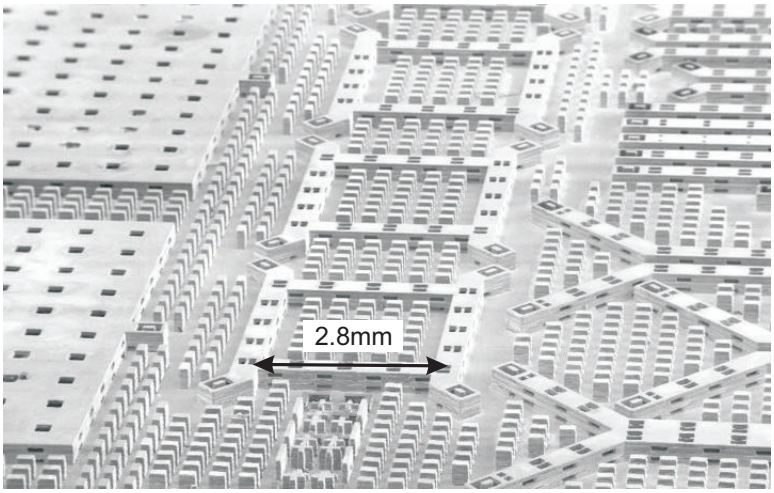

(a)

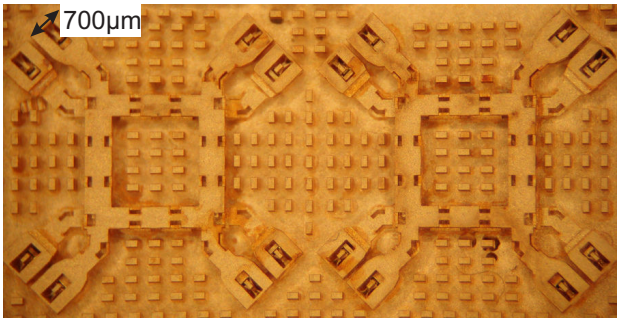

(b)

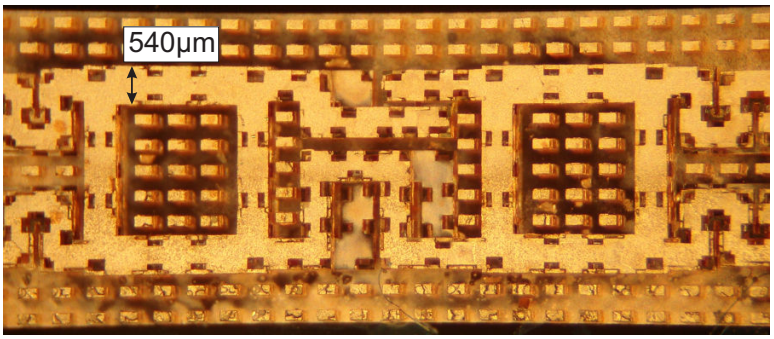

(c)

Figure 1.6: Three images of fabricated devices are shown. (a) Several branch-line couplers, resonators, and isolation measurement structures fabricated with a 5-layer process for operation at 26 GHz. (b) A photograph of two sets of branch-line couplers that have been fabricated using the 10-layer process. (c) A photograph of a feed network to demonstrate a four-input-to-four-output Butler matrix operating at 36 GHz. ((a) © 2006 Rohm and Haas Electronic Materials, LLC.)

technology. Further exploration of the possibilities for resonator miniaturization using the PolyStrata^{TM} technology is initiated in [35] and more fully developed in [29]. The parasitic reactances of rectacoax tee junctions are mitigated using two forms of compensation to produce balanced branch-line couplers [30]. Antenna elements designed for array applications at 36 GHz are presented in [36, 37]. The focus of this thesis includes some of the aforementioned work as well as other, previously unpublished designs.

1.3 Dissertation Organization

With an introduction to the motivation for this work, a description of the microfabricated transmission lines, and an outline of the fabrication process, the analysis and characterization of 3-D microwave and millimeter-wave microfabricated devices will be presented.

General methods of analysis and a broad description of measurement techniques are presented in Chapter 2. The vector network analyzer (VNA) is the primary piece of equipment used to measure these devices. A discussion regarding the calibration is provided. Additionally, some comments about the modeling of these devices are also given.

The topologies of seven metallic cavity resonators are presented in Chapter 3. Cavity resonators are fabricated for operation at 26 GHz and 36 GHz. Allowance for robust mechanical designs are made through the use of support posts for the large top cavity wall. Miniaturization using several loading schemes is presented.

The focus of Chapter 4 is the design, analysis and measurement of 90° hybrids fabricated using the PolyStrata^{TM} process. Branch-line couplers using common design techniques are presented as a baseline approach. The performance of these couplers is limited by the transmission line tee-junctions inherent in branch-line designs. Compensated branch-line couplers are presented to solve this problem. These are the first compensated tee-junctions for microfabricated rectangular coax. Lange couplers are

also designed, fabricated and presented as another method of improving performance. 10- and 20-dB directional couplers are designed using similar techniques to those used for the Lange coupler and the provided measurements verify the design process.

In Chapter 5 the design and modeling for a 3-D opto-electronic package for optical communication is presented. This design demonstrates the fluidity with which the design techniques used for PolyStrata^{TM} devices can be employed for other microwave and millimeter-wave systems.

The concluding chapter, Chapter 6, provides a summary of the presented work, presents initial ideas for a few new designs and extensions to the previous chapters, and discusses avenues for future work.

Chapter 2

Simulation and Measurement Background

The analysis and measurement techniques used to characterize the 3-D micro-fabricated components will be presented in this chapter. A brief description of the numerical analysis methods is presented in Section 2.1. As the measurement analysis is not unique for each classification of components, all of the employed techniques will be presented here, and the remaining chapters will focus on the underlying electromagnetic behavior and results of the fabricated devices. A description of the structures used to probe the wafer is given in Section 2.3.

2.1 Pertinent Numerical Analysis Methods

Transmission lines and millimeter-wave components fabricated using rectacoax and other fabrication process compatible technologies are labor intensive to design and analyze. The combined effects of release holes, sharp corners, inhomogeneous transmission line cross sections, and a high ratio between feature sizes requires a robust method of analysis [32]. These result in computationally intensive models, so simplifying assumptions are used wherever possible. Parameters such as the characteristic impedance (Z_0) and the complex propagation constant (γ) are calculated using 2-D methods when possible. Circuit models are derived in Section 3.6 to further simplify analysis.

Quasi-analytical numerical implementations of the Schwarz-Christoffel conformal mapping transformation (SCCM) for doubly- and singly-connected geometries are uti-

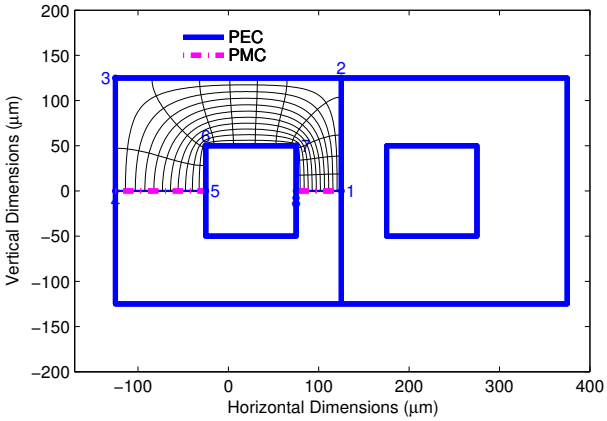

(a) Center PEC Symmetry

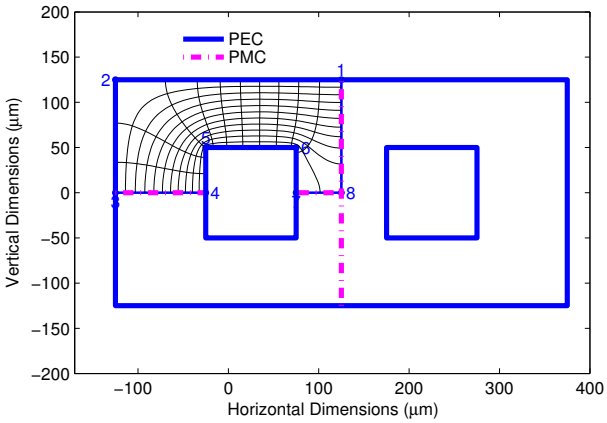

(b) Center PMC Symmetry

Figure 2.1: Two examples of the implementation of the SCCM for the calculation of the even- and odd-mode impedances for coupled lines with the field lines plotted (a) PEC and (b) PMC center line.

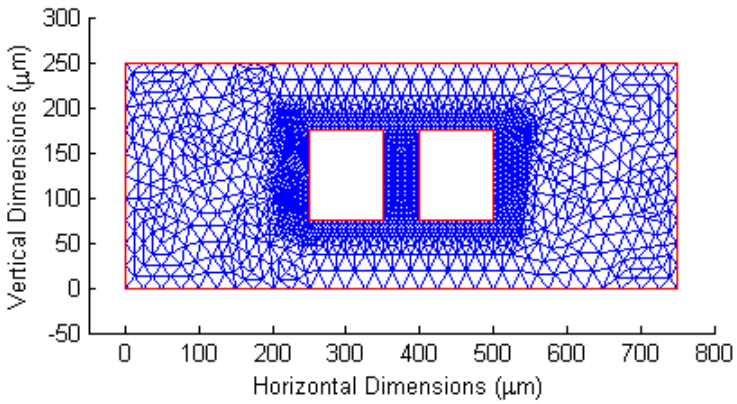

Figure 2.2: An example mesh created using COMSOL *Multiphysics* to solve the quasi-static solution for a pair of coupled center conductors in a rectacoax transmission line is shown.

lized in [1] for the analysis of rectacoax lines. Part of this formulation is implemented with the Schwarz-Christoffel MATLAB toolbox created by Driscoll [38]. The quasi-static approximation is used in this situation because the transmission line cross section is electrically small and the frequencies of interest are well below that of the first higher order mode supported by the transmission line [39]. With these tools, one is able to transform the transmission-line cross section to a parallel-plate waveguide and calculate the capacitance per unit length. From here, the characteristic impedance are calculated. Using Wheeler's incremental inductance rule, one is able to solve for the per-unit-length attenuation of the transmission line [40]. Numerical conformal mapping can also be used to solve for the even- and odd-mode impedances for different cross sections of transmission lines, although symmetry in both of the cross-sectional dimensions is necessary. Figure 2.1 shows examples used to calculate the even- and odd-mode impedances for a pair of coupled lines. It is only necessary to solve a quarter of the geometry because of symmetry. The coupled lines used to design the Lange coupler of Section 4.4 do not have the required symmetry to employ this technique.

For coupled transmission-line cross sections without symmetry, transmission-line

cross sections containing inhomogeneous dielectric fillings, and other more complicated transmission line cross sections, one is required to employ methods other than SCCM. A two-dimensional FEM solver is used in HFSS to solve the fields for the cross section of the wave ports; however, it does not allow full flexibility for the control of all of the parameters in which one may be interested. The 2-D FEM capabilities of COMSOL *Multiphysics* are used for various problems such as these. An example mesh for a 2-D coupled-line problem is shown in Figure 2.2. Again, quasi-static analysis is used for these lines. The capability to use the eigen-mode solver to solve for the modes exists, though has not been employed.

Over the years, many methods of analyzing rectangular coaxial transmission lines using 3-D techniques have been exploited. The branch-line coupler has been a common point of embarking for the demonstration of several 3-D analysis methods. A field-matching technique is developed for both 2-D and 3-D discontinuities [41]. A combination of the finite element method with mode matching is used for a three-branch directional coupler in [42]. In [43], this technique is extended to other discontinuities. A formulation of the FDTD is used in [7]. Currently, the combination of the flexibility of the 3-D FEM and the computing power of modern computers seems to be a good match for the analysis of rectangular coaxial transmission lines [4, 11, 32].

The finite element method is used for the analysis of the devices presented here because of its robust ability to handle arbitrary shapes and material parameters. Two-dimensional and three-dimensional formulations are employed where one or the other lends itself to being the preferred method. These, and similar, full-wave methods are necessary when canonical solutions do not exist for the analytical solution of the desired boundary value problems [44]. Typically, one has a computational domain, Ω, enclosed by a boundary, Γ, over which a solution is desired. The governing operator equation is

of the form

$$L\mathbf{\Phi} = f \tag{2.1}$$

where L is an operator (this is the heart of the governing equation, whether it is Poisson's equation, the Helmholtz equation, or otherwise), $\mathbf{\Phi}$ is the unknown quantity of interest, and f is the excitation. Several methods exist for the solution of such an equation, the scope of which is beyond our immediate discussion. It is sufficient to mention that two of the most common methods used to solve this equation (the methods of Galerkin and Rayleigh-Ritz) involve an understanding of functions that can be used to represent the actual solution over the computational domain. Computationally-efficient large-domain techniques exist, in which the fields are approximated using higher-order equations [45]. This notwithstanding, the majority of interest has been in representing the problem using simpler functions and discretized the computational domain into many subdomains [44, 46].

We are interested in solutions to two classifications of Eq. 2.1 [47]. The first involves foreknowledge of L and f, in situations where we know the governing operator and the sources, and we wish to find the fields everywhere, $\mathbf{\Phi}$. These problems will be solved using the driven analysis in HFSS. The other problems of interest are those involving the non-trivial solution to homogeneous partial differential equations (PDEs) where $g = 0$, eigenvalue problems of the form

$$[\mathbf{A}]\mathbf{\Phi} - \lambda[\mathbf{M}]\mathbf{\Phi} = 0 \tag{2.2}$$

Here, $[\mathbf{A}]$ and $[\mathbf{M}]$ are known and λ and $\mathbf{\Phi}$ are unknown. For a given eigenvalue, λ, there is a solution $\mathbf{\Phi}$ which represents the corresponding eigenvector. For resonant cavities, like those in Chapter 3, λ represents the resonant frequencies of the cavity and $\mathbf{\Phi}$ is the field structure of the corresponding resonant modes.

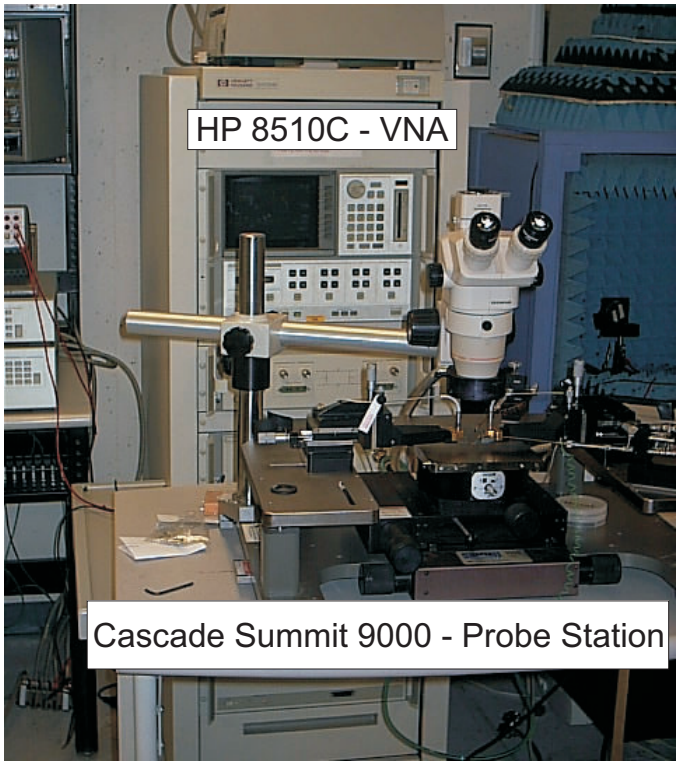

Figure 2.3: A photograph of the HP 8510C vector network analyzer with the Cascade Microtech Summit 9000 probe station used at the University of Colorado.

2.2 Measurement Techniques

The majority of the measurements associated with this thesis are conducted using standard microwave and millimeter-wave laboratory equipment. At the University of Colorado a Hewlett-Packard 8510C network analyzer with a Cascade Microtech Summit 9000 probe station is used. With this equipment, S-parameters analysis to 110 GHz is possible; however, currently some of the probe station W-band adapters are not available at the University of Colorado, so measurements are conducted using coaxial connections to 50 GHz.

Other measurements have been conducted at BAE Systems, Nashua, NH. The Mayo Clinic, Rochester, MN, has conducted four-port network analyzer measurements and some of the data presented in Chapter 4 are from measurements acquired using

equipment in these two locations. The calibration for the four-port measurements is performed using a two-tier method to be described in Section 2.4.1.

2.3 Connections to Non-Microcoax Components

The method of connecting the rectangular coaxial devices to other circuits and measurement equipment determines the accuracy with which the devices can be characterized. This connection should be repeatable and robust. Two methods have been developed, and are presented here.

The current method of measuring these devices uses probing structures that provide locations for microwave probes to contact the devices using a probe station. Probe transitions to several transmission lines of varying dimensions are designed. A simpler model, using the structures shown in Figure 3.5(a) for $R1$-$R5$, is the first design iteration developed for measurement using probes. This design presents a drawback because the center conductor is stabilized using a direct connection of the center conductor to the host substrate, as seen in Figure 3.5(a) and Figure 3.5(b). To provide proper electromagnetic performance, it is necessary to open the bottom wall around the center conductor to electrically isolate the inner and outer conductors. Depending on the requirement for the isolation between adjacent transmission lines, coupling through the substrate between holes will create stronger levels of coupling between two transmission lines than the shared release holes of a common center wall. A design without holes to the substrate is necessary to properly test the isolation between two lines without the coupling of the probing structures contaminating the measurement.

Sketches of four probe transitions for the 10-layer process from Figure 1.4 are shown in Figure 2.4. A 150-μm pitch probe, ground-signal-ground connection to the rectangular coax is shown in Figure 2.4(e). Transparencies in the outer walls of the sketches show the internal features of the probe structures. The center conductor rests on a metallic "seat" that serves to mechanically stabilize the center conductor when the

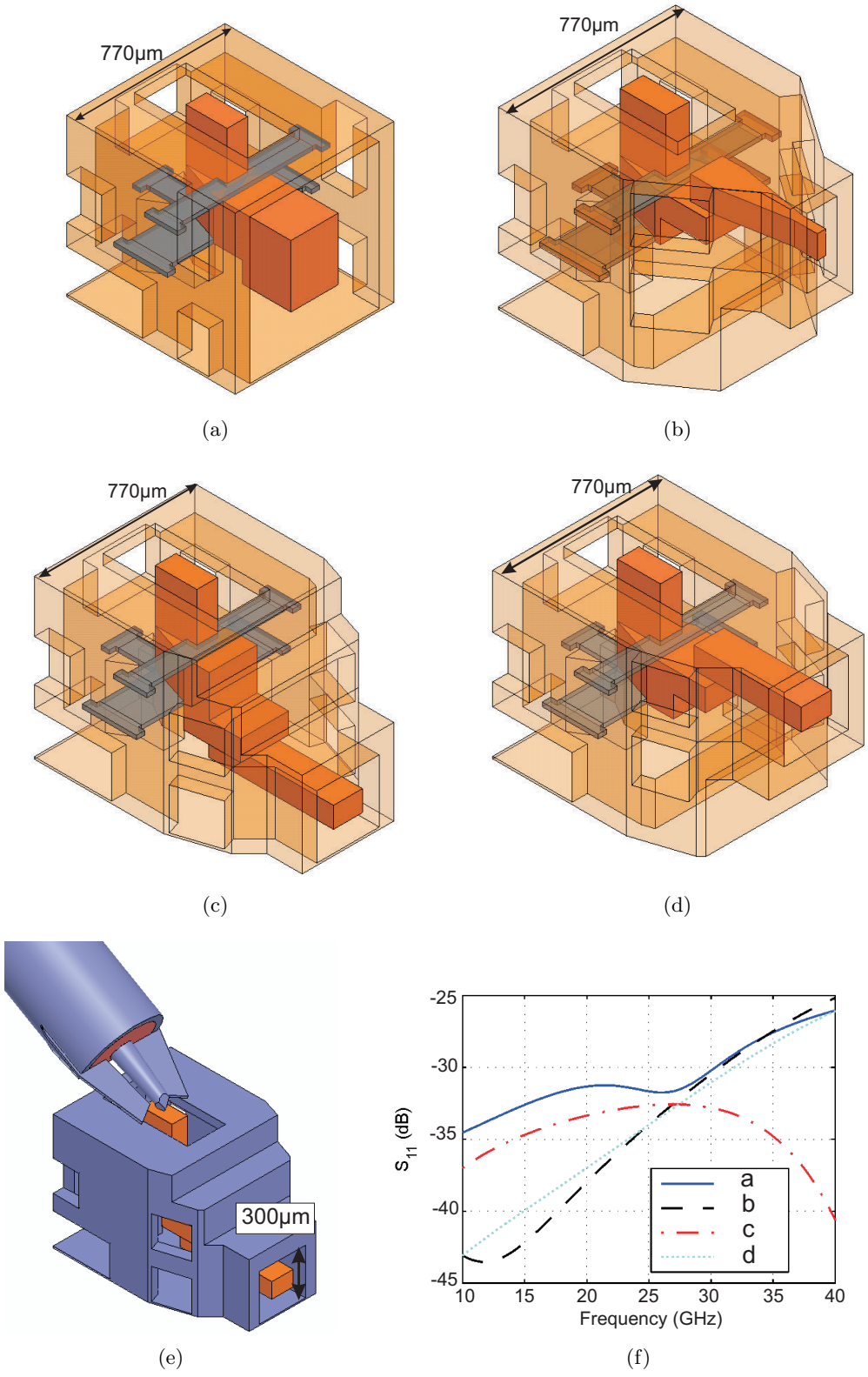

Figure 2.4: Sketches of the transition to (a) 300-μm-wide rectacoax on the bottom layer, (b) 300-μm-wide rectacoax on the top layer, (c) 125-μm-wide rectacoax on the top layer, and (d) 630-μm-wide rectacoax. (e) Sketch of a test probe landing on a probe structure. (e) Simulated results of S_{11} for the probe transitions.

devices are probed. Two dielectric supports are used to position the center conductor in the proper location for probing and isolate the center conductor from the metallic "seat." Release holes are large enough to evacuate the photoresist, while contributing little to the losses of the probe transition. The shape of the center conductor and outer conductor has been tapered where necessary to provide the desired electromagnetic behavior. To the greatest extent possible, a single interface has been designed which can adapt to any of the four 50-Ω line geometries desired with the ten-layer process. This provides flexibility for the designer to have bigger transmission lines when lower loss is desired, lines on top of each other when stacked designs are desired, and narrow lines when dense integration is desired.

2.4 Calibration

Off-wafer calibration is done using either the it Short-*Open-Load-Through* method (SOLT) or the *Line-Reflect-Match* method (LRM) on an alumina substrate, since on-wafer microcoax calibration standards were not initially fabricated. The resulting calibration is flawed because the subsequent measurement of the rectacoax involves connection to air-filled coaxial transmission lines instead of CPW on alumina. The probe-to-transition interaction is fundamentally different and can be compensated using an understanding of the parasitics developed using measurements of the discontinuity [48] or 3-D simulations [49]. On-wafer calibration using such techniques as the *Thru-Reflect-Line* method (TRL) can overcome this problem [50]. Deembedding the probe-launch interaction enables accurate characterization of the fabricated devices independent of the measurement method.

The on-wafer methods, such as the TRL method, are advantageous in cases such as ours where the transition from the network analyzer to the rectacoax structures is not well understood. The TRL error formulation is an 8-term model, as opposed to the 12-term model which has 6 terms used for the forward path (excitation of port 1

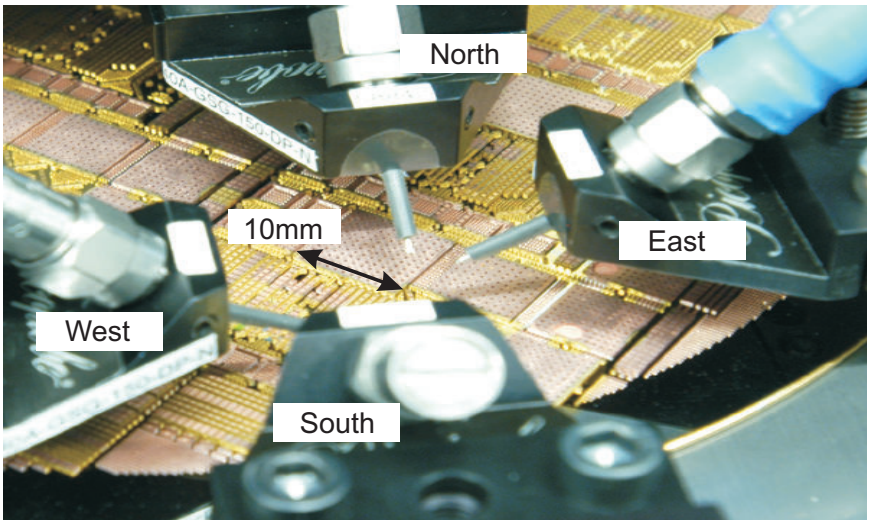

Figure 2.5: A photograph of the four-port measurement setup. The naming convention for the ports is indicated.

of the network analyzer) and reverse path (port 2 excited) [51]. Assuming the same connection can be made to the calibration standards as to the devices of interest, TRL uses a minimum of three transmission-line standards to solve for a two-port error matrix on either side of the device under test. One-port measurements are made on the *reflect* standards, whose sole requirement is to have a high reflection coefficient. The *line* standard is a length of transmission line that is identical to the *thru* standard except for being usually 90° longer at the center frequency of the band of interest. Full two-port measurements of these standards is required. In addition to the two-port error matrix that is calculated using this method, the propagation constant for the transmission line is found.

2.4.1 Four-Port Measurements

The branch-line coupler measurements given later in Chapter 4 are quite sensitive to the probe-transition discontinuity. The setup at BAE Systems is shown in Figure 2.5. The four probes are commonly spaced 90° from the others, as shown. To remove the probe-structure effects discussed in Section 2.3, measurements of TRL calibration struc-

tures for the North-South and East-West probes are then performed and the error boxes at each port are calculated using the traditional two-port TRL algorithm [50]. With the computed error boxes, it is possible to de-embed the effects of the probe structures at each of the ports to find the internal impedance matrix using [52]:

$$[\mathbf{Z}_{DUT}] = \{[\text{Diag } \mathbf{T}_{11}] - [\mathbf{Z}_{tot}][\text{Diag } \mathbf{T}_{21}]\}^{-1} \times \{[\mathbf{Z}_{tot}][\text{Diag } \mathbf{T}_{22}] - [\text{Diag } \mathbf{T}_{12}]\} \tag{2.3}$$

where [Diag $\mathbf{T}_{ij}$] is a diagonal matrix filled with the $\mathbf{T}_{ij}$ chain-matrix parameters for each of the ports. $[\mathbf{Z}_{tot}]$ is the four-port impedance matrix with the error boxes included. A schematic representation of the de-embedding of the probing structures from a four-port device is shown in Fig. 2.6; $[\mathbf{S}_{tot}]$ is measured and $[\mathbf{S}_{DUT}]$ is desired.

The measurements of the four error boxes are shown in Figure 2.6(b) on a Smith chart with the simulated values for the error box shown with the '△' symbol. As an example showing the utility of the calibration method, Figure 2.7 shows the difference in measurement results for the cases with and without de-embedding the probe transition of an ideal quadrature hybrid using Eq. 2.3. One of the measured error boxes of Figure 2.6(b) has been added at each of the ports for this example. These are compared to the simulated results for the coupler without the probe transitions. In Figure 2.7, it is evident that all aspects of the frequency response of the four-port devices change with the addition of the probe structures. Chapter 4 shows measured data that verifies this method for four-port devices.

The measurement procedure that have been outlined in the preceding paragraphs is summarized in the following steps.

(1) Perform four-port SOLT calibration.

(2) Measure TRL standards using the two 2-port combinations.

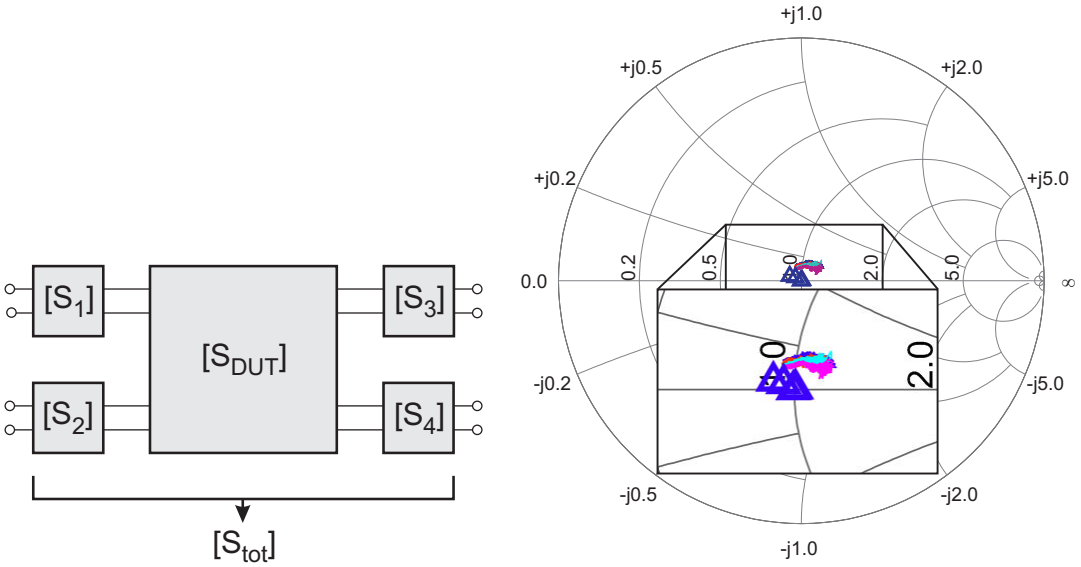

(a) (b)

Figure 2.6: (a) A schematic of the de-embedding method showing the parameters of the full measurement, the distinct probe-to-μ-coax transition parameters for each port, and the desired branch-line coupler measurement at the de-embedded reference plane. (b) S_{22} for each of the error boxes at the four ports compared to the simulated value plotted on a 50-Ω Smith chart. S_{22} of the simulated error box is shown with '△'. (From [30], © 2007 IEEE. Reprinted with permission.)

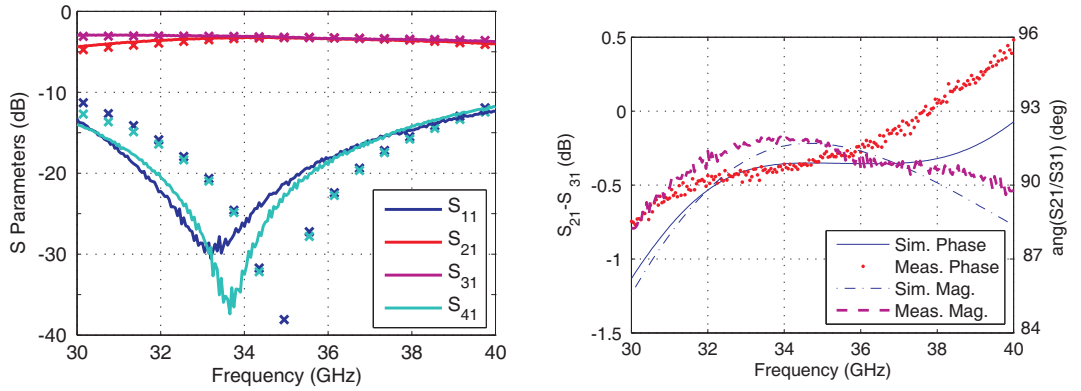

(a) (b)

Figure 2.7: An example response of a branch-line coupler with and without the de-embedding of the error boxes at the ports. An ideal hybrid is shown with the same error box at each of the ports. (a) The magnitude in dB for the S parameters when port 1 is fed. (b) The difference in phase and magnitude at the output ports for this case.

(3) Calculate S parameters of the error boxes at each of the ports.

(4) Measure the four-port device of interest.

(5) Apply de-embedding to the four-port measurements using Eq. 2.3.

Chapter 3

Cavity Resonators

3.1 Introduction

This chapter presents the analysis and data for seven *Ka*-band cavity resonators fabricated using the PolyStrata^{TM} process. With reference to the coordinate system indicated in Figure 3.1, the TE_{101} mode is used for the two-port resonators presented.

3.1.1 Definition of Quality Factor

High-quality-factor (high-Q) resonators are important building blocks for low-phase-noise oscillators and high-performance filters at microwave and millimeter-wave frequencies [53–55]. The quality factor is a measure of the loss of a resonant circuit and defined as

$$Q = \omega_0 \frac{W_m + W_e}{P_l} \tag{3.1}$$

where ω_0 is the angular frequency of resonance, W_m and W_e are the average stored electric and magnetic energies, and P_l is the energy lost per second. At resonance W_m and W_e are equal. The larger the value of Q, the fewer losses exist in a given resonator.

For resonators measured in two-port conditions, the Q-factors of the resonators are extracted from the $|S_{21}|$ measurements of the devices using the following [55]:

$$Q_L = \frac{f_0}{\Delta f_{3\,\mathrm{dB}}}\,, \tag{3.2}$$

$$S_{21}(\mathrm{dB}) = 20\log_{10}\left(\frac{Q_e}{Q_L}\right)\,, \tag{3.3}$$

and

$$\frac{1}{Q_L} = \frac{1}{Q} + \frac{1}{Q_e}\,, \tag{3.4}$$

where f_0 is the resonant frequency, $\Delta f_{3\,\mathrm{dB}}$ is the 3-dB bandwidth, Q_L is the loaded, Q is the unloaded and Q_e is the external quality factor of the resonator.

3.1.2 Background

We are interested in microwave and millimeter-wave resonators (as opposed to resonators for optical frequencies). Q factors on the order of 10^5 can be obtained with electrically large resonators, e.g. TE_{102} Bragg reflection sapphire resonators inside conductive cavities [56]. On the other hand, with compact planar resonators, such as microstrip resonators, it is difficult to obtain Q factors larger than a few hundred [57]. For lumped-component resonators, it is difficult to fabricate inductors with an effective Q larger than 40 for frequencies above 20 GHz [58]. This chapter discusses quasi-planar air-filled *Ka*-band cavity resonators of heights that are 250-μm tall with unloaded quality factors (Q_{un}) in the range of 400-500 and 700-μm tall with unloaded quality factors above 800. The resonators are fabricated by RHEM, using photolithography with a high-metal-layer aspect ratio, and they are air-filled in order to reduce the loss. Five different 250-μm-tall resonators and two separate 700-μm-tall designs are studied in this chapter, each with varying dimensions and mechanical support structures.

A sketch showing the combined pertinent features of the seven resonator designs, $R1$-$R7$, is shown in Figure 3.1, with dimensions given in Table 3.1. The values of the

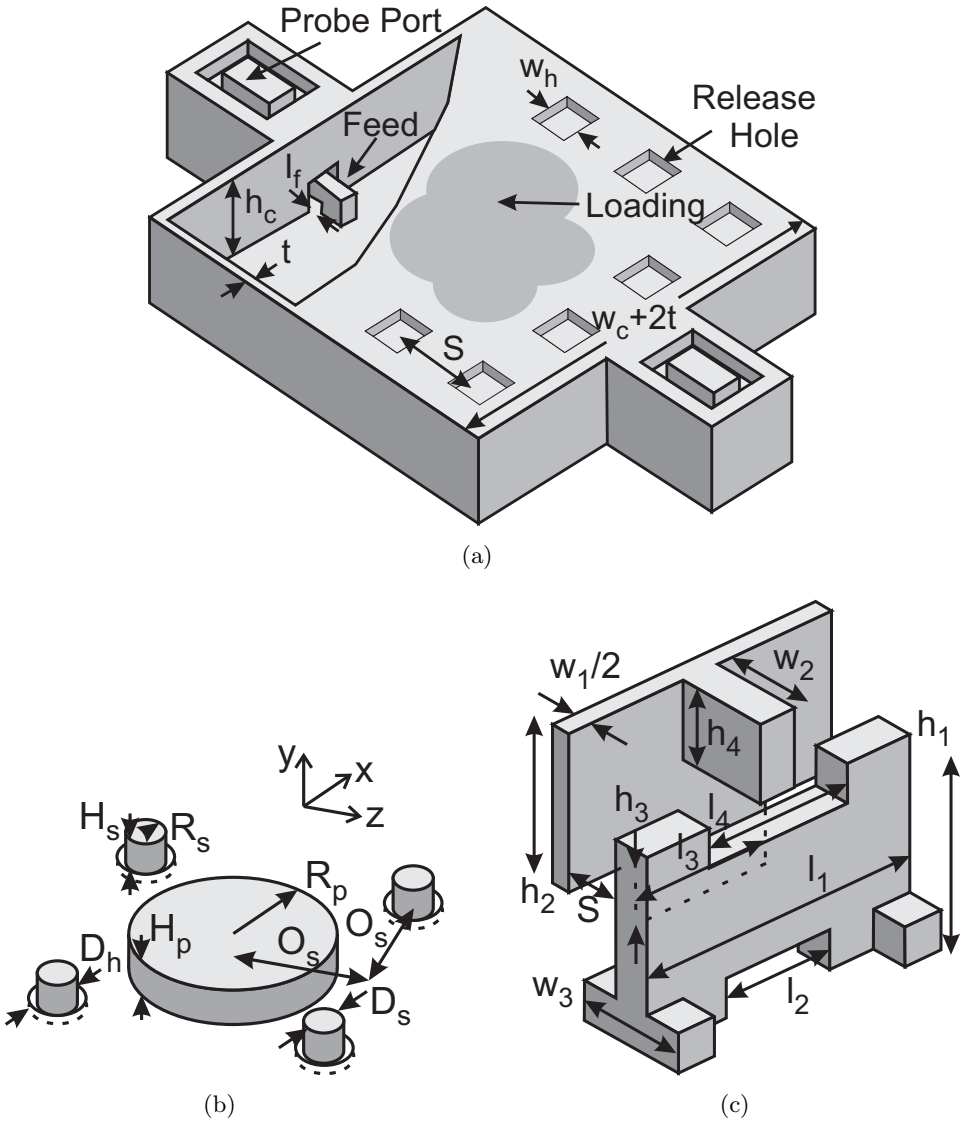

Figure 3.1: (a) Sketch of a loaded quasi-planar air-filled copper cavity resonator showing all relevant design dimensions (the values of specific dimensions are given in Table 3.1). (b) A general sketch showing loading dimensions for $R1 - R5$ (not all of the dimensions apply to each of the resonators). (c) A half-view sketch of the rib loading in $R7$. The ribs are cut along the xy plane to simplify the presentation, and the relevant dimensions are given in Table 3.2. (From [29], © 2007 IEEE. Reprinted with permission.)

dimensions of the loading ribs in $R7$, corresponding to what is shown in Figure 3.1(c), are given in Table 3.2.

The motivation for this work is to demonstrate high-Q resonators integrable with other passive components on the same wafer. These components include TEM trans-

mission lines [1], directional couplers, and divider and combiner networks [32]. The primary aim is to achieve a high Q factor while maintaining a very low profile, matching that of the other circuit components. To demonstrate this, a rectangular coaxial feed is implemented for the resonators discussed in this chapter, as shown in Figure 3.5. The other goal is to miniaturize the footprint of the resonator for a given Q_{un}.

The miniaturization of microwave resonators, including re-entrant cavity designs, has been of interest since the development of microwave engineering [59]. Work with filters using evanescent waveguide for miniaturization and suppression of spurious modes with the ability to do wide-band filters is presented in [60]. More recently, interest in microfabricated microwave and millimeter-wave resonators using various techniques has been seen. The loading of *C*-band surface micromachined cavity resonators with barium titanate and alumina is examined in [61]; *Q*s in the hundreds are demonstrated with fabrication tolerances being the most important limiting factor on performance. Silicon micromachining of *Ku*-band resonators with drain holes used to release the sacrificial material are fabricated as outlined in [62]; the electrical performance is decreased by a small amount of leftover silicon in the resonator after the processing. Silicon micromachined and metal-plated layered polymer resonators with miniaturization factors up to 70 % at *X*- and *Ku*-bands are presented in [63]. More recently, tuning from 5.4 to 10.9 GHz of an evanescent-mode resonator was demonstrated [64]. The resonators presented in [63,64] use fin-shaped interdigital capacitor loading (among other techniques), and are an excellent starting point for the designs presented here.

Ka-band and *V*-band rectangular coaxial transmission line filters with nickel walls using the EFAB$^{\mathrm{TM}}$ process have been shown in [4] and [12], respectively. In this work, the resonators are not characterized alone, however, the largest theoretical *Q*s that can be obtained from nickel coaxial resonators with the same dimensions as in [4] and [11] are less than 80. The same technology with gold plating has recently demonstrated Q factors near 250 at 60 GHz [17]. Laser etching of copper has been used to fabricate rectangular

Table 3.1: Dimensions of the major features of the resonator corresponding to the diagram shown in Figure 3.1 for the seven resonators.

geometry parameter	abv.	$R1$	$R2$	$R3$	$R4$	$R5$	$R6$	$R7$
operating frequency (GHz)	f_0	26.0	26.0	26.0	26.0	26.0	36.0	36.0
cavity width (mm)	w_c	8.11	7.93	7.85	9.56	7.50	5.842	3.20
cavity height (μm)	h_c	250	250	250	250	250	700	700
release hole width (μm)	w_h	200	200	200	200	200	400	400
release hole spacing (μm)	S	700	780	775	775	690	807	817
support diameter (μm)	D_s	–	150	150	150	150	–	–
support hole diameter (μm)	D_h	–	230	230	–	–	–	–
loading puck radius (mm)	R_p	–	–	–	–	.875	–	–
support center offset (mm)	O_s	–	0.00	2.25	2.25	2.08	–	–
loading puck height (μm)	H_p	–	–	–	–	175	–	–
feed inset (μm)	I_f	100	100	100	100	125	75	75
wall thickness (μm)	t	75	75	75	75	75	75	75
number of supports	–	0	1	4	4	4	–	–
number of top wall holes	N^2	144	100	100	144	100	49	16

coaxial *Ka*-band filters [5]. *Q*-band 2.5-D resonators using U-shaped metallic half-wave resonators have been fabricated using a low temperature co-fired ceramic (LTCC) implementation [65]. Compact filter design using several of these U-shaped resonators in close proximity is possible.

Photographs of some of the fabricated resonators are shown in Figure 3.2. Figure 3.2(a) is a photograph of $R5$, however it is indicative of the general size of the cavity

Table 3.2: Design values for the dimensions of the rib-loading structures of $R7$, as shown in Figure 3.1(c). All of the values are given in μm.

w_1	100	h_1	500	l_1	760	S	150
w_2	250	h_2	400	l_2	300	I_f	55
w_3	300	h_3	200	l_3	380	w_h	400
h_c	700	h_4	200	l_4	400	w_c	3200

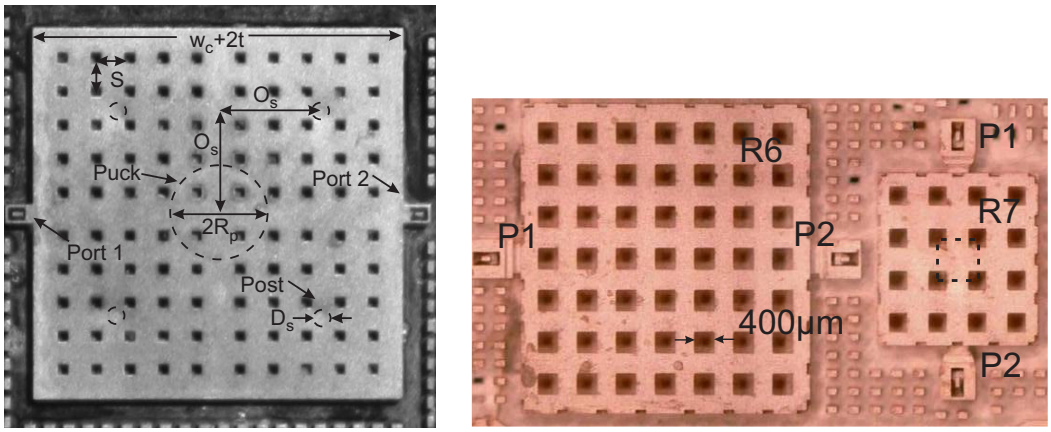

(a) (b)

Figure 3.2: Photographs of a few of the fabricated resonators. (a) An image of $R5$, although it is representative of $R1$-$R5$. (b) A photograph showing $R6$ and $R7$, highlighting the miniaturization accomplished by going from the size of $R6$ to $R7$. ((a) from [35], © 2006 EuMA. Reprinted with permission. (b) from [29], © 2007 IEEE. Reprinted with permission.)

and release holes of $R1$-$R5$. Figure 3.2(b) shows a comparison of the relative footprints of $R6$ and $R7$. Figure 3.2(a) and Figure 3.2(b) are sized such that the scale is roughly the same.

Seven resonator designs using the PolyStrata^{TM} process with up to 10 layers are demonstrated in this chapter. The fabrication and resulting mechanical parameters dictate the electrical design. The major fabrication-related factors and their influence on component design are found to be the following.

(1) Total resonator height is limited by the number of layers and thickness of each layer. In our case with 10 layers, a maximal cavity height of 700 μm is possible, which will limit the Q factor as presented in Figure 3.3. The electrical height of the tallest resonator presented in this paper is one twelfth of a free-space (TEM) wavelength. This analysis is presented in Section 3.2.1.

(2) Photoresist release holes on the top wall and on the side walls limit the Q factor and it is desired to have a small number of these holes. However, a relatively

large number of holes are required to completely evacuate the lossy photoresist from the cavity. The size and number of release holes was carefully examined within fabrication parameters and is described in Section 3.2.3.

(3) The design of the loading to reduce the size of the resonator is limited to what can be fabricated with this technology. The main limitation is the size of the loading structure which needed to be mechanically fixed to the top wall while providing enough loading. We could not use previously published designs as, given the mechanical constraints, they would not provide a sufficiently large loading reactance. This constraint resulted in a three-dimensional loading which is unique to this work and differs from the fins presented in [63]. This is presented in Section 3.4.7.

(4) The aspect ratio of a thin cavity is such that the top wall can sag or bulge. The mechanical support posts, which increase the footprint of the 26-GHz loaded cavity (see Section 3.4.4), are eliminated in the $R7$ design presented in Section 3.4.7 because of the miniaturization with the three-dimensional loading.

(5) The inductive coupling between the input μ-coaxial cable and cavity is constrained by the height of the center conductor and the required impedance match, as is described in Section 3.2.2.

3.1.3 Outline of Chapter

The influence of the preceding constraints are discussed in the remainder of the chapter. In addition, there are other topics of interest with regard to the design and characterization of these millimeter-wave resonators. A general outline of the remainder of the chapter is the following.

- Section 3.2 discusses three design considerations common to all the resonators: the effect of the cavity height on Q, the placement of the release holes, and the

two-port transmission levels achievable with the presented feeding method.

- Section 3.3 describes the analysis methods used for the design of the resonators.
- Section 3.4 elucidates specific aspects of the dominant behavior of each of the cavity resonators.
- Section 3.5 presents the measurement data for the five resonator configurations built to operate near 26 GHz using the 5-layer process and two resonators fabricated with the 10-layer process for operation near 36 GHz.
- Section 3.6 derives circuit models for $R5$ and $R7$. The measured and modeled input impedances are compared to that given by the circuit models.
- Section 3.7 provides a few ending comments for the chapter and indicates some of the future work to be done in this area.

3.2 Common Characteristics – Cavity Height, Feeding, and Release Holes

Before talking about aspects of the resonator designs specific to the individual resonators, it is worth taking a moment to describe a few aspects of the analysis and design that are common to all of the designs. The height of the cavity has the greatest role on determining the quality factor of the resonators. A method of normalizing the height of the cavity to allow the comparison of resonators at different frequencies, with different cavity heights, and with different materials is presented. Following this, the feeding mechanism for the resonators is described. Ideally, one would want to have the ability to have a wide range of coupling ratios dependent on the application, and the achievement of this is presented. The last topic of this section is the effect of the release holes on the Q_{un} of the resonator.

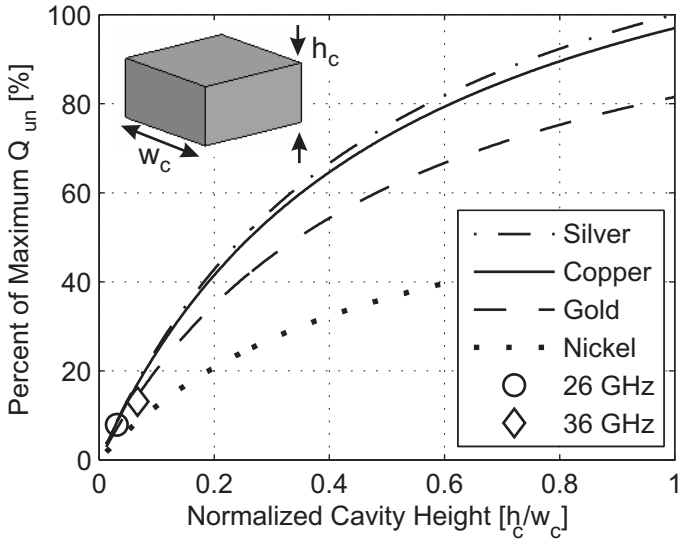

Figure 3.3: The percentage of the maximum achievable Q_{un} for an electrical height in wavelengths for the conductivities of several standard metals for the cavity. (From [29], © 2007 IEEE. Reprinted with permission.)

3.2.1 Cavity Height

It is worth clarifying the usage of the word "quasi-planar" in the context of this work. Figure 3.3 shows simulated values of Q_{un} for a square cavity with a footprint $w_c \sim \lambda_g/2$ on the side, and with different metal conductivity values. The height of the cavity, h_c, is varied from a small value to w_c. The measured unloaded Q factors for two unloaded quasi-planar cavity resonators are indicated in Figure 3.3 for comparison. The normalized heights of the two cavities are $0.03w_c$ ($R1$) and $0.07w_c$ ($R6$), justifying the terminology "quasi planar". The small electrical height allows resonators and micro-coaxial feeds to be fabricated in the same process, while simultaneously providing Q factors higher than those of coaxial transmission line resonators of the same height.

A number of impressive X- through Ka-band microfabricated miniature resonators have been demonstrated in the past few years [62, 63, 66–70]. Different dimensions, frequencies, fabrication processes, miniaturization techniques and other design factors produce resonators with vastly different quality factors, so it is difficult to meaningfully

compare them. Because of the comparatively small cavity heights of the resonators of this paper, a normalized cavity height is defined as follows:

$$h = \frac{h_c}{\lambda_0}\sqrt{\frac{f_n}{f_0}}\,, \tag{3.5}$$

where h_c is the physical cavity height, f_0 is the resonant frequency, and f_n is the normalizing frequency (26 GHz). The frequency ratio takes into account lower skin-effect conductor losses at lower frequencies. The demonstrated unloaded Q factors as a function of the normalized height of the resonators in [62, 63, 66–69], along with a value demonstrated in this paper, are given in Figure 3.4. The solid line represents the highest theoretical value of an ideal smooth silver-lined, TE_{101} resonant cavity for a given height. This allows one to determine how well a fabrication method creates resonators approaching the theoretical limit for the quality factor. The stripline resonators in [66] are included in this comparison because they exhibit Q factors near levels achieved using extreme miniaturization techniques for cavity resonators. The Q of the resonator in [62] compared to that of [69], both fabricated by the same authors, demonstrates the extent to which miniaturization of a resonator can decrease the achievable Q for a given height.

The influence of the height of the cavity on the Q of the resonator, though obvious qualitatively, has been quantified with regards to this work. For the normalized height of Eq. 3.5, $R1$ performs closer to the theoretical maximum than the best microfabricated resonators to which it has been compared [62, 63, 66–69].

3.2.2 Resonator Feeding

Two types of feeding structures are used for the resonators, which are measured in a 2-port configuration. A five-layer process is used to fabricate $R1$-$R5$, and Figure 3.5 (a) and (b) show a photograph and sketch of this feed structures. For $R6$ and $R7$, a ten-layer fabrication process is used, and Figure 3.5 (c) and (d) correspond to these feed structures. To prepare the wafer to be photographed as shown in Figure 3.5(a) and

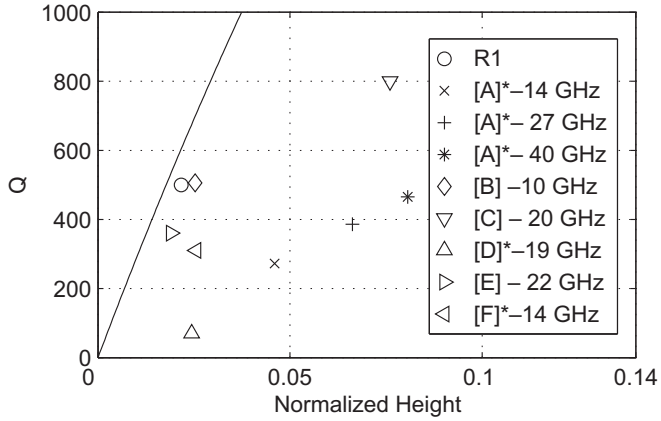

Figure 3.4: Comparison of unloaded Q versus normalized electrical height, $\frac{h_c}{\lambda_0}\sqrt{\frac{f_n}{f_0}}$, for $R1$, and resonators in [A] - [66], [B] - [67], [C] - [68], [D] - [62], [E] - [69], [F] - [63]. The resonators that use a miniaturization technique, e.g. a dielectric filling or capacitive loading, are indicated with a '*' in the legend. The solid line is the theoretical unloaded Q for an ideal silver-walled $\lambda/2$ square resonator with a normalized height specified by the horizontal axis, and $f_n = 26\,\text{GHz}$. (From [31],)

Figure 3.5(c), the devices are filled with a clear epoxy that provides enough mechanical strength for the wafer to be diced down the center line of the resonator without drastically altering the profile of the cross section that is to be diced. For each of these resonators, inductive coupling into the cavity resonators is accomplished by shorting the center conductor of the rectangular coax of the feed to the bottom metal wall. By varying the distance that the center conductor penetrates into the cavity before it is shorted to the bottom wall, I_f, a wide variety of coupling levels are achievable. This is demonstrated in Figure 3.6 for four hypothetical cavity resonators. These curves show S_{21} for two cavity heights, 250 μm and 700 μm, at the two design frequencies, 26 GHz and 36 GHz. This indicates that the electrical length of the feed inset is more important than the ratios of the feed height to cavity height.

3.2.3 Design of Release Holes

In order to remove lossy photoresist after the top metal layer is deposited, release holes in the top layer and on the side walls are necessary. Electrically, these holes perturb the current flow and therefore affect the resonant frequency as well as the Q factor. While no holes or small holes will give the highest Q factor, many larger holes are needed for high fabrication yield, so an optimization study is required. The release holes on the sides of these resonators do not have a large effect on the electrical performance because of the cavity heights used, so only the effects of the top holes will be examined. Figure 3.7 shows the results of a 3-D FEM study, using Ansoft HFSS version 10, of Q_{un} of a cavity resonator versus the number of rows of holes on the cavity resonator top surface, N (total holes = N^2). The ratio of the surface area of the release holes to the total top-wall surface area of the resonator is kept constant. For what is fabricated, this ratio is 8.74 % for $R1$, the five-layer, 26-GHz design (250-μm cavity height) and 21.80 % for $R6$,the ten-layer, 36-GHz design (700-μm cavity height). These numbers are dictated by 200 by 200-μm square release holes at 26 GHz ($N^2 = 144$) and 400 by

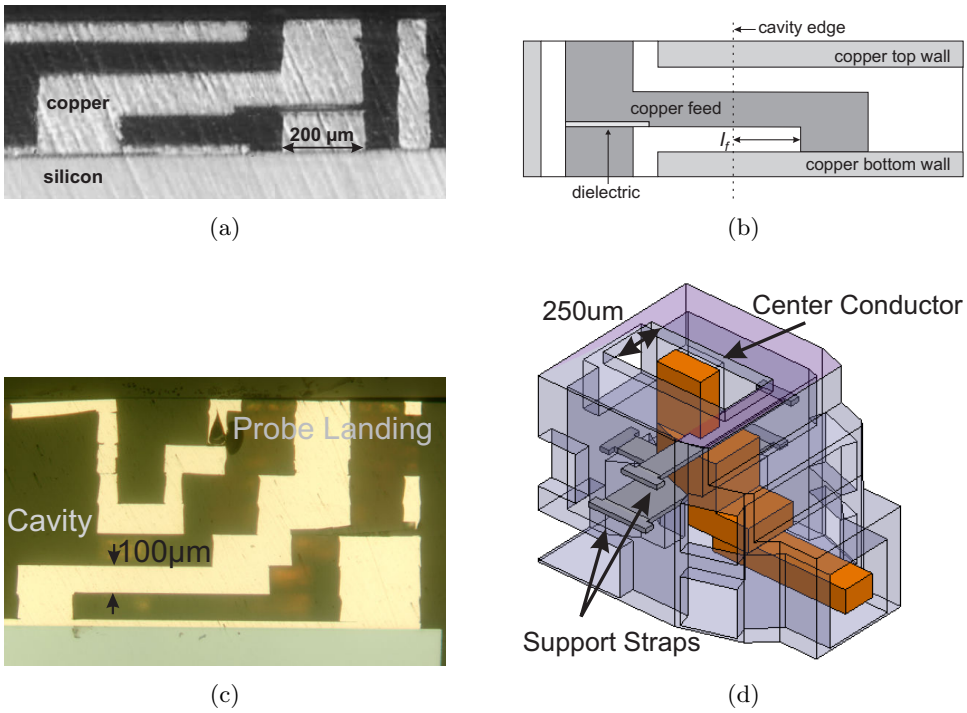

Figure 3.5: Cross sections of the probe structures and feed mechanism for the launches are shown. (a) A photograph of the probe structure used for $R1$-$R5$. (b) A sketch of (a) with labels detailing the major components. (c) A photograph of the probe structure for $R6$ and $R7$. (d) A 3-D mechanical model of the probe structures used for $R6$ and $R7$. The photos here are courtesy of the Mayo Clinic. ((a) from [35], © 2006 EuMA. Reprinted with permission. (b) from [31], © 2006 IEEE. Reprinted with permission. (c) and (d) from [29], © 2007 IEEE. Reprinted with permission.)

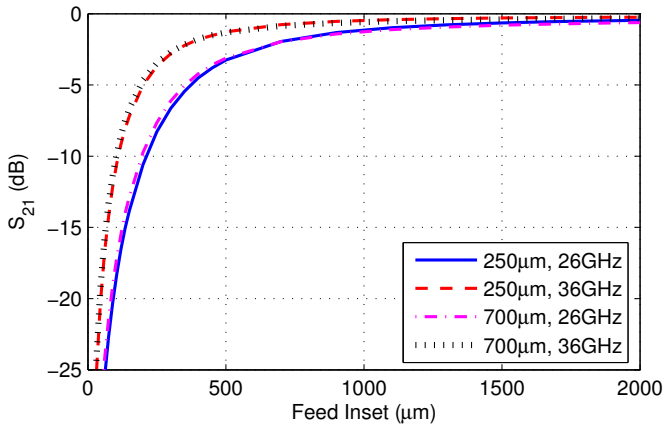

Figure 3.6: The coupling through the cavity, S_{21}, is shown for different lengths of the feed inset into the cavity, I_f. The length that the feed penetrates into the cavity is shown for empty cavity resonators operating at 26 GHz and 36 GHz. This is done for two fabricated cavity heights.

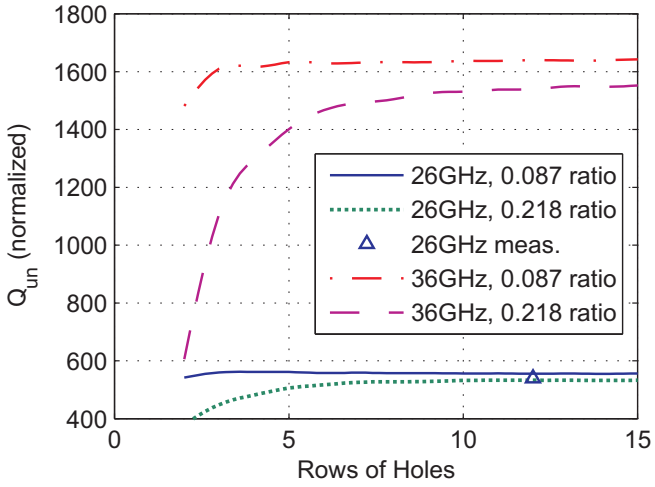

Figure 3.7: Normalized Q_{un} for different sized release holes on a cavity resonator. The surface area of the release holes is kept constant with respect to the top surface area of the cavity. This is shown for the 250-μm-tall cavities at 26 GHz and 700-μm-tall cavities at 36 GHz. (From [29], © 2007 IEEE. Reprinted with permission.)

400-μm square release holes at 36 GHz ($N^2 = 49$). Figure 3.7 shows curves obtained numerically for both ratios at both design frequencies. The resonant frequency of the resonators changes slightly as the number of holes increases. To compare these changes in Q_{un} for a fixed frequency, it is necessary to normalize the Q values.

We begin with the formula for the Q due to the conductor losses of a TE_{101} rectangular metallic cavity resonator, as can be found in [71]:

$$Q_c = \frac{(kad)^3 b\eta}{2\pi^2 R_s} \frac{1}{2a^3b + 2bd^3 + a^3d + ad^3} \tag{3.6}$$

where k is the wavenumber, η is the wave impedance of the cavity-filling medium, R_s is the surface resistance of the cavity walls. The length, width, and height of the cavity are a, d, and b, respectively. We assume that a and d are equal and that the cavity is air filled:

$$Q_c = \frac{4f_0^{2.5}}{c^3} \frac{a^3b}{4b + 2a} \sqrt{\frac{\pi\sigma}{\epsilon_0}} \tag{3.7}$$

To compare two resonators with the same size but different configurations of

release holes, it is necessary to normalize the calculated unloaded quality factors based on the frequency of resonance. If the cavity dimensions and materials do not change, we find the ratio of quality factors to be related to a power of the ratio of the resonant frequencies:

$$\frac{Q_{c1}}{Q_{c2}} \propto (f_1/f_2)^{2.5} \tag{3.8}$$

The data shown in Figure 3.7 are simulated for two frequencies and two top plate surface area to release hole surface area ratios using the Q normalization in (3.8). The cavity is 250 μm tall for the 26-GHz resonator ($R1$) and 700 μm tall for the 36-GHz resonator ($R6$). We see that the resonator performance is minimally affected by the release hole size when the cavity is 250 μm tall; however, the unloaded Q of the cavity is large enough in the 700-μm-tall case, that an effect on the Q is seen for large hole sizes.

3.3 Cavity Resonator Analysis and General Design

The different resonators and feed are analyzed with Ansoft's 3-D FEM HFSS^{TM} software package, using both eigenmode and driven analyses [72]. Figure 3.8 shows a comparison of the computed Q_{un} of a cavity resonator using three different modeling techniques. The analytical technique calculates the Q_{un} using the common formula for a TE_{101} cavity resonator based upon the cavity dimensions, the surface resistance of the cavity metal, and the frequency of interest [71]. The finite element models include the feeds and associated losses. As a result, the Q-factors calculated from the finite element models are lower than those found using the analytical formula, but the difference is less than 1.5 %. The two FEM approaches give results within 0.2 %. There is a near constant offset between the three curves over the full frequency range. The resonant frequency changes less than 0.4 % over the range of values utilized for this demonstration.

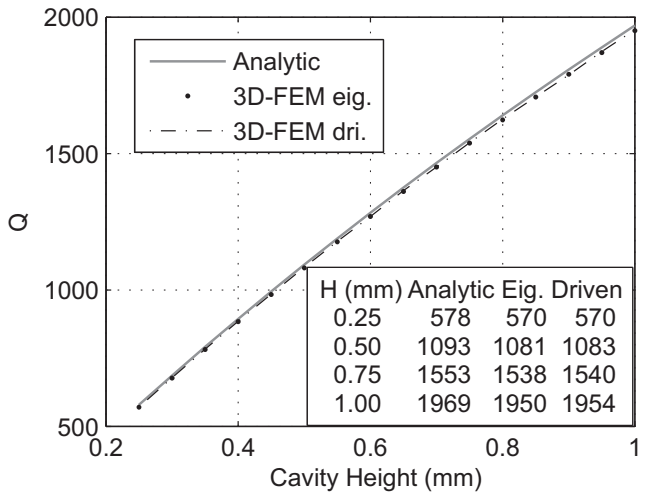

Figure 3.8: For a fixed footprint, the unloaded Q-factor is computed for a copper-walled cavity resonator with different cavity heights, H, using an analytical formula, and both driven and eigenmode 3-D FEM analyses. (From [29], © 2006 IEEE. Reprinted with permission.)

The challenge for the analysis is the large range of relevant electrical sizes in the resonator models. The full resonators have dimensions on the order of $\lambda_0/2$, and the release holes have dimensions less than $\lambda_0/50$. A large number of tetrahedra are required to mesh the volume. Symmetry planes of the resonators are exploited to reduce the size of the computational models, as is mentioned in Section 2.1. The eigenmode analyses use models constituting one quarter of the geometry. The driven analyses use one half of the geometry divided down the center line from one port to the other.

3.4 Fabrication-Driven Analysis and Design

This section gives descriptions of the detailed analysis for the seven different resonators, each with characteristics as follows:

- $R1$ is a TE_{101} cavity, with dimensions like the ideal one from Fig.5, but with the release holes required for photoresist removal;
- $R2$ has a mechanical support post in addition to the release holes. The copper support post rests on the silicon substrate in the center of the cavity and is insulated from the bottom wall with an annular slot;
- $R3$ has four support posts resting on the Si substrate as in $R2$. The posts are symmetrically placed inside the cavity;
- $R4$ has four support posts that are connected directly between the top and bottom walls, shorting the two walls, unlike $R2$ and $R3$. The resulting footprint is larger than the other resonators.
- $R5$ has four support posts that are connected directly between the top and bottom walls, as $R4$. There is also a capacitive metallic puck in the center that is used for miniaturization.

- $R6$ is a simple cavity, as $R1$, fabricated using the ten-layer process with an operating frequency at 36 GHz.

- $R7$ is a miniaturized loaded cavity fabricated using the ten-layer process of $R6$. The loading provides a 70 % reduction in surface area compared to $R6$.

A selection of specific loss mechanisms is studied using the 3-D FEM in addition to the fabricated designs. Where appropriate, the models are simplified to highlight the salient effects, e.g. the release holes are omitted from the model.

3.4.1 R1-Cavity Resonator

This initial resonator serves as a baseline model with which to compare the subsequent designs. Figure 3.9(a) shows a conceptual cross section of $R1$. This topology is the simplest conceivable resonator using this technology. The TE_{101} cavity resonator is designed to operate near 26 GHz. From Figure 3.8, the theoretical value of the unloaded Q-factor for this geometry with a cavity height of 250 μm is near 575 if the cavity is perfectly constructed of smooth copper. However, this ideal model does not account for several loss mechanisms encountered in the presented microfabrication process. One of the loss mechanisms is in the feed structure. With the coupling levels in our case, this loss is a few percent.

The release holes contribute to the loss, as well. The resonator is modeled by effectively placing the resonator within a numerical anechoic chamber. The release holes are open to the anechoic chamber, allowing radiative losses to be examined. The holes are 200 μm by 200 μm, which puts the cutoff frequency of the holes as rectangular waveguides above 750 GHz. Evanescent modes in the release holes can allow some energy leakage out of the cavity and decrease the unloaded Q-factor of the cavity. A numerical study reveals that reducing the thickness of the top wall from 50 μm to 10 μm decreases the quality factor by 2 %. The simulated Q given in Table 3.3 including all

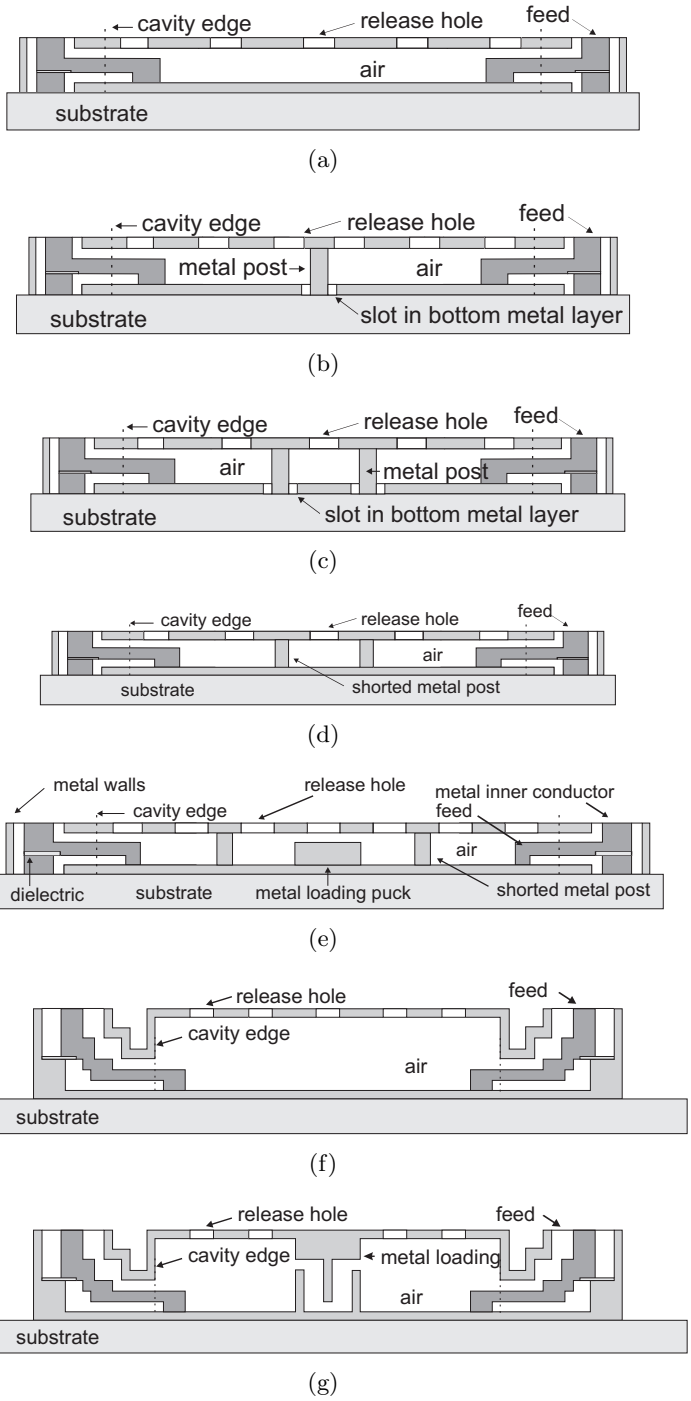

Figure 3.9: Sketches of cross-sectional views of the seven resonators with feeds are shown. For clarity, the resonators are not drawn to scale and the number of release holes is not accurate. (a) $R1$, (b) $R2$, (c) $R3$, (d) $R4$, (e) $R5$, (f) $R6$, and (g) $R7$. ((a)-(d) from [31], © 2006 IEEE. Reprinted with permission. (e) from [35], © 2006 IEEE. Reprinted with permission.)

Table 3.3: A summary of the simulation and measurement results is given for the seven different resonator configurations.

		Resonator						
		$R1$	$R2$	$R3$	$R4$	$R5$	$R6$	$R7$
sim.	f_0 (GHz)	26.02	26.11	26.40	26.94	25.91	35.98	35.99
	S_{21} (dB)	-14.6	-15.2	-15.0	-20.6	-19.4	-9.6	-10.3
	Q_L	441	424	406	454	454	987	691
	Q_{un}	541	513	494	500	508	1306	995
meas.	f_0 (GHz)	26.06	26.44	26.51	26.33	25.75	35.73	35.89
	S_{21} (dB)	-15.8	-15.0	-16.5	-21.2	-19.8	-13.6	-11.3
	Q_L	392	403	335	409	397	803	604
	Q_{un}	470	490	391	449	442	1015	829

loss mechanisms is 5 % smaller than the value given in Figure 3.8, for which the effect of the release holes is not included. It is seen that the release holes do affect the achievable Q of the resonator, despite having a cutoff frequency much higher than the resonant frequency, as will be discussed in Section 3.5, where the loss budgets of each of the resonators are presented.

3.4.2 R2-Cavity Resonator with a Single Post to the Substrate

A support post in the center of the resonator is designed to increase the mechanical stability of the top wall. This post connects from the top wall to the substrate below the resonator, as shown in the diagram in Figure 3.9(b). A slot is opened in the metal floor of the resonator around the post to electrically isolate the top and bottom walls. The metal post and slot form a series L-C circuit, but at 26 GHz, the capacitive gap between the bottom wall and the post dominates the electrical behavior. This capacitance, in parallel with that between the top and bottom walls, increases the overall capacitance and decreases the dimensions of the resonator slightly compared to the baseline resonator, $R1$, for a fixed f_0.

3.4.3 R3-Cavity Resonator with Four Posts to the Substrate

The third design has four posts to the substrate. Figure 3.9(c) shows a cross-sectional view of $R3$ including two of the support posts and slots. Using four posts increases the mechanical stability as compared to that of a single post. However, the electrical effect of the four off-centered posts individually is reduced from the case of a single centered post due to the lower fields. A design parameter is the post offset from the resonator center, O in Figure 3.1(a). Smaller values of O decrease the resonator size for a given f_0, and reduces the Q. To a certain limit, decreasing the offset of the posts from the center, O, increases the resonant frequency of the resonator.

The effect of the substrate losses on the performance of $R3$ without release holes and without the feed is studied with all other dimensions kept the same as in Table 3.1. Energy from the resonator leaks into the substrate through the annular slots used to isolate the support posts from the bottom wall of the resonator. Figure 3.10 shows the effects of the substrate parameters (ϵ_r and $\tan\delta$) on the Q of the resonator. The mean circumference of the annular slot is approximately $\lambda_0/20$ and for a Si substrate with a quasi-static approximation of $\epsilon_{\text{eff}} \approx \frac{\epsilon_r+1}{2} = 6.45$, the circumference increases to approximately $\lambda_{\text{eff}}/8$, influencing the dramatic increase in losses with larger substrate relative permittivities.

3.4.4 R4-Cavity Resonator with Four Posts to the Bottom Metal Layer Operating at 26 GHz

The previously described post/slot combination decreases the size and Q of the cavity. Alternatively, metal inductive posts can be used. The $R4$ design eliminates the slot to silicon for the support posts, as depicted in Figure 3.9(d). The inductive effect of the 150-μm diameter posts is less if they are spaced further from the center of the resonator, but the mechanical advantage decreases as the support posts are moved

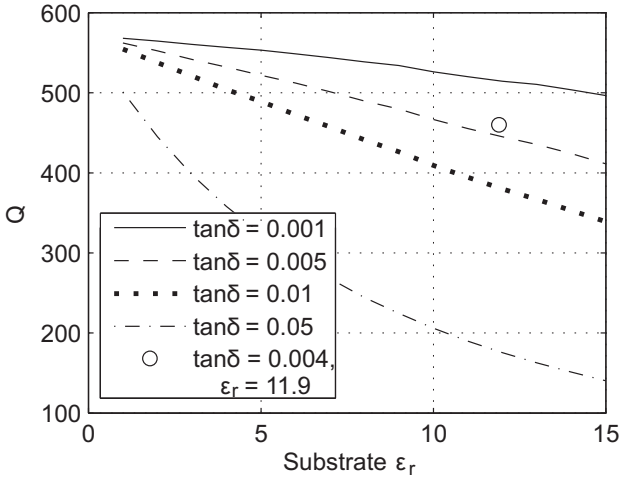

Figure 3.10: A simplified version of $R3$ is modeled with the relative permittivity and loss tangent of the substrate varied. Two general trends are observed: an increase of the permittivity makes the effective size of the support post holes larger and decreases the Q of the resonator; and the substrate losses are not negligible. A marker (O) is placed to indicate the Q corresponding to the high-resistivity Si substrate parameters of this design. (From [31],)

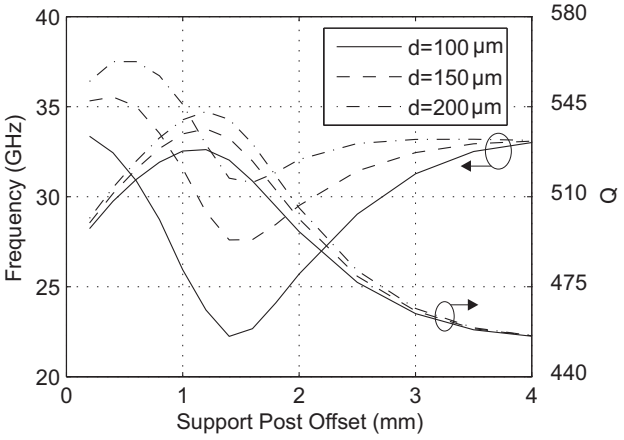

Figure 3.11: The offset of the support posts from the center, O, is varied from near the center of the resonator towards the outside for a simplified $R4$ resonator. This is done for three different sizes of support posts. The effects on resonant frequency and unloaded Q are shown. (From [31], © 2006 IEEE. Reprinted with permission.)

closer to the outer walls of the resonator. This effect makes the overall footprint of the resonator larger than would be the case for an empty cavity resonator, but this tradeoff in size may be preferred to a lower Q if mechanical stability is necessary and the resonator would otherwise be opened to a lossy substrate.

Figure 3.11 shows the unloaded Q and the resonant frequency of a resonator similar to $R4$ for different support post offsets, O. Three different support post diameters are used for the simulation: 100 μm, 150 μm, and 200 μm. The simulation, performed using 3-D FEM eigenmode analysis, neither includes the feed, nor the release holes. The cavity behaves similarly to a coaxial cavity resonator for values of O less than 1.2 mm, as can be verified by the examining the field profile. However, as O continues to increase, the resonator behaves more like a rectangular cavity resonator. The diameter of the post has a large effect on the resonant frequency of the resonator, but a small effect on Q. 150-μm support posts are chosen, making the resonant frequency of the cavity less sensitive to O than would occur with smaller post diameters.

3.4.5 R5-Cavity Resonator with Capacitive Loading by Metallic Puck Operating at 26 GHz

It is desired to shrink the size of the resonator while keeping the metal support posts as in $R4$. This is done using capacitive loading with a metallic feature as shown in Figure 3.9(e). The values used for the dimensions of the resonator are given in Table 3.1. The use of the capacitive metal puck in the resonator creates a concentration of fields in the gap between the puck and the top wall. This increased capacitance can be exploited as a miniaturization technique. Four metal support posts are equally offset from the center of the resonator. The electrical effect of these four supports in parallel have an effect of decreasing the overall inductance of the resonator, thus raising the resonant frequency, but the capacitive puck is designed large enough to compensate for the decreased inductance, and shrink the size of the resonator.

Figure 3.12(a) shows the results of a parametric study of the size of the capacitive loading puck of the resonator. The height of the puck is swept from 120 μm to 240 μm while the diameter of the puck is determined that keeps the resonant frequency at 26.0 GHz. The unloaded Q is then computed for the geometry. Interestingly, there is a combination of the puck height and diameter that gives the best Q. This occurs when the gap between the puck and the top wall of the cavity is quite small, however if that gap becomes too small, the Q begins to decrease again as the puck is practically shorted to the top wall. Physically, as the puck height increases, the puck diameter necessary for a given frequency decreases, this reduces the metal surface area in the resonator and increases the volume, increasing the Q. The current fabrication process allows three possible discrete heights, as there are three layers that makeup the actual cavity (two more layers exist, one for the top wall and one for the bottom wall, making a total of five layers). The tallest height is chosen to maximize the Q-factor, whose value is less than 2 % lower than the highest theoretical value in this configuration.

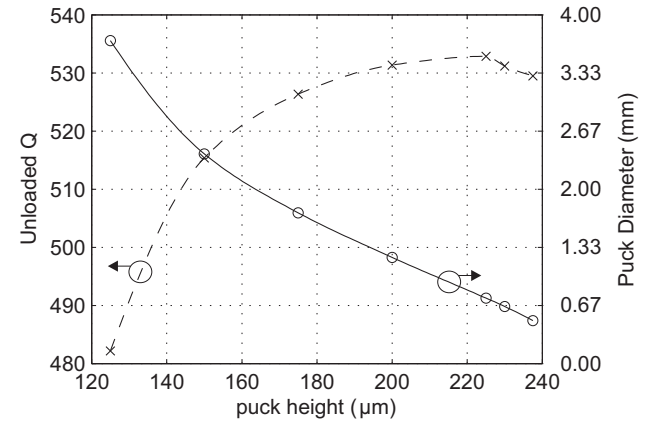

(a)

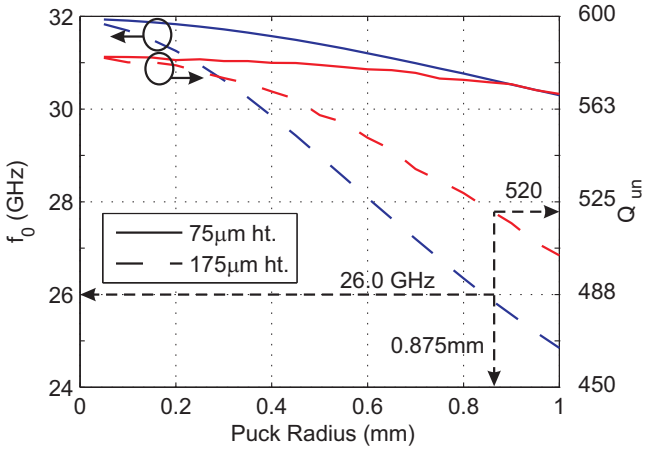

(b)

Figure 3.12: (a) The results of a parametric analysis of a simplified model of the resonator are shown. The analysis examined different combinations of the height and diameter for the loading puck (H_p and $2R_p$ from Figure 3.1), while maintaining a resonant frequency of 26 GHz. Eigenmode analysis using the FEM is employed to obtain the results shown here. (b) The results of a parametric analysis of a simplified model of $R5$. The release holes are not included for this analysis. The FEM eigenmode analysis examines how different diameters for the loading puck affect the Q_{un} and f_0 of the resonator. Two puck heights, 75 μm and 175 μm, corresponding to the two possible heights using the five-layer fabrication process, are examined. Values corresponding to the fabricated resonator are indicated on the graph. ((a) from [35], (b) from [29],)

Figure 3.12(b) shows the results of a numerical study of the size of the capacitive loading puck of the 26-GHz resonator, $R5$, for puck heights of 75 μm and 175 μm, corresponding to the two possible values using the five-layer process. The position and size of the support posts and the overall dimensions of the resonator are kept constant, unlike Figure 3.12(a), where f_0 is kept constant. The fabrication process allows three possible discrete heights (0, 75, and 175 μm), as there are three layers that make up the actual cavity (two more layers exist, one for the top wall and one for the bottom wall, making a total of five layers). The tallest height is chosen to maximize the Q-factor, whose theoretical value is less than 2 % lower than the highest ideal value for a copper resonator without release holes.

3.4.6 R6 - Cavity Resonator Operating at 36 GHz

After building the 5-layer resonators for operation at 26 GHz, a few resonators are designed for 36-GHz operation. $R6$ is a plain, empty cavity resonator, as the sketch of the cross section shows in Figure 3.9(f). A ten-layer process is used for the fabrication, allowing these resonators to be integrated with rectacoax designs employing two layers of coax. Figure 3.2(b) shows a photograph of this resonator on the left side of the image. The release holes are larger than those of $R1$-$R5$ because it was determined that the removal of the photoresist from the large, continuous regions of the cavity resonators required larger holes. 400 μm by 400 μm holes are large enough to start noticing the radiation through the holes, yet still small enough to fabricate resonators with Q_{un} greater than 1000 (see Figure 3.7).

3.4.7 R7 - Rib-Loaded Cavity Resonator Operating at 36 GHz

Taking the information that is learned from the designs for $R1$-$R6$, a resonator is designed that uses 3-D loading of the cavity to provide 70 % miniaturization. Figure 3.13 presents the results of a parametric study examining the effect of the rib spacing, S,

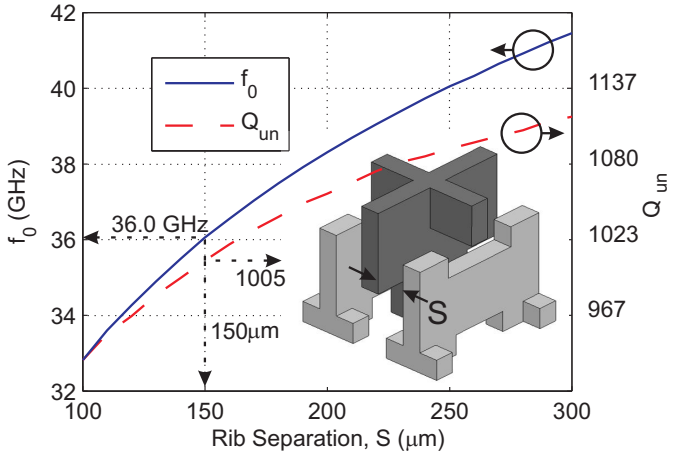

Figure 3.13: The results of a parametric analysis of the miniaturized 36 GHz resonator *R*7. The analysis examines different spacings of the loading ribs, S, as given in the figure inset. Eigenmode analysis using the FEM is employed, and values corresponding to the fabricated resonator are indicated on the graph. (From [29], © 2007 IEEE. Reprinted with permission.)

on Q_{un} and f_0 of the resonator $R7$. The values corresponding to the dimensions used for the fabrication are highlighted on the graph. As the rib separation is increased, the capacitance between the ribs diminishes, however the capacitive coupling from the ribs to the opposite wall of the cavity remains strong. The scaling of the two y-axes is the same relative to the first point of each data set, emphasizing that the frequency changes more rapidly than Q_{un} over the range of separation values considered.

3.5 Resonator Measurement Results

The measurement setup includes an HP-8510C network analyzer with Cascade Microtech 150-μm pitch CPW microwave probes and a Cascade Summit 9000 probe station. An external Short-Open-Load-Thru (SOLT) calibration implementing CPW on an Alumina substrate is used for the two-port calibration. TRL measurements using on-wafer calibration standards have also been done.

A comparison of the measurement and simulation for the resonators is given in Figure 3.14. The measurement and simulation results for all of the resonators are compared in Table 3.3. The agreement between measurement and simulation is generally similar for the seven resonators for both frequency and Q. The coupling is 1.5 dB lower for the measurements than predicted by simulations. Figure 3.6 shows how sensitive the coupling levels can be to the feed inset. A slight error in the fabricated feed inset could account for the coupling levels being lower than predicted. In Figure 3.14, the measured and simulated responses of $R5$ and $R7$ are given with those of the circuit models derived in Section 3.6.

Regarding the miniaturization, the simulated Q_{un} for a cavity resonator using the 5-layer technology is 541; therefore, using $R5$ a 15 % footprint reduction with four supporting posts is realized by sacrificing 6 % of Q_{un}. The values of Q_{un} for $R7$ are 995 and 829 for the simulated and measured results. This compares to a simulated Q_{un} of 1308 for a full-sized cavity resonator with the same cavity height. A 71 % reduction in

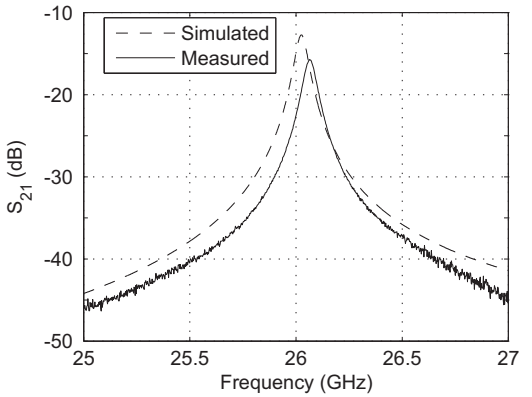

(a) Resonator $R1$

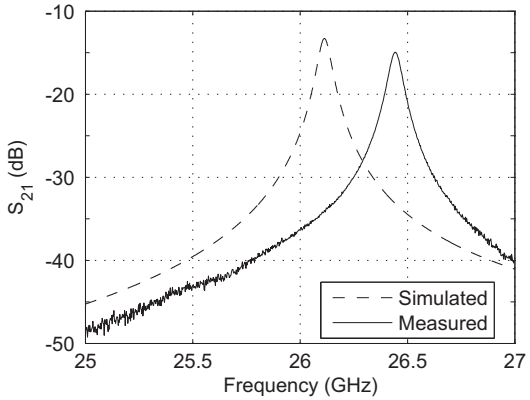

(b) Resonator $R2$

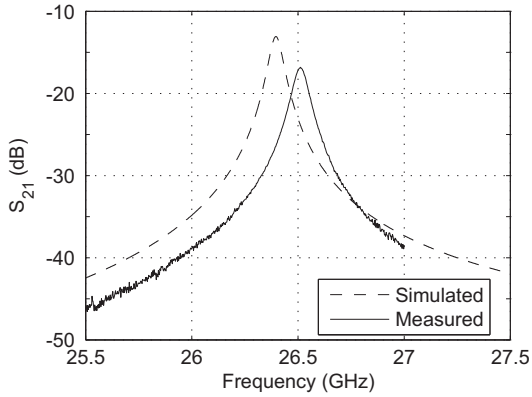

(c) Resonator $R3$

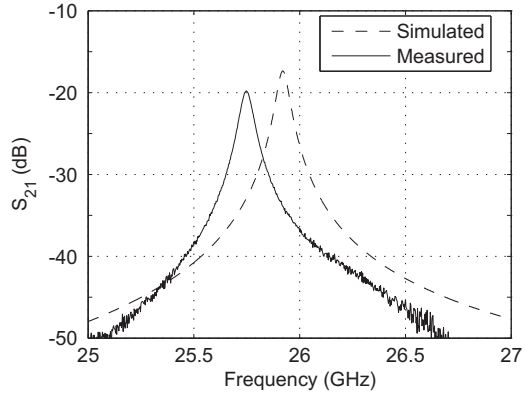

(d) Resonator $R4$

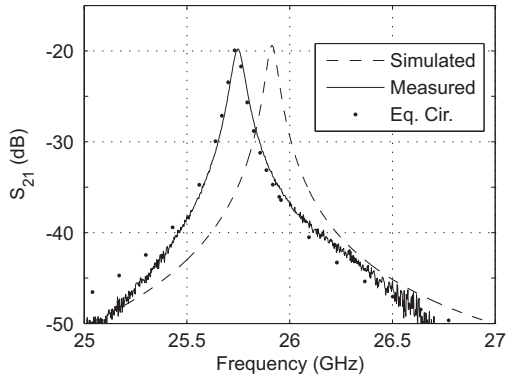

(e) Resonator $R5$

Figure 3.14: The frequency response of resonators $R1$-$R5$ are shown. The measurement and simulation data are compared. (a) $R1$, (b) $R2$, (c) $R3$, (d) $R4$, and (e) $R5$ measurement and simulation, with the circuit model data from Figure 3.15.

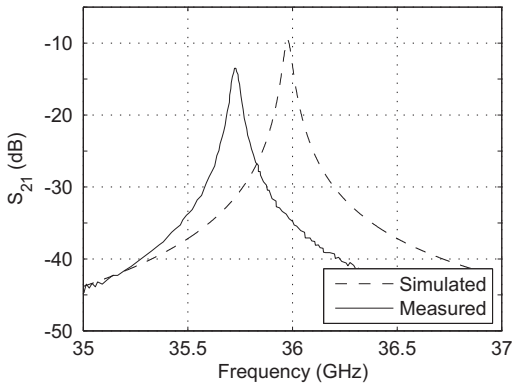

(f) Resonator $R6$

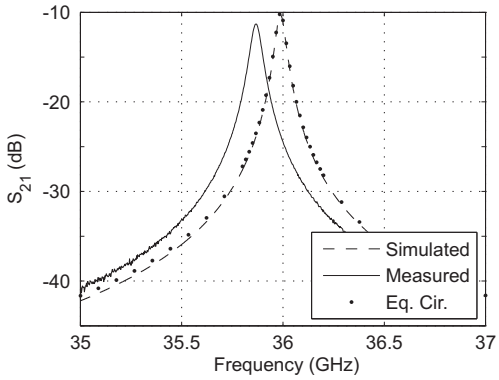

(g) Resonator $R7$

Figure 3.14: The measurement and simulation data of (f) $R6$, and (g) $R7$ are shown. (g) includes the equivalent circuit model from Figure 3.16. ((e) and (g) from [29], © 2007 IEEE. Reprinted with permission.)

Table 3.4: A loss budget detailing the relative contribution in percentage of each structural feature to the overall losses of resonators $R1$-$R5$.

	Resonator				
	$R1$	$R2$	$R3$	$R4$	$R5$
cavity walls	91.8	85.5	86.2	82.6	85.9
feed	3.1	2.8	3.0	1.5	0.8
support post(s)	0.0	7.3	6.3	13.0	6.6
release holes	4.9	4.4	4.4	2.7	2.7
loading mechanism	0.0	0.0	0.0	0.0	4.0
radiation	< 0.1	< 0.1	< 0.1	< 0.1	< 0.2

footprint is thus achievable for a 25 % reduction in Q_{un}.

Loss budgets for the resonators are summarized in Table 3.4. It is clear that the conductor losses of the walls unavoidably dominate, but the other losses may be minimized. For instance, the metal losses in the release holes have a much larger effect on the overall losses of the resonator than the radiation from the holes. One could conceivably change the placement or shape of the holes to decrease losses, without drastically increasing the radiation losses. The 50 % lower losses of the feed of $R4$ compared to the other resonators is due to the smaller coupling of the feed to the resonator (smaller fields around the feed), as seen by S_{21} being lower by approximately 3 dB in Table 3.3, so the coupling levels are seen to have an effect on the unloaded Q.

In addition, loss due to the surface roughness is not taken into account, but would result in a consistent decrease in Q for the resonators. At 26 GHz, we assume that the losses due to the surface roughness are small enough to neglect.

3.6 Circuit-Model Development

Though full-wave FEM simulations are accurate and flexible for detailed studies, they are computationally expensive. For example, on a dual-processor Intel Xeon 3.4 machine it takes four minutes per frequency point to run a simulation with a 70k-

tetrahedron mesh, which generally gives an adequate level of accuracy for these resonators. Therefore, behavioral circuit models are developed for the two loaded resonators and compared with the measured results to validate this approach.

A circuit model, as shown in Figure 3.15(a), is developed for $R5$. The steps for extracting the model are similar to those outlined in [73]. Once the capacitance of the gap, C_g, between the puck and the top wall is approximated using quasi-static analysis, the other circuit parameters can be determined. The other parameters of interest are the series resistance of the feed, R_s; the turns ratio, m, which is approximately the coupling coefficient; the total inductance of the support posts, L_s; the characteristic impedance of the lines connecting to the resonator, Z_o; and the nominal capacitance, resistance, and inductance of the cavity, C_n, R_n, and L_n, respectively. Starting values for these parameters are found using full-wave analysis, and then the parameters are fit to correspond to the measured results. Good agreement can be seen between the measured response and the derived equivalent circuit, Figure 3.15(b). The calculated values for the circuit parameters are Z_o=50 Ω, R_s=0.15 Ω, m=0.03 turns, C_g=0.28 pF, C_n=0.56 pF, L_s=264 pH, L_n=54 pH and R_n=3.22 kΩ. A similar exercise using the simulated S-parameter data from the full-wave response yields a circuit model whose input impedance is indistinguishable from that calculated in the simulation.

Figure 3.16(a) shows the model and Figure 3.16(b) the input impedance predicted by the model, as compared with the simulated input impedance for the rib-loaded resonator, $R7$. A comparison with the simulated results demonstrates that the circuit model predicts the measured response and agrees with the full-wave simulations. The circuit model has one inductor fewer than the model in Fig 3.15(a), as there are no support posts in this design. The loading capacitance from the ribs, C_L, is calculated using Ansoft's Maxwell 3D, as the approximation of the capacitance is more involved than what was done for the loading puck. This method calculates the electrostatic capacitance, but this is a good approximation since the dimensions of the loading ribs

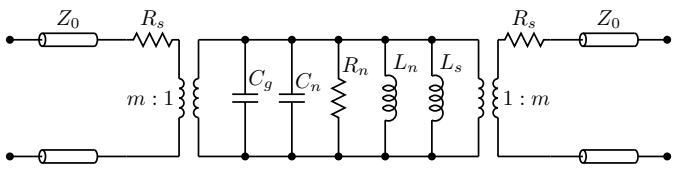

(a)

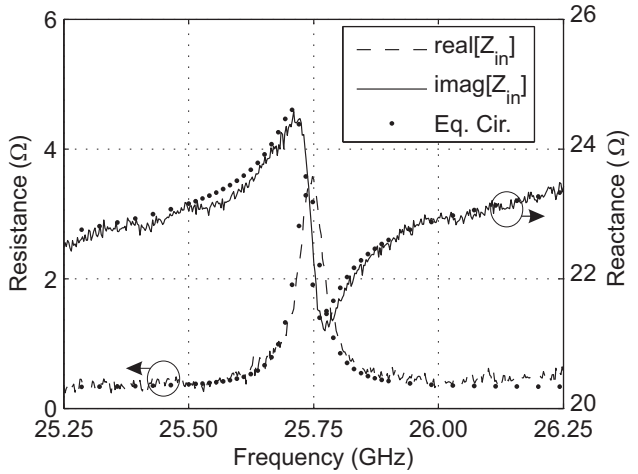

(b)

Figure 3.15: An equivalent circuit is generated for the resonator with feed combination for the miniaturized resonator using a loading puck and support posts. (a) The circuit topology used to create the model. (b) The measured input impedance of the resonator/feed combination compared to the input impedance of the circuit model derived from the measured data. (From [29], © 2007 IEEE. Reprinted with permission.)

are less than $\lambda_0/10$ at the resonant frequency. C_L is 0.068 pF. The nominal capacitance of the resonator is C_n=0.029 pF, the nominal inductance is L_n=0.203 nH, the nominal resistance R_n=45.73 kΩ, the turns ratio is m=0.016, and the series resistance of the feed is R_s=0.3 Ω.

The resonant frequency of a simple parallel resonator is given as

$$f_0 = \frac{1}{2\pi\sqrt{C_n L_n}} \tag{3.9}$$

and with the loading,

$$f_0 = \frac{1}{2\pi\sqrt{(C_n + C_g)\left(\frac{L_n L_s}{L_n + L_s}\right)}} \tag{3.10}$$

Using the above equations, the component values of the circuit model are found.

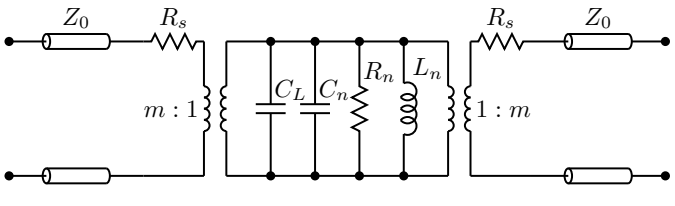

(a)

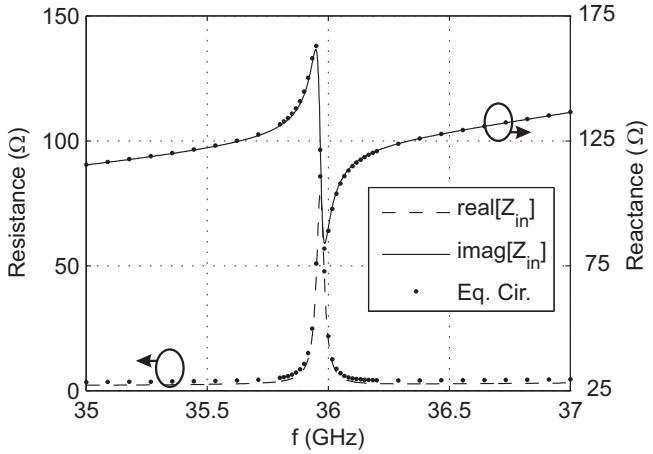

(b)

Figure 3.16: An equivalent circuit is generated for the resonator with feed combination for the miniaturized resonator using three ribs for miniaturization. (a) The circuit topology used to create the model. (b) The simulated input impedance of the resonator/feed combination and the input impedance of the circuit model derived from the simulated data. (From [29], © 2007 IEEE. Reprinted with permission.)

An examination of the derived circuit models of the two miniaturized resonators presented in Figure 3.15(a) and Figure 3.16(a) reveals that quite similar behavioral models describe the two resonators with seemingly different loading topologies. This approach can be generalized to other possible quasi-planar loading topologies.

3.7 Discussion of Resonator Results

The top wall of the resonators in the initial fabrication batch exhibited an upward "bowing" effect due to top-wall strain. The process was subsequently refined to produce flat walls, however it is interesting to note the bowing increased both the resonant frequency and the Q of the resonator. The resonant frequency increases because the overall capacitance between the top and bottom walls decreases with the increased separation. The increase of the interior volume from the bowing also increases the Q. Surface profile cuts for a $R1$ resonator with the bowing are shown in Fig. 3.17(a). The cuts are made for the center to the edge of the resonator between the rows of release holes over a quarter of the geometry. The surface profile measurements were made using a Zygo laser interferometer. The bowing increases H by $60\,\mu$m near the center of the cavity. Fig. 3.17(b) illustrates a comparison of performance for $R1$ with and without the top-wall bowing. The resonant frequency and loaded Q of the resonator are predicted using 3-D FEM and the simulation and measurement for the two cases are shown in the figure. With bowing, the measured Q is 684 and the resonant frequency is 26.82 GHz. The simulated Q is 661 and the simulated resonant frequency is 26.78 GHz, calculated using eigenmode analysis. The bowing of the top surface of the resonator is approximated using six curvilinear surfaces in the model geometry as shown in Figure 3.17(d). The dimensions are those given in Table 3.1 for $R1$, except the top surface bows to a maximal vertical displacement of $60\,\mu$m.

The resonator work presented here can be extended into several areas. Filters are of interest using this technology and a few initial designs have been examined, as

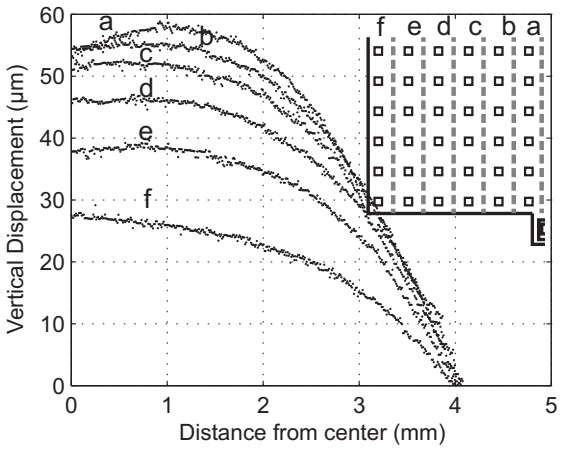

(a)

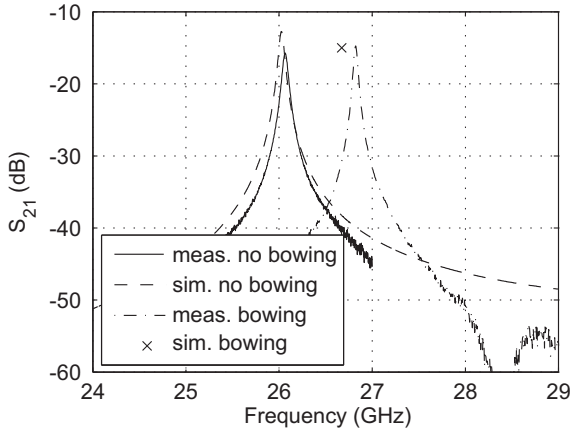

(b)

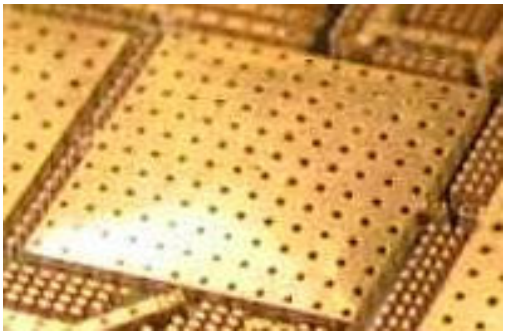

(c)

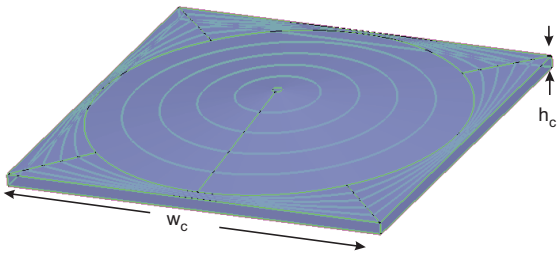

(d)

Figure 3.17: (a) The surface profile for a quarter of the top wall of a bowed $R1$. An inset indicating the location of the cut planes with dashed gray lines is shown in the upper right corner. This bowing was subsequently eliminated by changing the fabrication process. (b) The measured and simulated S-parameter data for the cavity resonator are given for the cases with and without bowing. (c) A photograph highlighting the bowing of one of the $R1$ resonators. (d) The frequency shift exhibited by resonators with bowing can be accounted for by including the bowing in the models with an approximation of the top surface using a six-curvilinear-surface approximation. ((a) and (b) from [31],)

discussed in Section 6.2.3. Additionally, compact, high-quality resonators are essential for the construction of low-power, low-phase-noise oscillators [74]. Work has been done at the University of Colorado for chip-scale atomic clocks with commerically available coaxial transmission-line resonators having Q_{un} below 250. This might prove to provide an architecture amenable to larger values of Q.

Chapter 4

Four-Port Couplers

Hybrid couplers are commonly used as components of microwave and millimeter-wave front ends. Quadrature hybrids include narrow-band branch-line and broadband Lange directional couplers, usually implemented in microstrip. This chapter presents branch-line couplers made of sections of rectangular coaxial cable fabricated using the PolyStrata^{TM} technology. Previous work in this area includes rectangular coaxial branch-line couplers fabricated in the EFAB^{TM} process by Microfabrica for operation in the *Ka*- and *V*-bands [10, 11]. Although small, rigid devices with excellent performance have been reported, this process uses nickel, with twice the loss of copper for the same transmission-line cross section. Initial results for a 26-GHz air-filled branch-line coupler and other components using the copper-metal PolyStrata^{TM} process are presented in [32] and will be the subject of Section 4.1. Each of these previously reported couplers is unbalanced, as expected [75], but to a degree which is not acceptable for many applications, such as antenna feed networks. In one case, the return loss is maximized at a frequency 2 GHz lower than the center frequency for good output amplitude balance [11]. This is due to parasitic reactances from T discontinuities in the coupler. Because of the resonant nature of the branch-line architecture, even small parasitics can have a large effect on the output port balance. In Section 4.3, we present techniques for achieving excellent phase and amplitude balance in the same frequency range as that for best match and isolation. Without the presented methods, a 4 % difference in frequency

(1.5 GHz) would be observed in couplers that are otherwise the same. The branch-line couplers of Section 4.2 suffer from this problem as well.

Another method to potentially improve the performance of 90° hybirds is to use a Lange coupler, as seen in Section 4.4. Prior to Lange couplers, fabrication of 3-dB coupled-line directional couplers using planar fabrication techniques was difficult because of the tight line spacings necessary for high coupling [76]. By using an interdigitated coupling structure, tight coupling became possible, and these couplers provide wider-band frequency performance than branch-line couplers. Limiting factors of the design include the parasitic reactances associated with the wire bonds, their repeatability, and the tolerances for line dimensions. Alternative configurations of the Lange coupler have included the 'unfolded' Lange coupler, requiring fewer wire bonds [77]. A comprehensive study of both symmetric and asymmetric multilayer directional couplers at frequencies below 8 GHz is given in [78]. Micromachining of Lange couplers using membrane suspended stripline has produced a 3.6±0.8 dB bandwidth from 6.5 to 20 GHz [79].

Directional couplers using a pair of coupled lines are shown in Section 4.5. A 10-dB and a 20-dB coupler are demonstrated with the operating frequency at 26 GHz. Similar analysis methods to those used for the Lange coupler are employed for the design.

4.1 26-GHz Branch Line Couplers

Nine branch-line couplers are designed for operation at 26 GHz. The characteristic impedance of the branch-line and the length of the coupler branches are varied to provide an understanding of how much the two parameters effect the performance. Figure 4.1(a) shows a sketch of the branch-line coupler topology with the basic design parameters indicated. Figure 4.1(b) shows an SEM of one of the fabricated 26-GHz branch-line couplers. The characteristic impedance of the lines between ports one and two and

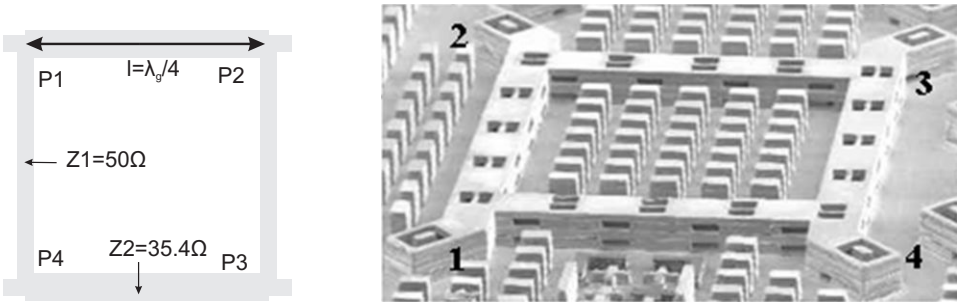

(a) (b)

Figure 4.1: (a) A sketch of the basic parameters of interest for the design of a branch-line coupler. (b) An SEM of a branch-line coupler designed for operation at 26 GHz. ((b) from [32], © 2006 IEEE. Reprinted with permission.)

ports three and four is 50 Ω. The characteristic impedance of the lines between ports one and four and ports two and three is $(50/\sqrt{2})\,\Omega$. The lengths of each of the line segments is 90° at the center design frequency. The dimensions for the nine hybrid designs are given in Table 4.1. The magnitude of the S parameters for excitation at port 1 are given in Figure 4.2. A comparison of the simulated and measured output magnitudes and phases for the nine designs are given in Figure 4.3 and Figure 4.4, respectively. The four-port de-embedding of Section 2.4.1 has not been applied to these data.

4.2 36-GHz Branch Line Couplers

A branch-line coupler operating at 36 GHz is designed. This uses a similar design to that described in the previous section. Figure 4.6 shows a model of the branch-

Table 4.1: The parameters used for the nine branch-line coupler designs.

	Z_2=33.8 Ω	Z_2=34.8 Ω	Z_2=35.8 Ω
L = 85°	H5	H4	H6
L = 90°	H2	H1	H3
L = 95°	H8	H7	H9

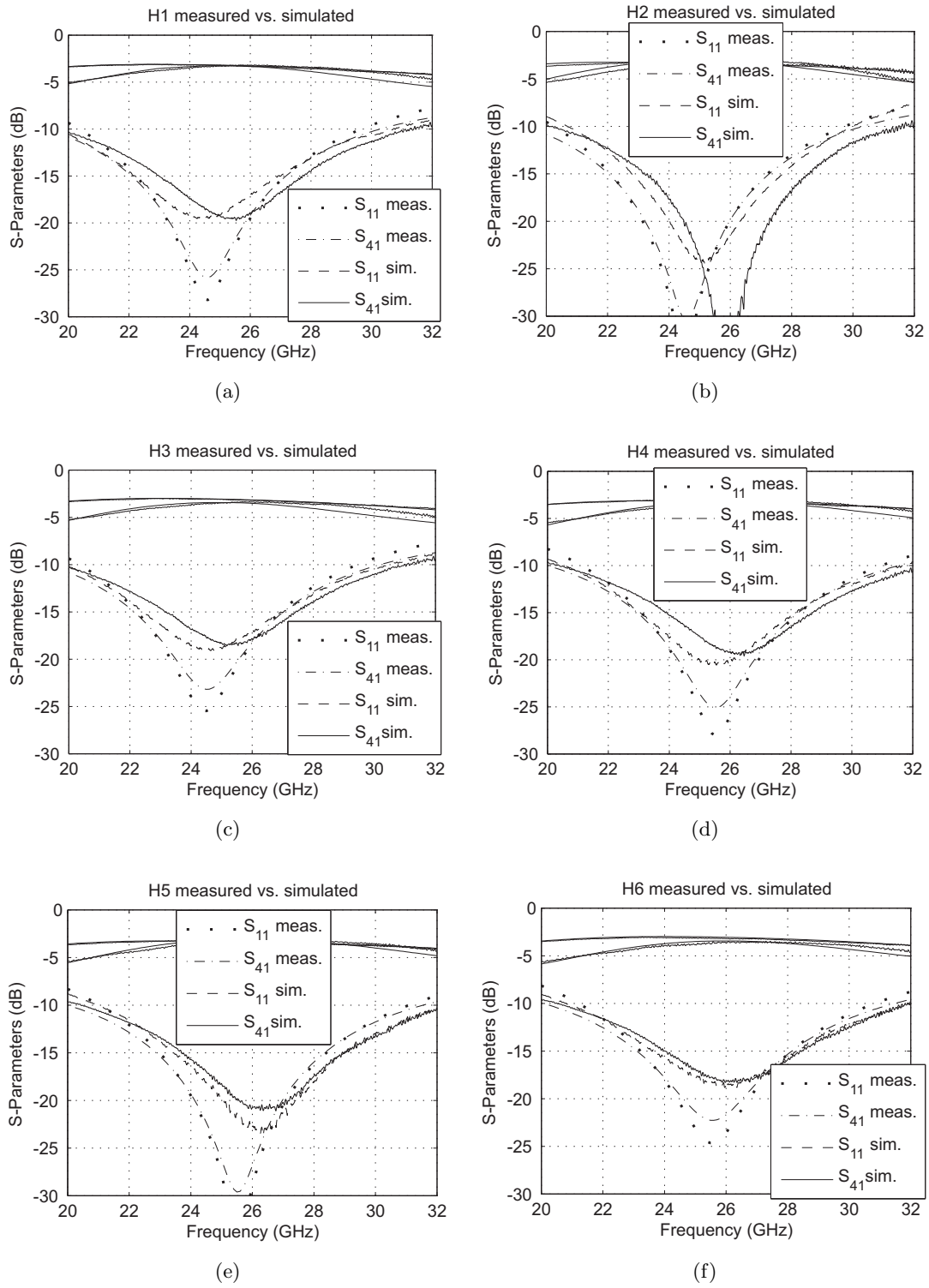

Figure 4.2: The measurement and simulation data for the S Parameters associated with an excitation at port 1 (S_{i1}) are given. The labeling of the hybrids H1-H9 corresponds to the dimensions given in Table 4.1. (Note: The legend is placed over the traces for S_{21} and S_{31} where unavoidable because Figure 4.3 shows that data.) (a) H1, (b) H2, (c) H3, (d) H4, (e) H5, and (f) H6.

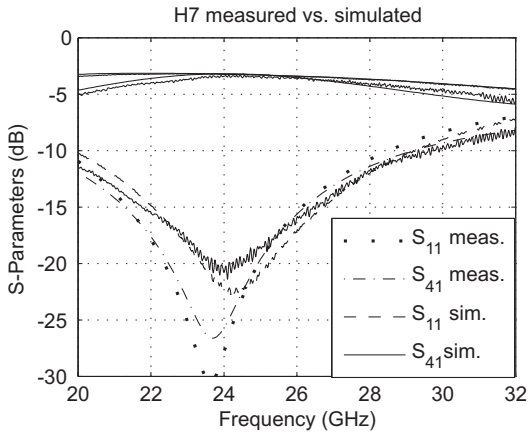

(g)

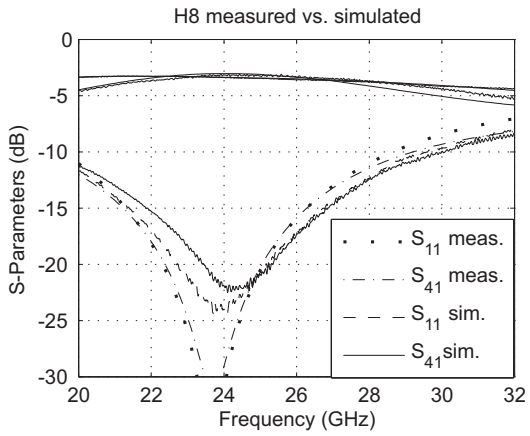

(h)

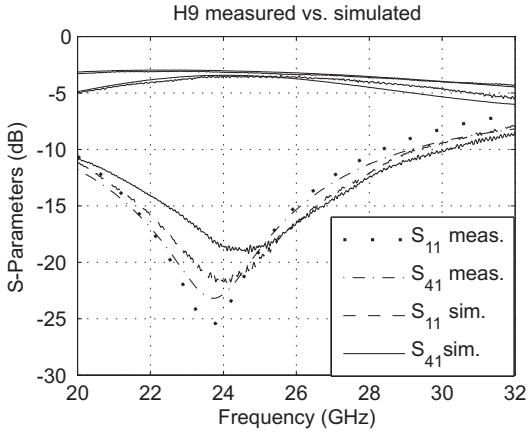

(i)

Figure 4.2: (g) H7, (h) H8, and (i) H9. (cont.)

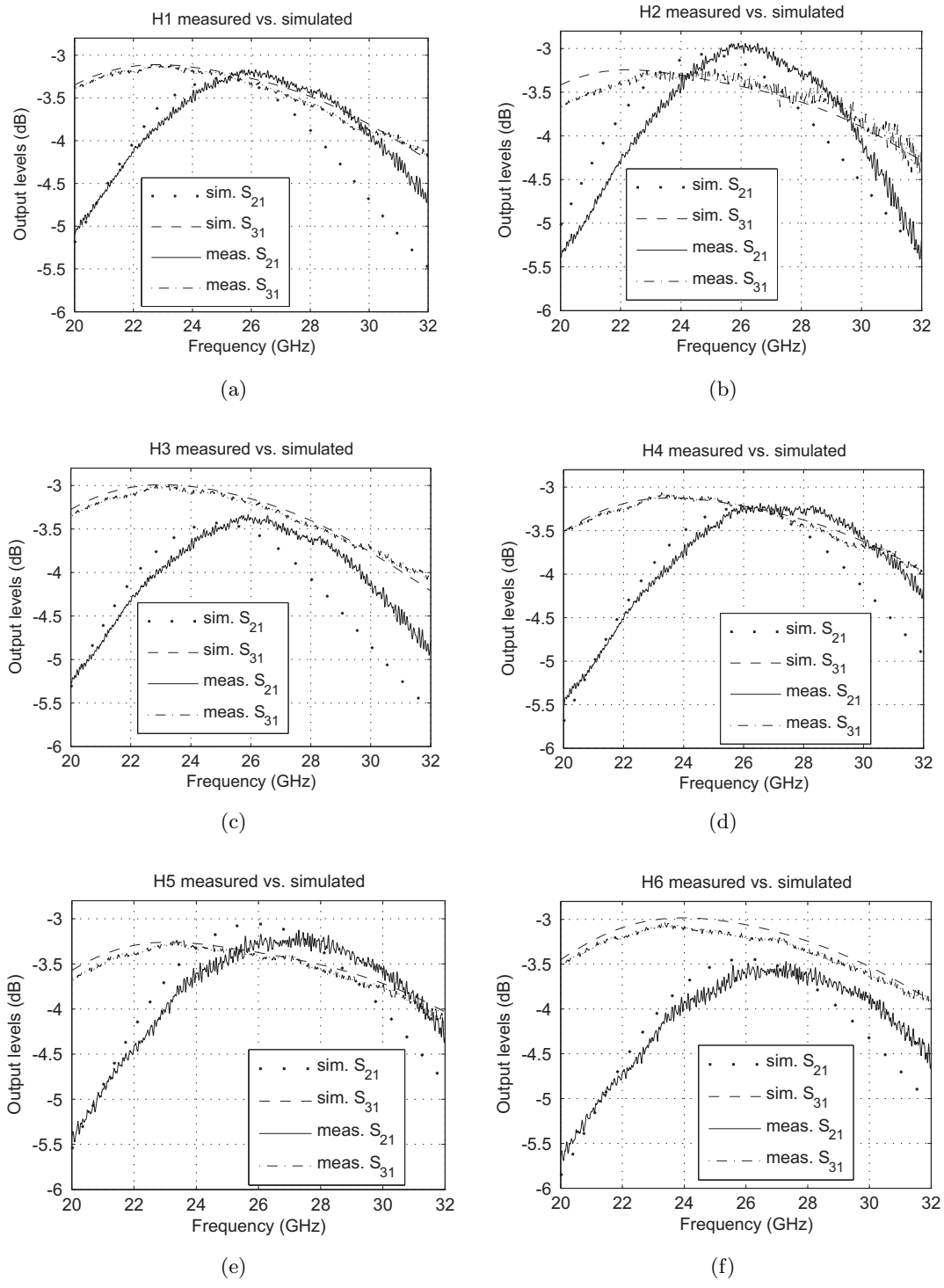

Figure 4.3: The measurement and simulation data for the output S Parameters associated with an excitation at port 1 (S_{21} and S_{31}) are given. The labeling of the hybrids H1-H9 corresponds to the dimensions given in Table 4.1. (a) H1, (b) H2, (c) H3, (d) H4, (e) H5, and (f) H6.

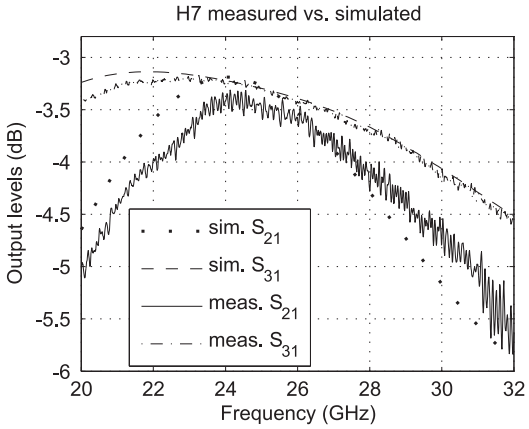

(g)

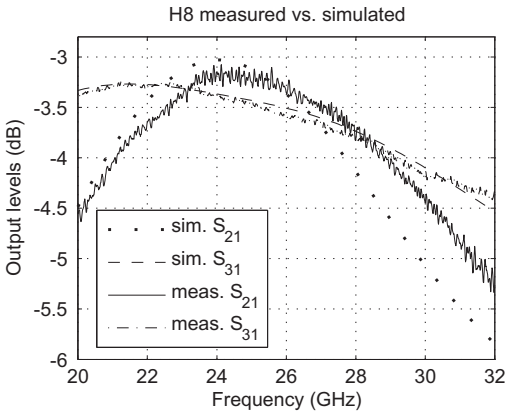

(h)

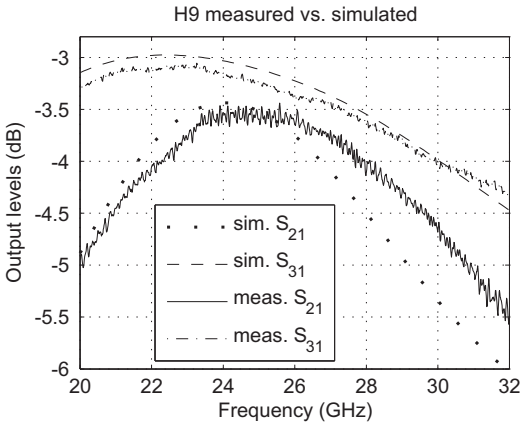

(i)

Figure 4.3: (g) H7, (h) H8, and (i) H9. (cont.)

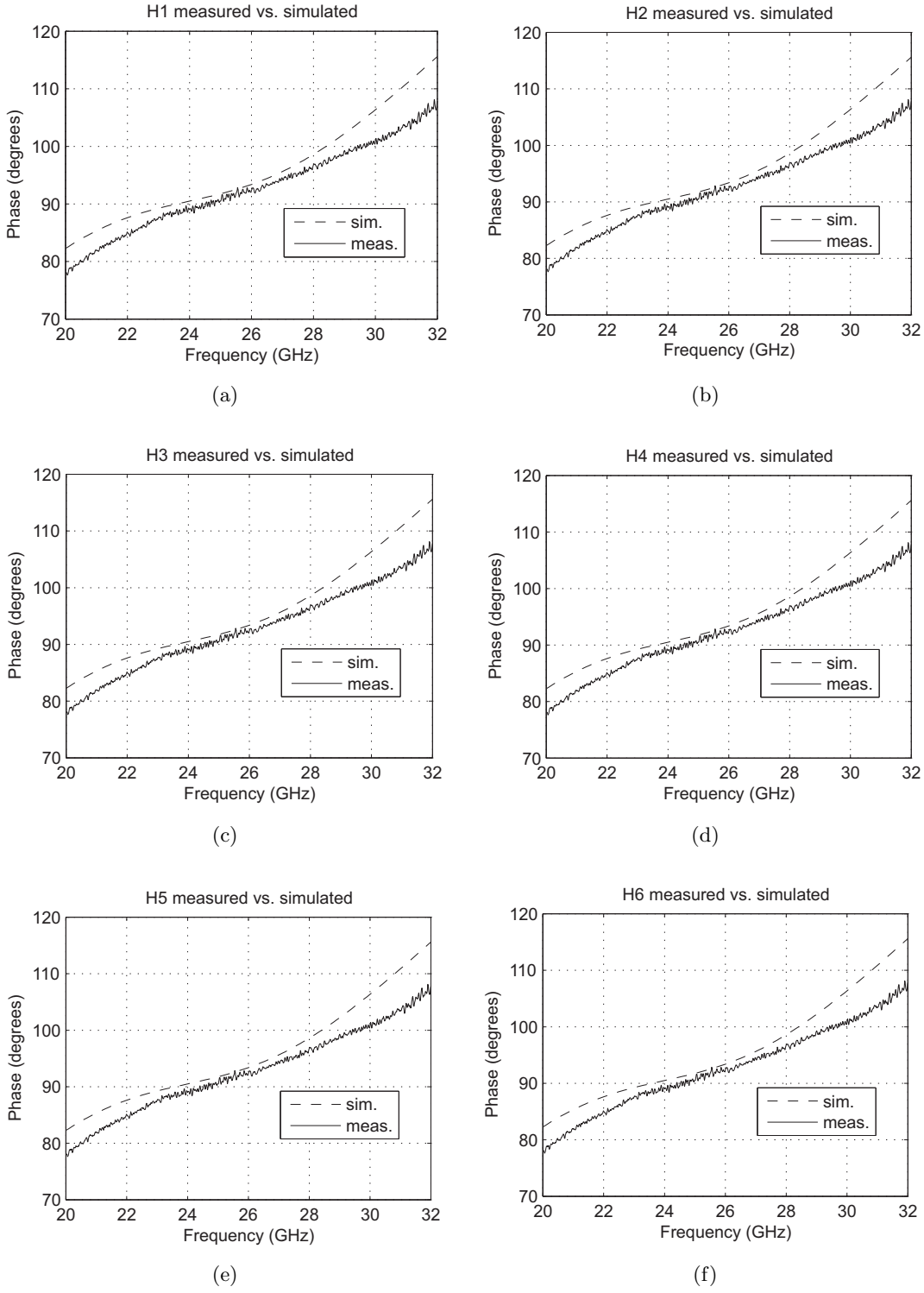

Figure 4.4: The measurement and simulation data for the output S Parameters associated with an excitation at port 1 (S_{21} and S_{31}) are given. The labeling of the hybrids H1-H9 corresponds to the dimensions given in Table 4.1. (a) H1, (b) H2, (c) H3, (d) H4, (e) H5, and (f) H6.

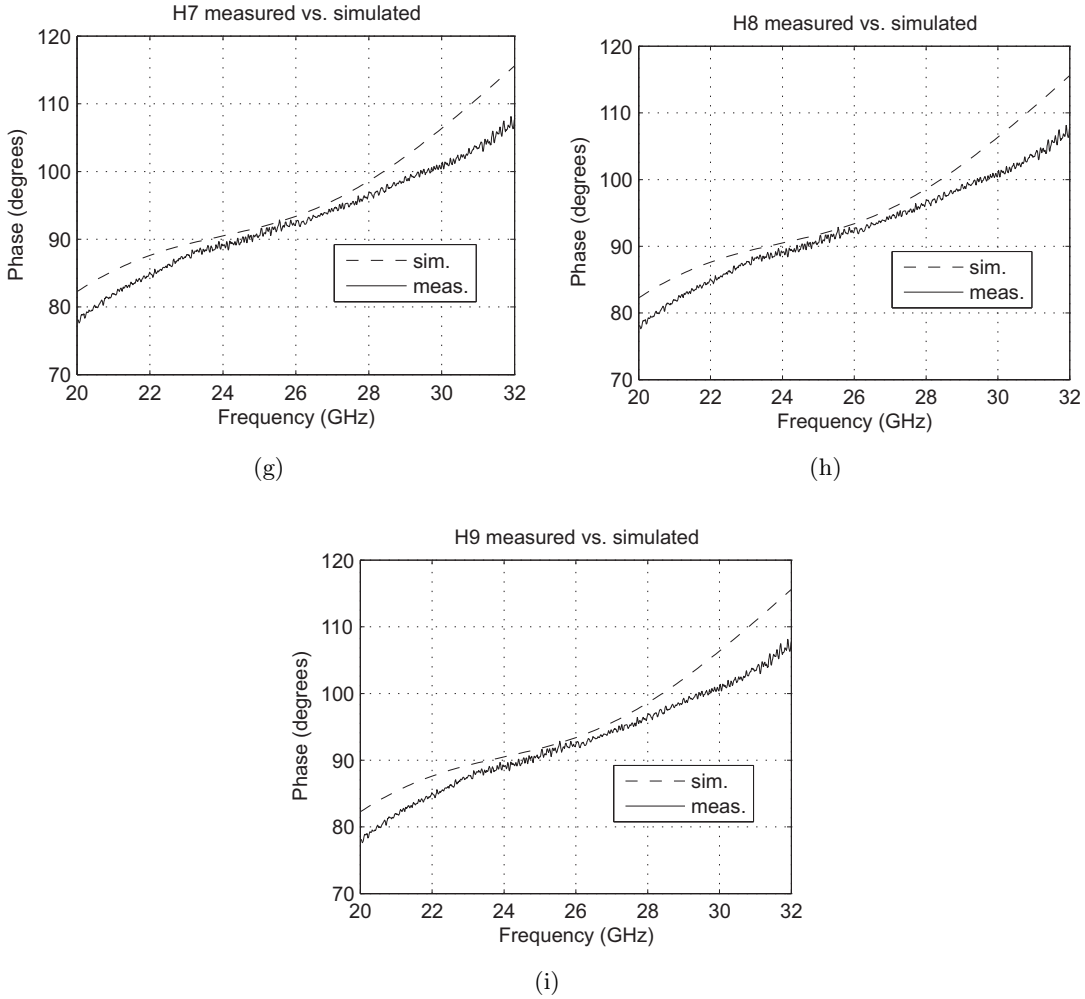

Figure 4.4: A comparison of the simulated and measured results for the phase difference between the output ports for the nine hybrid designs. (a) H1, (b) H2, (c) H3, ... and (h) H9. (cont.)

line coupler with the relevant dimensions and features indicated. Figure 4.5 shows the measured and simulated data for the branch-line coupler shown in Figure 4.6. The four-port de-embedding of Section 2.4.1 is used on the measured data.

The uncompensated T junctions within a branch-line coupler produce an offset in the frequency performance for the parameters of interest. For this discussion, two frequencies and their difference are of interest:

$$f_1 = f(\min\{|S_{11,41}|\}) \tag{4.1}$$

$$f_2 = f(\max\{S_{21}(\text{dB}) - S_{31}(\text{dB})\}) \tag{4.2}$$

$$\Delta f = f_1 - f_2 \tag{4.3}$$

For the couplers presented here, the theoretical minimum values of S_{11} and S_{41} occur at virtually the same frequency; however, the average of the two frequencies is taken if this is not the case. An example illustrating Eqs. (1)-(3) is shown in Figure 4.8 for the simulated values of a branch-line coupler without junction compensation; $\Delta f = -1.5\,\text{GHz}$ for a center frequency near 36 GHz.

4.3 Balanced 36-GHz Branch-Line Couplers

A variety of discontinuity compensation techniques have been demonstrated for improved microstrip circuit performance, e.g. [80,81]. T-junction compensation of coaxial transmission lines has been examined, but quarter-wave sections were used for impedance matching, which is not always practical [59]. In [75], the stripline junctions are compensated by changing the impedance and lengths of the branches of the coupler. Two compensation techniques amenable to the PolyStrata^{TM} process are presented in this paper: (1) length compensation of the 50-Ω segments; and (2) modification of the T-junction geometry.

A layout of a rectangular μ-coaxial branch-line coupler with relevant dimensions

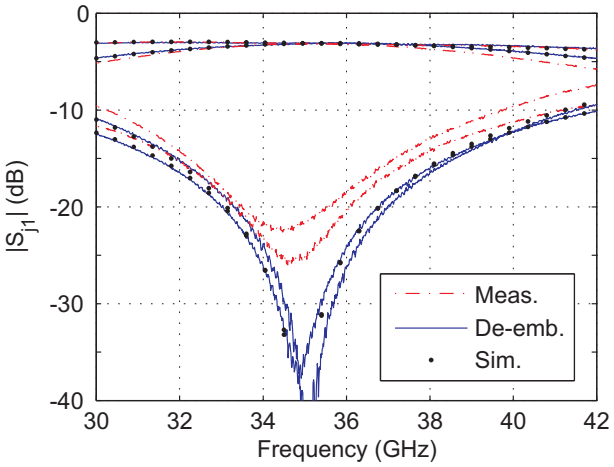

(a)

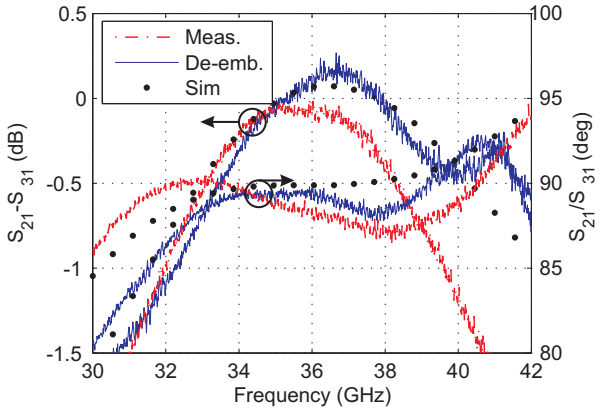

(b)

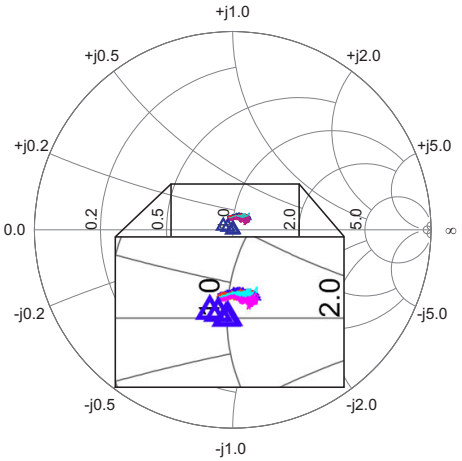

(c)

Figure 4.5: (a) The measurement results with and without the implementation of the de-embedding described in Section 2.4.1 are compared to the simulated results with the probe transitions omitted for an uncompensated 36-GHz branch-line hybrid. (b) The measurement results at the output ports with and without the de-embedding for both the phase and amplitude. (c) S_{22} for each of the error boxes at the four ports compared to the simulated value plotted on a 50-Ω Smith chart. S_{22} of the simulated error box is shown with '△'. ((a) and (c) from [30],)

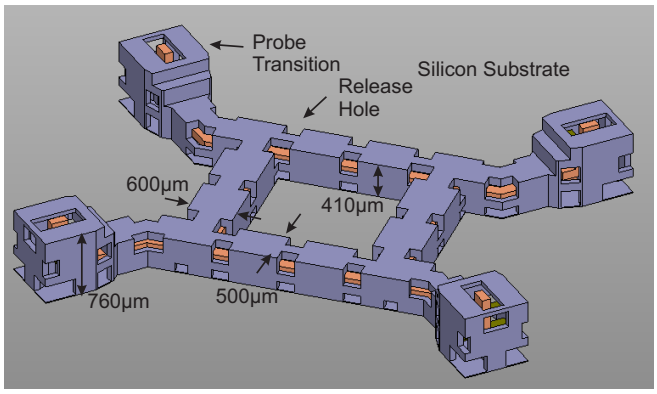

Figure 4.6: Layout of a rectangular μ-coaxial branch-line coupler fabricated on a low-resistivity Si substrate using the PolyStrata^{TM} process. The 50-Ω transmission lines have a $139 \times 100\,\mu\text{m}^2$ center conductor and 300-micron square outer conductor. Periodic thin dielectric straps support the center conductor. The holes in the metal serve to drain the photoresist. A 150-mm diameter substrate contains over 1000 passive components fabricated in a parallel process. (From [30],)

for the PolyStrata^{TM} process is shown in Fig. 4.6. Probe connections are fabricated in the same process at each of the ports of the device to enable measurements using standard 150-μm coplanar waveguide (CPW) probes. The probe connection discontinuity is de-embedded from externally-calibrated four-port measurements and known on-wafer two-port standard parameters. It is shown that de-embedding is required to adequately measure high-quality couplers that show very small deviations in output amplitude and phase.

4.3.1 Fabrication and Modeling

The devices are fabricated using the PolyStrata^{TM} process, consisting of sequentially depositing layers of metal and photoresist on a low-resistivity silicon host substrate [28]. Each layer is chemically planarized before the next one is deposited, and the copper layers are limited to an aspect ratio of 1.5:1. 100-μm-wide polymer straps support the center conductor and are placed along the line with a 700-μm period. The final step involves selectively etching the photoresist to leave air-filled copper components, with a dielectric-to-air volume ratio of approximately 0.5 %. A photograph of the two fabricated couplers is shown in Fig. 4.7.

The devices are modeled using Ansoft HFSS^{TM}. The 3-D finite element method (FEM) is chosen for its flexibility with arbitrary geometries and ability to handle diverse material properties. In addition, the holes left in the copper for dissolving away the photoresist are designed to radiate minimally (< -40 dB), and the FEM is well suited for closed metallic structures, as discussed in [29]. Simplified models with no support straps and photoresist release holes are used to obtain an approximate design efficiently, which is followed by simulations and optimization of the final physical model. The simulation results are presented with the measurements in Section 4.3.2. The cross section of the 50-Ω line is 100 μm tall by 139 μm wide for the inner conductor and 300 μm by 300 μm for the outer conductor spacing. The 35-Ω line is 100 μm tall by 265 μm wide for the

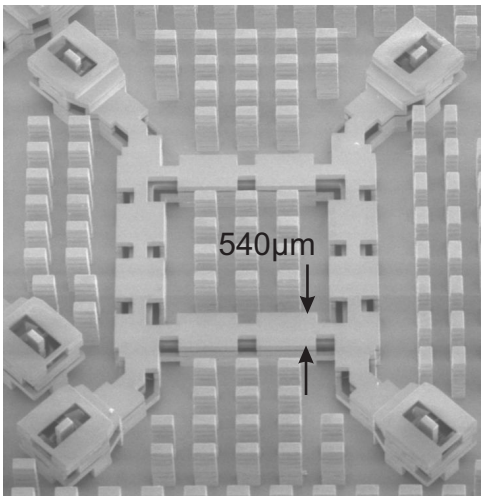

(a)

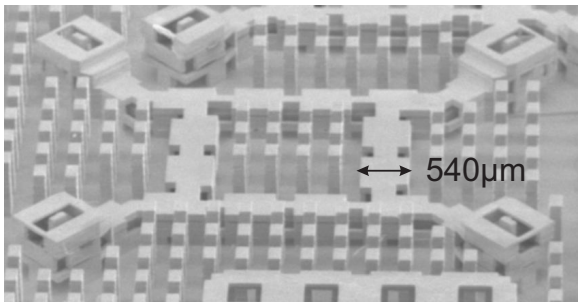

(b)

Figure 4.7: SEM images of the fabricated couplers: (a) the length-compensated quadrature coupler and (b) the T-junction compensated. (From [30], © 2007 IEEE. Reprinted with permission.)

inner conductor and 300 μm tall by 400 μm wide for the outer conductor spacing. The wall thicknesses are 70 μm on the sides, and 20 μm and 50 μm on the bottom and top, respectively.

The two methods of compensation are shown in Fig. 4.9. The length compensation is achieved by increasing L_b by 11 % for the 50-Ω sections, while L_a for the 35-Ω sections remains $\lambda/4$. The T compensation is designed using a reactive equivalent circuit model derived from full-wave simulated S parameters. Additional series inductance in each of the arms of the T junction and a small amount of shunt capacitance are needed to optimize the performance of the junction, as shown in Fig. 4.9.

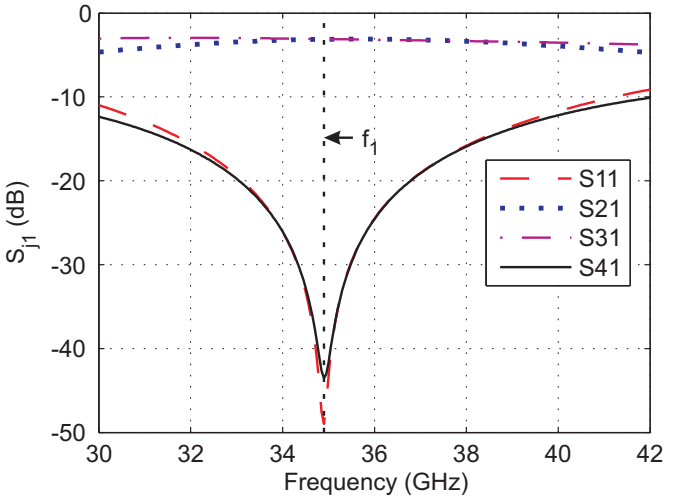

(a)

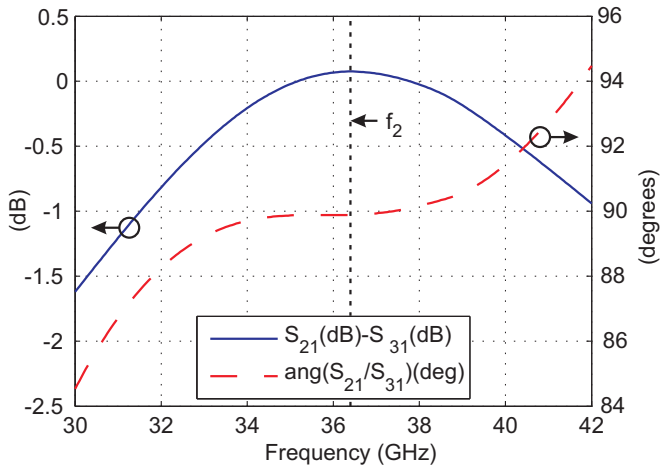

(b)

Figure 4.8: Simulated results showing the two frequencies of interest for the analysis of the frequency offset caused by the parasitic junction reactances. (a) f_1 is identified for the minimum of S_{11}. (b) f_2 is the frequency where the amplitude difference between the through and coupled ports is maximal. (From [30],)

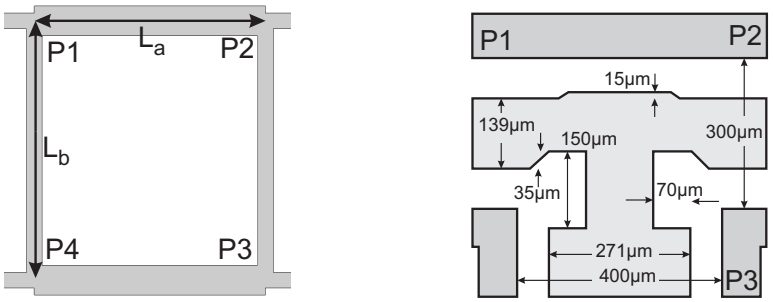

Figure 4.9: (a) Sketch of length-compensated hybrid. The segments for the length-compensated quadrature hybrid are shown to scale. The two lengths of interest are $L_a = 2.08\,\text{mm}$ and $L_b = 2.33\,\text{mm}$. (b) Sketch of the reactively-compensated T junction, with P1, P2 and P3 connected to the input, isolated and coupled ports, respectively. (From [30], © 2007 IEEE. Reprinted with permission.)

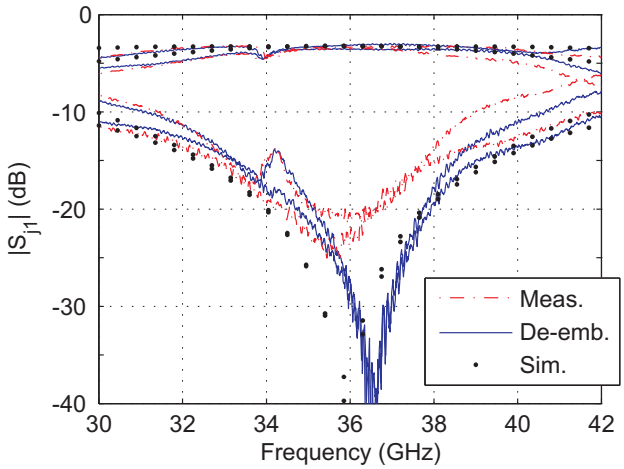

Figure 4.10: The simulated, measured, and de-embedded S-parameters in dB for port one being excited of the length-compensated branch-line coupler. (From [30], © 2007 IEEE. Reprinted with permission.)

4.3.2 The Measurement and Results for Balanced Branch Line Couplers

The measurements are conducted using a four-port network analyzer over a frequency range from 30-42 GHz with a probe station equipped with four probes, two of them oriented North-South, and the other two oriented perpendicularly (East-West). A two-tier calibration method is performed. An external four-port SOLT calibration is performed off-wafer on an Alumina substrate, calibrating to the tips of the microwave probes. In this step, the interaction between the probes and the on-wafer probing structures is not completely calibrated out of the measurement. Additional steps, according to the calibration method outlined in Section 2.4.1, are performed.

The measurement results with and without the de-embedding of Section 2.4.1 for the length-compensated branch-line coupler are shown in Figure 4.10. After de-embedding, the return loss and isolation are better than 20 dB from 35.2 to 37.7 GHz with the measured f_1 at 36.5 GHz. The output phase difference is $90° \pm 5.0°$ from 34.0 to 38.2 GHz and the output amplitude difference is 0.0 dB $\pm$ 0.25 dB from 34.2 to 37.5 GHz. f_2 is at 37.0 GHz, so Δf is 0.5 GHz compared to 1.5 GHz without compensation.

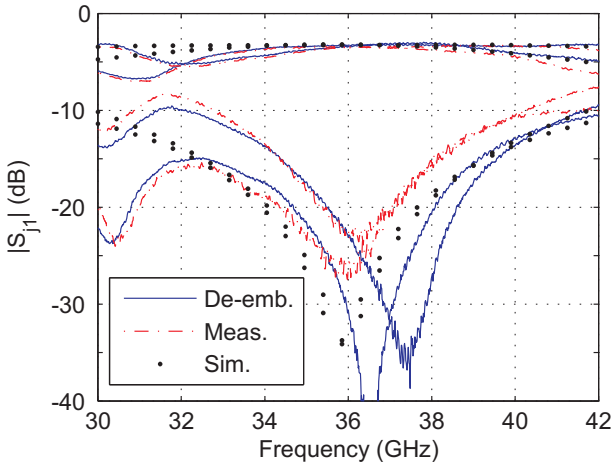

Figure 4.11: The simulated, measured, and de-embedded S-parameters in dB for port one being excited of the tee-compensated branch-line coupler. (From [30], © 2007 IEEE. Reprinted with permission.)

Fig. 4.11 provides the measured values for the branch-line coupler using T-junction compensation for improved performance. The return loss and isolation are greater than 20 dB from 35.5 to 38.2 GHz. The average of the minima of S_{41} and S_{11} gives f_1 at 37.0 GHz. The measured output phase difference is $90° \pm 5.0°$ from 34.0 to 42 GHz, and the output amplitude difference is ± 0.25 dB from 35.5 to 37.8 GHz ($f_2 = 38.1$ GHz). Δf is <0.2 GHz; both methods of compensation give measured frequency performance better than what is seen without compensation.

4.3.3 Discussion of Balanced Branch Line Couplers

The compensation of branch-line couplers in microfabricated rectangular coax is presented in this paper. Two methods are demonstrated with improvement in the frequency response of the couplers. One coupler employs a modification of the branch lengths to accomplish the compensation and the other uses a modification of the T junctions. Additionally, de-embedding of the probe transitions has been performed producing better agreement between measurement and simulation than off-wafer calibrations would normally allow, as visible in Figure 4.5. For this case, the coupling and

transmission are 3.30 dB ± 0.10 dB from 34 to 37.5 GHz. By de-embedding, the probe-to-transition mismatch has been removed, and it has been shown that the performance of fabricated millimeter-wave devices using the PolyStrata^{TM} process is predicted extremely well using full-wave simulation methods.

Although we currently do not have compensated branch-line couplers that are fabricated as well as the uncompensated hybrid from Figure 4.5, an increase in operating bandwidth is possible. Simulations predict a 100 % increase in bandwidth as compared to the uncompensated case with the return loss and isolation better than 20 dB, the output amplitudes of 3.2 dB ± 0.1 dB, and the output phase differences of 90° ± 2.0°.This is partially due to increasing the overlap of the desired bandwidths around f_1 and f_2 and partially due to an increased performance bandwidth when the two frequencies coincide.

The couplers presented here are only two of more than 1000 components that are fabricated on a single 150-mm diameter silicon wafer. Such high-quality batch-fabricated components can be integrated into larger sub-systems in the same fabrication process. For example, the couplers presented here will be integrated into a beam-forming Butler matrix requiring a number of hybrids with small values of Δf.

4.4 36-GHz Lange Couplers

The present work demonstrates the design, fabrication and measurement of a 3-D Lange coupler. This coupler does not suffer from the traditionally limiting differences between the even- and odd-mode phase velocities because the coupling section is completely air filled. A mechanical model is shown in Figure 4.12 with the top wall removed to show the internal structure of the coupler. Because of the multilayer process used to fabricate the devices, wire bonds are not required to tie together interdigital lines of the same potential, increasing the repeatability of the fabricated couplers. These couplers are seamlessly integrated with other millimeter-wave components using the same

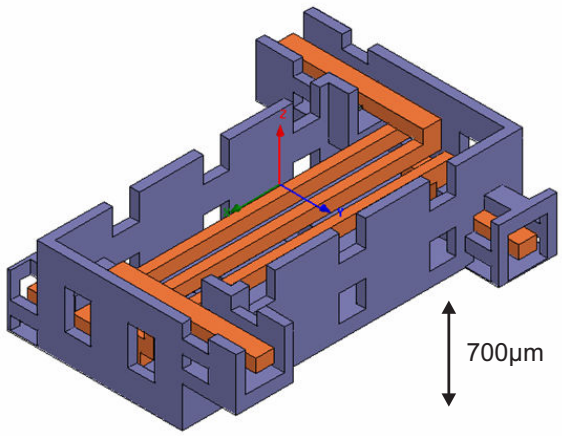

Figure 4.12: A mechanical model of the Lange coupler. The probe connection areas are omitted and the top metal layer is removed.

fabrication process.

4.4.1 2-D Design Aspects of the Lange Coupler

For the desired coupling, high isolation, and well-matching input ports, an accurate calculation of the even- and odd-mode impedances for different dimensions of the coupled transmission-line is required. Classical directional couplers are implemented using stripline or microstrip with the signal conductors lying in the same plane; however, other coupled transmission line topologies exist. Several directional couplers with both tight and low coupling levels using multi-layer structures are presented in [82]. In addition, broadside couplers on gallium arsenide have also been reported with better than 20-dB isolation from 20 to 40 GHz [83]. In this paper, because of fabrication driven process requirements, the coupling must be done using a non-canonical transmission line configuration. Several methods have been used to compute the even- and odd-mode impedances in the past. Initial design methods seemed to be empirically based, however Ou formulated admittance equations to describe the coupling [84]. Design curves for a few microstrip Lange configurations were given in [85], calculated using numerical methods. A numerical implementation of conformal mapping has been used to design

directional couplers, giving accurate results [86]; however, symmetry is necessary in one plane, although the analysis of multiple conductors is possible. Because our line cross sections do not fit these constraints, the characteristic impedances for different cross sections must be calculated by other means.

We use COMSOL *Multiphysics* to solve for the electric potential of the cross-section using Laplace's equation with the 2-D finite element method. The characteristic impedances are found using $Z_0^e = 1/cC_e$ and $Z_0^e = 1/cC_o$, where C_e and C_o are the calculated even- and odd-mode capacitances and c is the speed of light. The impedances for different values of w and g (from Fig. 4.13) that are possible to fabricate and potentially useful are shown in Fig. 4.14. The successive contours are in $5\,\mu$m steps with w going from $70\,\mu$m to $110\,\mu$m and g going from $10\,\mu$m to $70\,\mu$m. With the different impedance combinations that are possible, it is necessary to choose a combination that is matched to $50\,\Omega$ and provides 3-dB coupling to the coupled port. These lines are indicated on Fig. 4.14, and their crossing gives the starting values for the 3-D design. The 50-Ohm match line is calculated from the equation $Z_m = \sqrt{Z_0^e Z_0^o}$ and the 3-dB coupling line is calculated using

$$Z_0^e = Z_m \sqrt{\frac{1+C}{1-C}} \tag{4.4}$$

$$Z_0^o = Z_m \sqrt{\frac{1-C}{1+C}} \tag{4.5}$$

where C is the voltage coupling value. The 'O' on the graph indicates the value that is chosen after the 3-D modeling ($g = 26\,\mu$m and $w = 73\,\mu$m). This is quite close to what was predicted using 2-D methods, however slight differences exist because of the parasitics associated with the feeding into the coupled-line section.

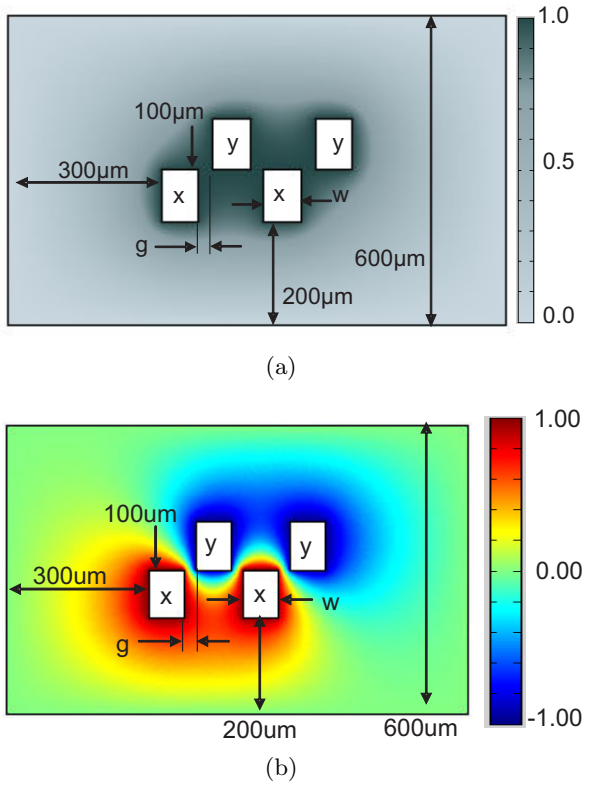

Figure 4.13: The dimensions of the coupling cross section. 'x' and 'y' indicate the two conductor pairs. Either these two conductor pairs are both (a) of the same potential (even-mode) or (b) of opposite potentials (odd-mode). The amplitude of the electric potential is overlaid on the graph.

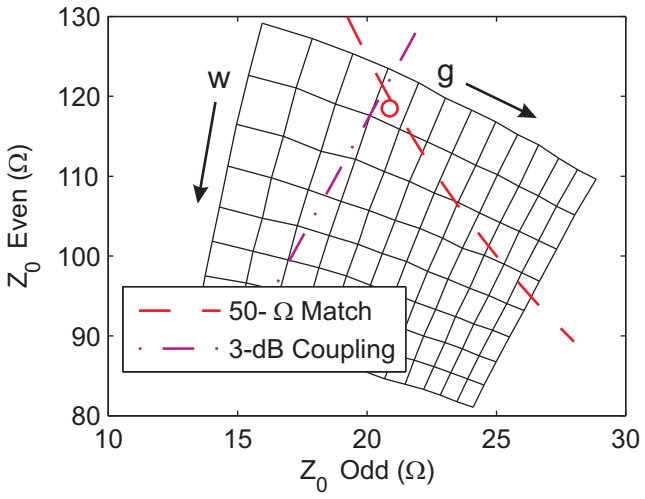

Figure 4.14: The even- and odd-mode characteristic impedances are shown for different values of w and g, as given in Fig. 4.13. By plotting the 3-dB coupling and 50-Ω match lines, the proper values of w and g are accessible graphically.

4.4.2 The 3-D Design and Results for the Lange Coupler

After the cross section has been calculated, the results are used to design the directional coupler. One must ensure that the electrical paths are as balanced as possible at the four ports, notwithstanding the asymmetries of the design. The full model is simulated using Ansoft HFSS^{TM} and any necessary adjustments are made to the design at this point. The electromagnetic effects of drain holes, used to remove the sacrificial photoresist from the structure, and periodic support straps for the center conductor are treated in the full-wave model. A photograph of the fabricated Lange coupler is shown in Fig. 4.15.

Fig. 4.16 shows the simulated values for the frequency response of the S parameters of the 3-dB coupler. The phase difference between the two output ports is measured to be $90° \pm 1.0°$ from 20 to 50 GHz, attesting to the broadband phase characteristics of a Lange-type coupler. The output magnitude difference is not as broadband, but this is partially due to a desire for a tighter output magnitude imbalance near the design frequency, 36 GHz. Four-port de-embedding will be useful for these measurements when they are taken.

4.4.3 Discussion of Lange Coupler

A 3-dB directional coupler derived from a Lange coupler has been designed and fabricated using a process that is completely compatible with that used to fabricate rectangular microcoax. This coupler does not suffer from the complications of imbalanced even and odd-mode phase velocities that have been common in the past with Lange couplers because of the homogeneously air-loaded coupled section of the lines. The multilayer configuration enables flexibility in the routing of the ports. Though the direct port is in the opposite corner of the coupler from the input port, as a 'traditional' Lange coupler, an 'unfolded' Lange port configuration is readily possible. A

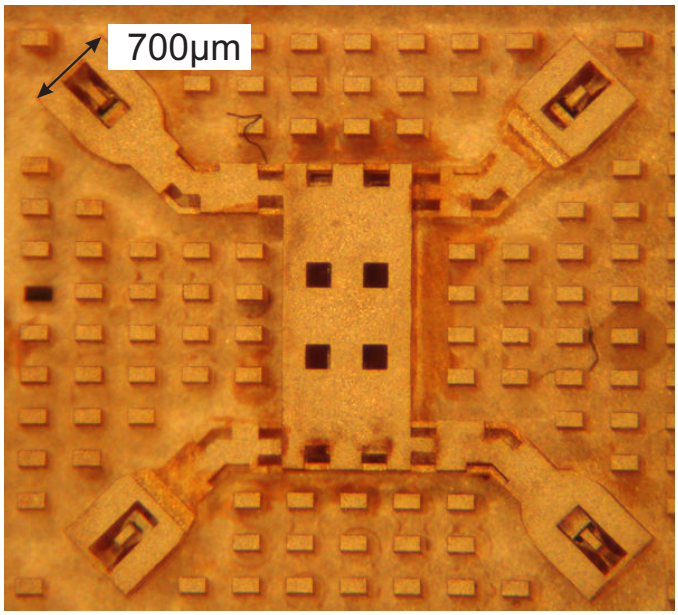

Figure 4.15: A Photograph of a fabricated Lange coupler.

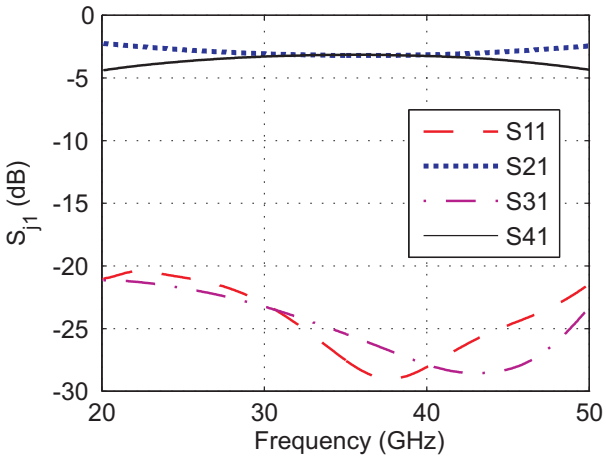

(a)

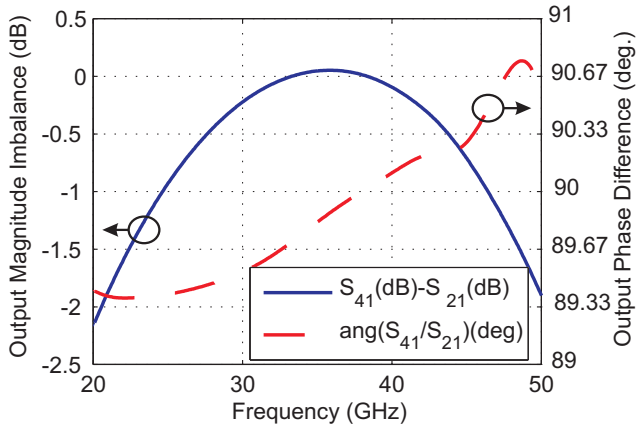

(b)

Figure 4.16: The simulated S-parameter data given port one being excited. (a) The values of the S parameters in dB for port 1 excited. (b) The difference in output magnitude and phase.

broad bandwidth for both the output phase and amplitude are demonstrated for this device, with the output phases deviating from ideal $\pm 1.0^\circ$ over the 20 to 50 GHz range. The output port amplitudes are 3.2 dB ± 0.2 dB from 30 to 42 GHz.

4.5 Coupled-Line Directional Couplers

One family of devices that has been designed and measured with good success is that of the directional coupler. The same methods as were used for the even- and odd-mode analysis for the Lange coupler in Section 4.4 is used here. Improvements in the design were made, including the addition of support straps for the inner conductors. These straps help fix the position of the inner conductor under probing conditions. An image of a directional coupler is shown in Figure 4.19.

Figure 4.17 provides the even- and odd-mode impedances for the coupled lines used to design the directional couplers, as was seen in Figure 4.14 for the Lange coupler. The dimensions of the cross section of the coupled lines are shown in Figure 4.17(a). w=105 μm, g=48 μm, and w_0=100 μm for the 10-dB directional coupler, and w=95 μm, g=120 μm, and w_0=50 μm for the 20-dB directional coupler.

The results for two directional couplers operating at 26 GHz are shown in Figure 4.19. A 10-dB coupler is shown in Figure 4.19(a) and a 20-dB coupler is shown in Figure 4.19(b). The couplers are designed using a pair of coupled transmission lines that are $\lambda/4$ at 26 GHz. The measurement is done with a series of measurements using a two-port network analyzer with an uncalibrated termination for a third port. The standing-wave pattern is clearly visible for the coupled ports in both plots. The same analysis that was used for the Lange coupler in Section 4.4 is used here. Results presented here show that the design method is correct, even though the implementation was flawed for the Lange Coupler.

In summary, this chapter shows excellent results for insertion loss, return loss, and

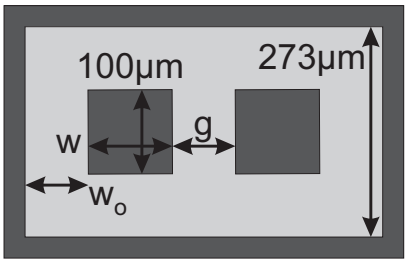

(a) Cross Section Sketch

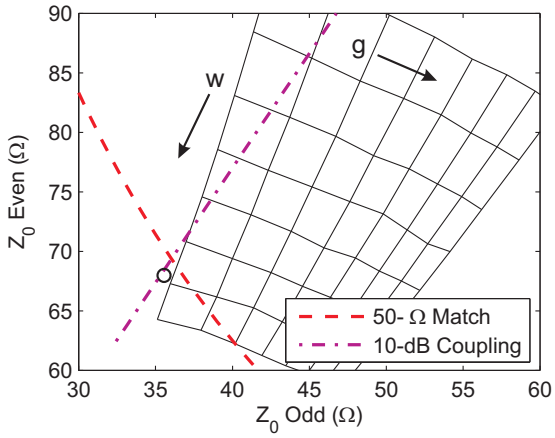

(b) 10-dB Coupler

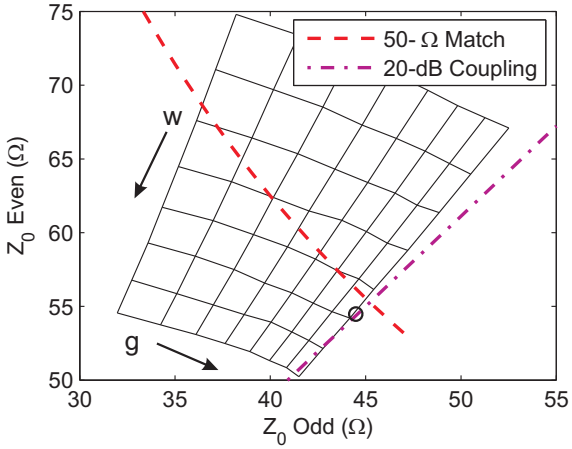

(c) 20-dB Coupler

Figure 4.17: The even- and odd-mode impedances are graphed for the directional couplers fabricated using coupled lines. (a) Sketch of the cross section of the transmission lines. (b) Each line going down represents an increase in w of 5 μm, with an starting value of 75 μm. Each line going from left to right represents a 10 μm increase in g, with a starting value of 50 μm. w_o is 100 μm for this case. (c) Each line going down represents an increase in w of 5 μm, with an starting value of 70 μm. Each line going from left to right represents a 10 μm increase in g, with a starting value of 50 μm. w_o is 50 μm for this case.

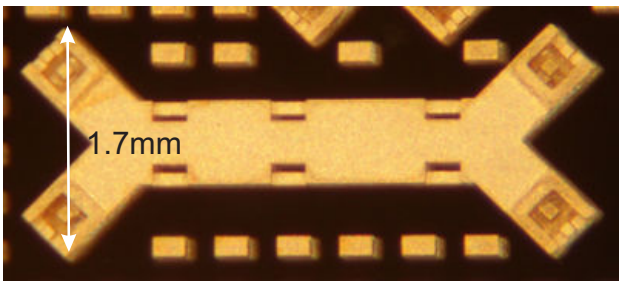

Figure 4.18: A photograph of a 26-GHz coupled-line directional coupler. The length is the same for the 10-dB and 20-dB couplers, and the width is 1.7 mm for one and 1.8 mm for the other, so the photograph would be vitually identical for the two. The performance of both couplers is shown in Figure 4.19.

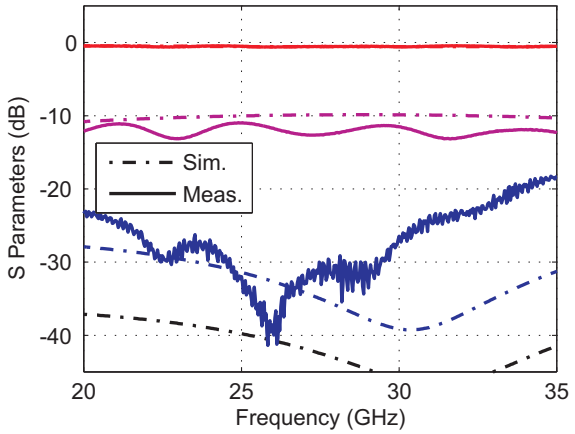

(a) 10-dB Coupler

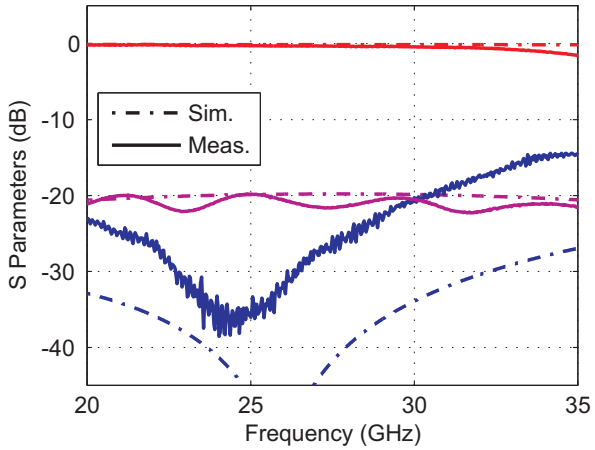

(b) 20-dB Coupler

Figure 4.19: The measured response for the directional couplers versus the simulated response for (a) 10-dB directional coupler and (b) 20-dB directional coupler.

amplitude and phase imbalance of a number of millimeter-wave hybrids. The hybrids were designed using the finite-element method including compensation of the reactances due to the T junctions. Implementation of the four-port de-embedding algorithm developed in Chapter 2 shows good agreement between measurement and simulation for several devices.

Chapter 5

SiPak™ Package – Silicon Optical Bench

5.1 Introduction

In the previous chapters, it was shown that finite element full-wave modeling can predict to a high degree of accuracy the performance of 3-D microcoaxial components. The resonators and couplers presented in Chapter 3 and Chapter 4 are narrow band devices, and use a limited number of materials, i.e. copper, polymer, air, and silicon (to a limited extent). It is of interest to apply similar analysis methods to heterogeneous 3-D circuits for broadband applications. An interesting and complex example is that of a 0-40 GHz microfabricated 3-D electro-optic transducer, shown in Figure 5.1.

In this package, two different types of metals are used (gold and copper), the silicon is not just a flat substrate, the connection to the rest of the system is done through a polymer-based flexible circuit, a high-dielectric-constant spherical lens is in close proximity to the circuitry, a resistive material is used for impedance matching, and active devices are hybridly integrated using epoxy and bond wires. The large number of different materials will dramatically complicate the complexity of the electromagnetic model.

In contrast to the microcoaxial circuits, which are effectively 2.5 dimensional, for which the substrate is flat, and for which most of the geometries are rectangular, in this case the shapes are more varied. As shown in Figure 5.1(a), the silicon substrate, with a relative dielectric constant of 11.9, and containing 3-D gold-plated pyramidal via

holes, is connected to the thin flexible substrate (ϵ_r=3.1) using solder bumps. On one side, the via hole is connected to a microstrip circuit on a 50-μm-thick substrate, and on the other side to a CPW circuit with integrated surface resistance and coupling to a laser diode. The aspect ratios in this component are very large. The largest dimension is over 25 mm, while the passivation layer on the flexible substrate is 18 μm thick.

The goal of the analysis is to gain an understanding of the performance of the entire component, as well as its parts, and to enable improved designs. Therefore, it is of interest to solve the challenging problem of accurately modeling this heterogeneous structure over a wide range of frequencies. For example, to accurately solve for the fields in Figure 5.1(a), 300,000 tetrahedrons are required, with a 6-hour run time on a dual-processor Intel Xeon workstation with 4 GB of RAM.

Telecommunications modules fabricated using the silicon optical bench (SiOB) concept provide excellent performance in a small form-factor package [87]. The ability to batch process the optical subassembly (OSA) through wafer-level processes eliminates much of the costly, serial labor required to produce traditional high-performance optoelectronic modules [88]. In addition, product reliability, assembly automation and yield are improved because of the precise feature definition achievable using photolithography. Historically, SiOB has been used as a component that is inserted into metal or ceramic hermetic packages. Initial work by Rohm and Haas Electronic Materials (RHEM) to convert the SiOB into a hermetic package by sealing a micromachined lid to the SiOB, along with initial environmental testing results, were previously reported in [89] and is being commercialized under the Si-Pak trademark. This approach allows hundreds to thousands of laser transmitters and receivers, complete with micro-optics and thin film electronics, to be fabricated, assembled, sealed, and tested at wafer or grid levels. This chapter focuses on the electromagnetic 3-D modeling, simulation, measurement, and layout optimization for next-generation hermetic silicon packages. The initial goal of 10 Gb/s Ethernet and SONET directly modulated laser (DML) trans-

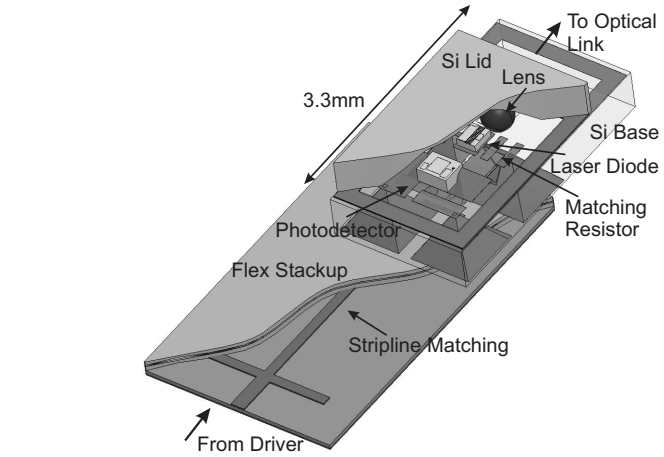

(a)

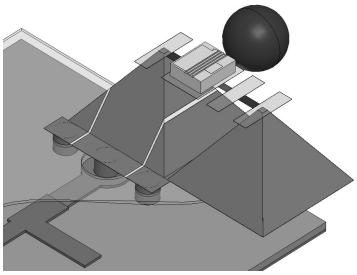

(b)

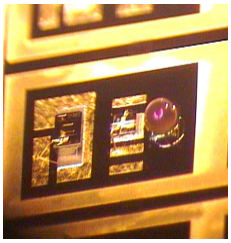

(c)

Figure 5.1: A sketch of the silicon package (a) with the pertinent features identified. For clarity, the lid and flex stack-up have been sliced open. (b) Detail of RF vias connecting from flex to SiOB, with patterning on one of the pyramidal vias. The photograph (c) shows a fully populated SiOB without a lid before wafer dicing. The spherical lens is 400 μm in diameter.

mitters is successfully demonstrated with simulations in good agreement. Avenues for design optimization to extend to 25 Gb/s or 40 Gb/s applications are also presented.

Impedance matching in high-bandwidth optoelectronic systems is important for reduced power consumption of the system and to maintain the signal integrity of the waveforms and transmitted optical signal [90]. The exact requirements are dependent on the targeted application (i.e. transmitter optical eye mask margin); however, a return loss better than 10 dB over the frequency range is typically considered adequate.

Here, the electromagnetic modeling developed for 10-Gb/s telecommunications transmit modules is presented. Figure 5.1 shows the major design components of interest

for the electromagnetic performance. The silicon base is processed on both the front and back sides. The silicon lid is processed on a separate wafer. The two wafers are bonded and diced, allowing for a highly parallelized and thus low-cost process. This gives module densities of 10 to 15 devices per cm^2 on the wafers prior to dicing. After dicing, the discrete silicon package is attached to a multi-layer flexible substrate (flex), providing an attachment to the laser driver IC. The full length of the flex is on the order of 2 cm. The silicon package, after being solder attached to the flex, would be incorporated into a mechanical package (not shown) and aligned to either a fiber or a fiber receptacle to achieve a transmitter optical subassembly (TOSA) for insertion into a transceiver.

The electro-optical design presented here utilizes a base silicon wafer which is locally thinned from one side for each die. The thinned regions are then further processed to create a series of microvias which can be provided on a 200 μm or less pitch. These vias are hermetically sealed with gold plugs. The wafer top side contains thin film circuits including a matching resistor, solder bond pads, and a precision micromachined region to contain a 400-μm lens. The periphery of each chip contains a bond ring for solder sealing a cavitated silicon lid. A wafer or grid of these bases are populated each with a InP laser die, a monitor photodetector and a lens, all of which are precision bonded, free of organic compounds, using thin film Au-Sn and other bonding methods. Once the wafer or grid is populated it undergoes a wedge bonding operation and then has a wafer or grid of optically coated silicon lids hermetically sealed onto the die under several atmosphere of helium. The lid is designed with a thinned membrane which serves as an absolute pressure gauge allowing the level of hermeticity to be determined above a threshold value by the bulge of the membrane region. These parts are then tested, diced into separate components, and attached to flex circuitry using BGA attachment. The parts are used to construct recepticalized or pigtailed assemblies for fiber optic transceiver applications such as 10 gigabit Ethernet. This approach allows significant

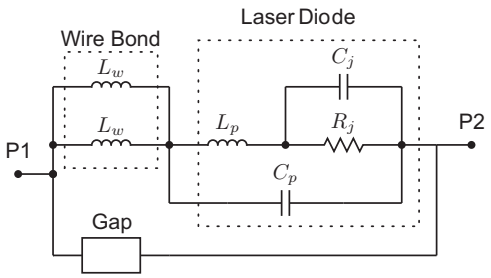

Figure 5.2: The circuit model for the measured laser diode is shown consisting of three parts: the S parameters of the gap, the inductances of the wire bonds, and the laser diode equivalent circuit. The computed element values are: R_j=5.9 Ω, C_j=1.2 pF, C_p=0.02 pF, L_p=0.45 nH, and L_w=0.68 nH.

cost reduction, increases thermal and RF performance, allows a very high degree of assembly automation with a simple tool set, significantly reduces part to part variation, and allows substantial size reduction over existing TO cans and hybrid packaging means.

5.2 Component Characterization

5.2.1 Laser Diode Characterization

The characterization of laser diodes using measurements to extract an equivalent circuit has been conducted by numerous researchers, e.g. [91–93]. The circuit model from [91], derived by linearizing the rate equations for a laser with a non-uniform lateral carrier distribution, is used successfully to model a laser diode in a 10-Gb/s system [92]. In [93], a butterfly-packaged, 2.5 Gb/s laser module is designed using a similar equivalent circuit extracted from measurement characterization of the laser diode. Using a similar technique, we characterize a 1.31-μm Fabry-Pérot directly modulated laser diode designed for 10 Gb/s performance available from Modulight, Inc. The laser diode is measured in series in a two-port configuration with Thru-Reflect-Line (TRL) calibration in 50-Ω microstrip. Measurements of the test circuit without the laser diode give parasitic values for the microstrip series gap that are included in the model. The resulting 2-port data is virtually terminated with a short at port 2 and fit as a 1-port

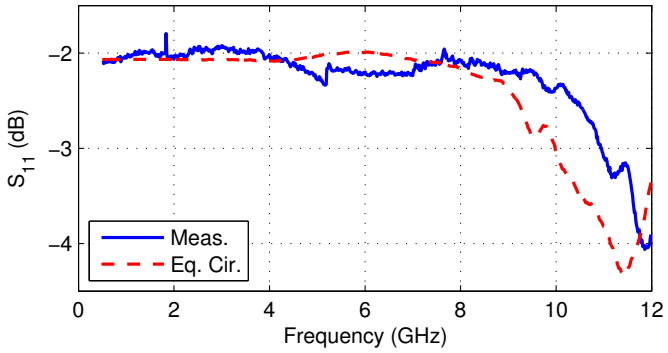

Figure 5.3: A comparison of the modeled results using the equivalent circuit for the diode compared to the measured results of the laser diode for a fixed bias point of 22 mA.

device to the circuit model for the diode shown in Figure 5.2. A comparison of the computed circuit model for a 22 mA bias current with the measurement results is shown in Figure 5.3.

5.2.2 Package Characterization

The silicon package is characterized using Ansoft HFSS. The package design allows for a hermetic seal of the laser and an optically transparent sidewall window with an anti-reflection coating for the 1.31 μm wavelength beam. Signal and monitor lines are routed into the package using hermetic metalized through vias. The initial design, shown in Figure 5.1, uses a patterning scheme on the via sidewalls and stripline circuit on the flex substrate for matching. Figure 5.1 highlights several of the key challenges of this design. The relative permittivity of the silicon is 11.9, compared to 1.0 for air and 3.5 for the polyamide used for the flex substrate; this wide range of relative permittivity can cause modeling difficulties because of the corresponding range of effective wavelength. In addition, the relative dimensions can cause meshing difficulties: the passivation layer on flex is 18μm thick, which increases the mesh count; and small metallic features exist on the SiOB in areas that cannot be neglected. These factors, when taken together, create computationally intensive models.

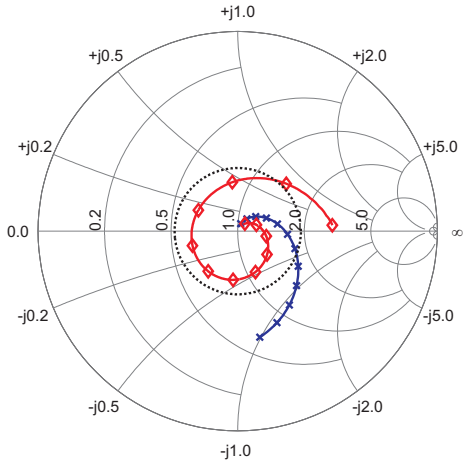

Figure 5.4: A comparison of the simulated input match before ('x') and after ('◊') the addition of the impedance matching circuit on the flex substrate. The data are plotted on a 25-Ω Smith Chart with markers at each GHz increment. The 10-dB return loss circle is given.

The SiOB is connected to the driver IC with a 2-cm long piece of flexible substrate. This provides stress relief for the connections and room for impedance matching the diode/package combination. The flex substrate is a polyamide, having ϵ_r=3.1-3.5 and $\tan\delta$=0.01-0.04 over the frequency range of interest.

A dual-stub matching circuit is designed on flex to increase the bandwidth of the system. The impedance match of the system with and without the stub-matching compensation on the flex substrate is shown in Figure 5.4 on a 25-Ω Smith Chart. The 10-dB return loss circle is given on the graph to highlight the improvement gained with the matching circuit, pushing the 10-dB crossing point from 7.3 GHz to 10.8 GHz.

5.2.3 Design Improvements

Three challenges arise from the via configuration for the design described above: the patterning within the vias as shown in Figure 5.1(b) adversely affects yield; the via depth is such that parasitic reactances limit performance at high frequencies; and layout or routing of the interconnection is constrained. We investigate an alternate

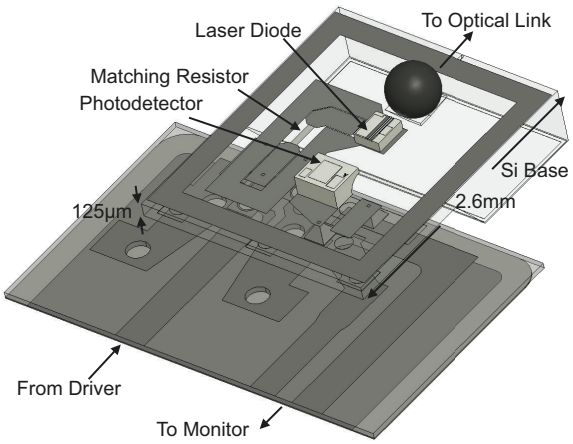

Figure 5.5: An annotated sketch of the MV design. For clarity, the Si lid and top passivation layer of the flex substrate have been removed.

micro-via (MV) design, shown in Figure 5.5 The MV design eliminates the patterning within the via (improving yield & high-frequency performance) and eliminates the need for flex stripline matching. This is accomplished by selectively thinning the Si substrate to shorten the vias while preserving mechanical support.

5.3 System Measurement

Broadband measurements are performed with a Wiltron VNA calibrated with external SOLT standards. A microwave probe with a resistive impedance transformer is used to match the 50-Ω ports of the VNA to the 25-Ω electro-optic driver over a broad bandwidth. The simulated and measured reflection coefficient for the 10-GHz design is shown in Figure 5.6.

The measured and simulated S_{11} response (to 30 GHz) for the MV package is shown in Figure 5.7. This does not include the flex circuit. Disagreement between experimental and simulation results above 25 GHz is due to interface differences between the calibration substrate and the SiOB. Subsequent wafers will have integrated calibration standards and more readily accessible test points for 2-port scattering parameter measurements.

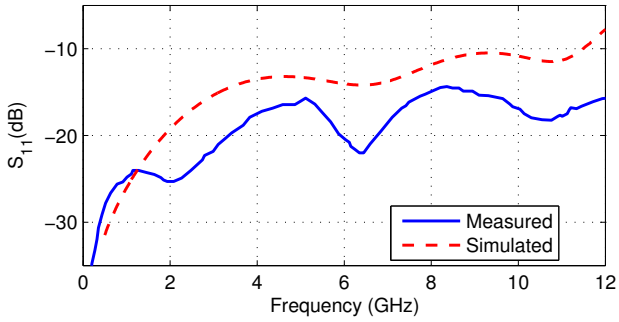

Figure 5.6: The frequency response of the system (initial design) showing a comparison of the simulation and measured data. The data are plotted normalized to a 25-Ω reference impedance.

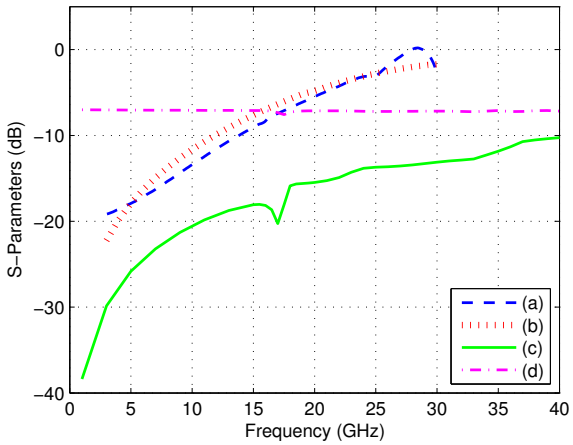

Figure 5.7: The frequency response of the system utilizing the MV design, showing a comparison of measured (a) and simulation (b) data. The simulated frequency response of the broadband MV package showing better than 10 dB insertion loss (c), S_{11}, up to 40 GHz, and practically flat transmission (d), S_{21}. These values are close to the theoretical limit near -7 dB due to the series 20-Ω matching resistor. All data are plotted normalized to a 25 Ω port impedance, except port 2 of the broadband design which is normalized to 5 Ω.

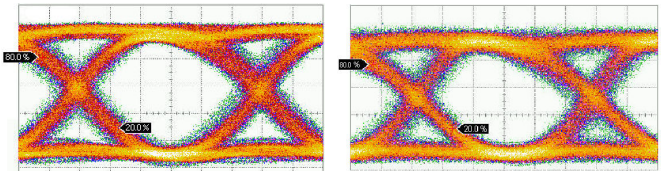

(a) (b)

Figure 5.8: The eye diagrams for a 10 Gb/s data stream through the package for a 4 dB extinction ratio (a) using the initial design and (b) using the MV design. The horizontal scale on the plots is 16 ps/div.

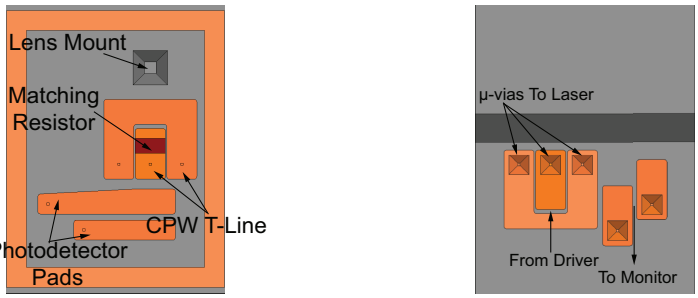

(a) (b)

Figure 5.9: A sketch of the broadband MV package: from above (a), showing the coplanar transmission line (CPW T-Line), and placement of other pertinent features; and from below (b), illustrating how the optimizations simplify the flex substrate designer's task.

In addition to the RF characterization of the system, functional electro-optic testing is conducted on these laser packages. Transmitter optical eye patterns for the system are measured using an Agilent 86100A digital communications analyzer with a 20 GHz optical input O/E converter. The resulting measurements are shown in Figure 5.8 for a 10-Gb/s stream of data with a bias current to the laser diode of 45 mA. Measured extinction ratios of both 4 dB are studied for both the initial and MV designs, corresponding respectively to the performance necessary for Ethernet applications.

5.4 Extensions to High-Data-Rate Designs

We have presented measured data for two different designs for 10 Gb/s systems. The modules are fabricated using a parallelized, low-cost approach that provides the requisite system performance. The predictive ability of the modeling techniques have been validated by comparison of the simulated and modeled S_{11} for two design topologies. System-level verification on functional 10 Gb/s optical transmitters provides additional validation of the design process. We have shown that design for performance optimization is possible using the EM simulation tools. By improving the EM performance of the signal lines into the OSA, while maintaining the hermeticity of the packaging, data

rates of 25 Gb/s, and potentially data rates of 40 Gb/s, are achievable.

The main areas in which investigation is ongoing to achieve these goals are the following.

(1) The development of a straight-through layout of the top-side coplanar waveguide structure.

(2) The use of different materials for the matching resistor in order to attain more desirable physical dimensions. The current surface resistivity of the thin-film resistors is approximately 5 $\Omega/\square$, which is too low for the resistors to behave as lumped elements in 40-Gb/s systems.

(3) Movement of the resistor closer to the laser [90].

(4) Optimization of the flex circuit and SiOB interface.

Figure 5.7 provides some preliminary simulation results on the new design, illustrated in Figure 5.9, indicating that a S_{11} return loss better than 10 dB, and a flat S_{21} response to 40 GHz are feasible. The measurements from Figure 5.7 give us confidence that the design improvements will yield better performance. This will be tested in the near future.

Chapter 6

Discussion and Future Work

The design, analysis and measurement characterization of millimeter wave devices fabricated using the Polystrata^{TM} process are presented in Chapters 2, 3, and 4. The modeling techniques are demonstrated to work well for the RF aspect of an optoelectronic transmitter in Chapter 5. The highlights are described in Section 6.1 and future directions are outlined in Section 6.2.

6.1 Summary and Conclusions

The use of air-filled copper microfabricated recta-coax is motivated in Chapter 1. This is argued from the standpoint of transmission loss, design flexibility, cable-to-cable isolation, and dispersion. An explanation of the fabrication process is given and an attempt to contextualize the work is made.

Chapter 2 describes a new technique for calibrating four-port devices. The ability to measure the performance of the branch-line couplers is compromised by the difference in parasitic reactances at the probe tip between the off-wafer calibration substrate (high ϵ_r) and the air-filled coax probe structures. By considering the connection of the probes at each port to be a repeatable error box, as is common with the TRL calibration in two-port measurement situations, it is possible to de-embed the transition into the rectacoax from the measurement. Measurement data supporting this for branch- line couplers operating at 36 GHz is provided.

The resonators described in Chapter 3 attest to the design flexibility available with the fabrication process. Figure 3.4 presents the measured performance of microfabricated resonators described in the literature. A method for comparing the quality factor for different frequencies and different cavity heights is derived and $R1$ is shown to have the best performance for Q. A cavity resonator, with a designed operating frequency of 36 GHz, has a measured quality factor better than 1000. Detailed studies of the loss mechanisms of several half-wave cavity resonators are presented. Miniaturization factors of 15 % and 71 % on the footprint of the resonators are demonstrated for operating frequencies of 26 and 36 GHz. Physics-based circuit models of the miniaturized resonators are derived for ready optimization in filter designs.

Several 90° hybrids are analyzed and shown in Chapter 4. With the de-embedding methods of Chapter 2, excellent performance is seen. The first compensated T-junction for microfabricated rectangular coax is demonstrated. A new, Lange-like 3-dB directional coupler is designed and fabricated. A detailed modleing approach combining analytical SCCM and 2- and 3-D numerical FEM is developed.

In Chapter 5 the electromagnetic design of the SiPak$^{\text{TM}}$ optoelectronic transmitter is described. With the current design, measured performance for 10 Gb/s data rates is achieved. Designs to provide 25 Gb/s and 40 Gb/s performance are also detailed. Impedance matching on a flexible substrate is one avenue pursued for performance gains and then the re-arrangement of transmission lines and components within the SiPak$^{\text{TM}}$ package provide the remaining performance gains.

Other new designs are presented in Section 6.2, among them a collinear coaxial antenna, cavity filters, and a rat-race coupler. The initial work towards demonstrating these devices has been done, however more remains to be done here. More generally, the framework for a design procedure for 3-D millimeter-wave components has been developed. This method is extensively shown for μcoaxial-based components, and then further validated with the work in Chapter 5.

6.2 Future Work

There are many aspects of this technology that remain to be explored in the future. A few points from each chapter are described and then some general comments are made. Some of the work described here is already underway.

6.2.1 Improved Component Design

The microfabricated resonators of Chapter 3 have excellent Q factors. As the release holes are made larger with the change from the 200 μm by 200 μm holes in $R1$-$R5$ to 400 μm by 400 μm holes in $R6$ and $R7$; this contributes to increased losses. The placement and shape of the release holes can be optimized and the Q-factor performance may increase by a few percent.

The Lange couplers in Chapter 4 did not perform as expected. The Lange couplers should be redesigned so that they have periodic supports for both center conductors, since this is the most likely cause of degraded performance. The addition of these supports should not have an appreciable effect on the even- and odd-mode velocity of propagation because of the relatively small volume these supports occupy relative to the total device size.

In the multi-layer structures, there are many open questions that are left related to layer-to-layer interconnects, such as z-turns, as well as the optimal layout when multiple components are stacked. This leads into the question of density of 3-D circuits, which is still an open research problem.

The loss in the components demonstrated to date can mostly be attributed to the skin effect. Therefore, coating of the transmission lines with silver can lead to reduced losses, while coating with an inert metal such as gold could simplify design and fabrication. The dielectric used for the straps is shown to significantly contribute to the loss and most likely will be the bottleneck for power handling. Therefore, investigating

other dielectric or metal supports for higher power levels is an open question. As the frequency increases, all the losses become more pronounced, but other effects also come into play. For example, surface inductance cannot be neglected, and surface roughness will become a more important contributor to loss. There has been only a limited amount of work investigating loss due to two-dimensional, random roughness, and for higher millimeter-wave frequencies, this should be a topic of future research.

6.2.2 Improved Characterization

In Chapter 2, the measurement techniques that allow TRL-type characterization of a four-port device is shown to provide excellent results. These techniques are readily extendible to multi-port devices with more ports if all the remaining ports can be terminated. The question remains whether it would be possible to get the data for a six-port device using a two-port network analyzer with only two more terminations and the other ports left open. This would allow characterization of networks with more than four-ports.

An important characterization that has not yet been performed is power handling capability of these small structures filled with a low breakdown voltage dielectric (air and polymer straps). This measurement will require the design of new components and careful calibration. Two possible factors will limit the power handling: heating due to Joule losses and sparking caused by the dielectric breakdown or air ionization. Due to the sharp corners in the fabricated structures, it is not clear whether the thermal losses or dielectric breakdown will be the dominant limiting factor for the power handling.

6.2.3 Some Other Possible Components

Filters were not initially included in the scope of this work, but they are an obvious extension of the work in Chapter 3. A proof-of-concept simulation of a two-pole cavity filter, which is a direct extension from Chapter 3 is shown in Figure 6.1.

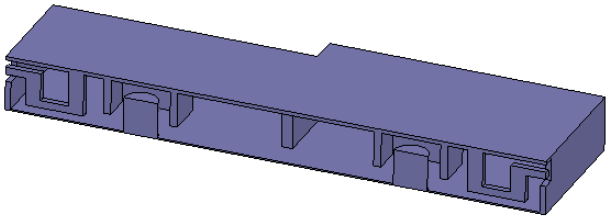

Figure 6.1: A sketch of a two-pole filter using coupled miniaturized cavity resonators.

Although bandpass filter characteristics are seen in this analysis, a practical filter would require an increased effort compared to what is required for this design. The fabrication of several proof-of-concept filter prototypes is expected to be finished in May of 2007. A detailed analysis of the advantages and limitations of this technology for filter design has not been performed, although it would be beneficial.

Although this technology is obviously advantageous for high frequencies, there is merit in looking into scaling to lower frequencies. The extremely good isolation between neighboring rectacoax makes it possible to implement devices with tight bend radii, thus reducing the footprint of the component. Of course, when designing miniaturized footprint components, the reactances due to bends must be carefully modeled. An illustration of scaling to lower frequencies is shown in Figure 6.2. We see that depending on the cross section at lower frequencies meandering can be employed; however, at higher frequencies this advantage decreases and then disappears. At 6 GHz there is significant reduction in size compared to devices that have not been meandered. The footprint of the device in Figure 6.2(a) is 86% smaller than an air-loaded one without meandering. The footprint of the 26-GHz meandered BLC is 30% smaller than without meandering. At 36 GHz the aspect ratio of the cross section is such that it does not make sense to meander the transmission lines.

A necessary component for many circuits is a Wilkinson power divider/combiner, which have improved isolation and bandwidth over the hybrids described in Chapter 4.

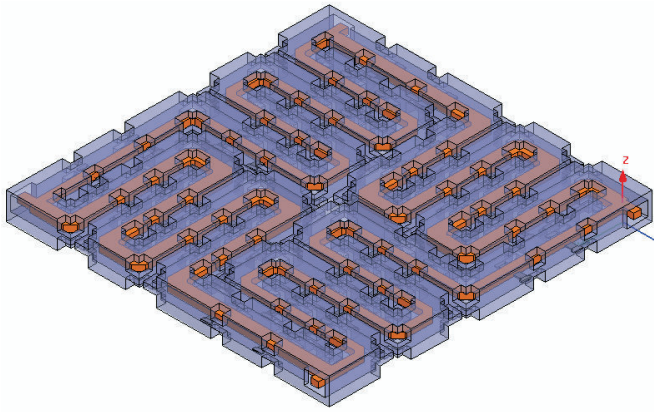

(a)

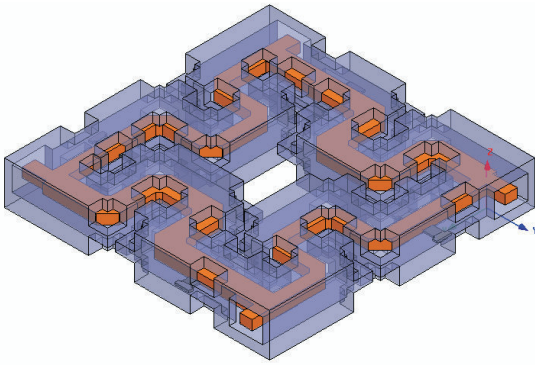

(b)

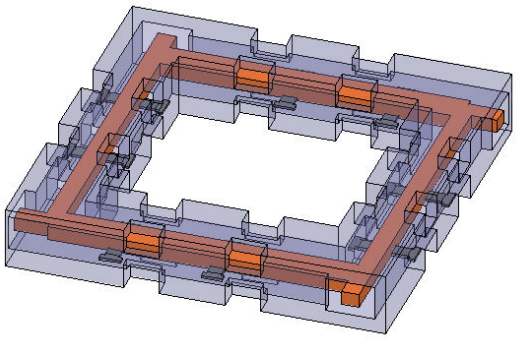

(c)

Figure 6.2: (a) A conceptual sketch of a 6-GHz branch-line coupler using meandering. (b) A sketch of a 26-GHz branch-line coupler using meandering. (c) A sketch of a 36-GHz coupler showing the meandering is no longer useful.

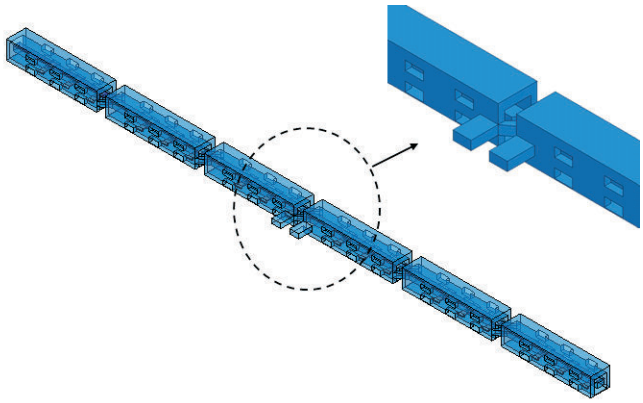

Figure 6.3: A conceptual sketch of a Collinear Coaxial Antenna.

In order for this component to be possible, a compatible resistive process must be developed. The resistive process must enable a value of 100 Ω for a lumped-element component in the millimeter-wave range. Such dividers/combiners would become an important component for broadband power combining and corporate feed networks.

Although an air-patch antenna compatible with the PolyStrata^{TM}process has been developed [36], there are other antenna designs that would be amenable to this microfabrication technology. An intriguing example is the coaxial collinear antenna shown in Figure 6.3, [94]. This antenna is often used at frequencies in the UHF band and below. With this antenna, a single feed is used for a linear array. The generator voltage is propagated along the transmission-line antenna by a guided-wave mode. After every half wavelength, the inner and outer conductor are interchanged, introducing a 180° phase shift. Thus, the generator voltage appears in phase at each element of the collinear array, and can be designed to provide current tapering for reduction of the side lobe levels. When the inner and outer conductors are interchanged, an unbalance is produced in the currents of the coaxial cable. This unbalanced current flows on the outer conductor and the antenna radiates like an array of wire antennas. The high-frequency limitations for such an antenna array are the parasitic reactances associated with the connection between collinear elements. With micro-coaxial cables, these reactances can

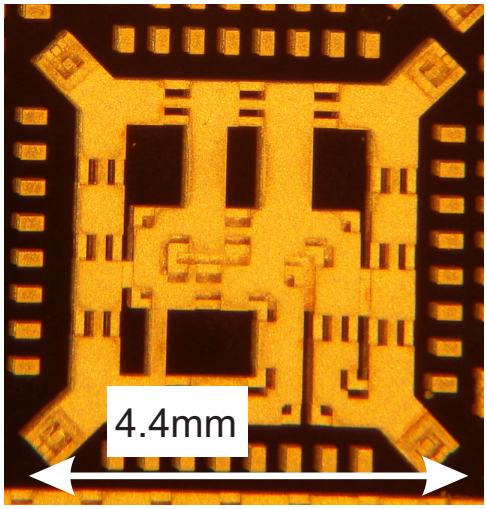

Figure 6.4: A photograph of a rat-race coupler designed for operation at 26 GHz.

be minimized and controlled.

Coaxial balun impedance transformers, often used by radio amateurs at frequencies below 1 GHz, are worth examining. Although very broadband, and flexible in design, these baluns have not been scaled to higher frequencies because their performance is sensitive to reactances due to the connection of the cables. Such baluns are useful in impedance matching networks, combiner/divider networks, and double-balanced and more advanced mixer architectures. The ability to minimize and control these reactances makes micro-coaxial cables an interesting technology for the fabrication of high-frequency baluns.

A rat-race coupler has been designed for operation at 26 GHz, Figure 6.4. This coupler has not yet been measured, but to the best of the author's knowledge, a rectangular coaxial rat-race coupler has not yet been demonstrated. Meandering of the transmission line, similar to what is shown in Figure 6.2 is employed to reduce the size of the device.

6.2.4 Integration

In Chapter 2, the connection from a PolyStrata$^{\mathrm{TM}}$cable to a measurement probe is described in detail. Although this was extremely useful for initial characterization, and was the easiest connection to fabricate, it is difficult to imagine integration with non-coaxial components and active circuits using this method. It follows that it is necessary to design connections to CPW and microstrip. RHEM has shown that these structures can be released from the substrate. Reliable connections to these transmission lines are important and should be examined in detail. Making this possible for a variety substrate with varied relative permittivities is important.

For any practical microwave system, integration with active circuits is required. This topic has barely been addressed at all, and there is much room for new research. There are some possible advantages of this technology when integrating actives, including good heat sinking due to a lot of metal and good thermal conductivity. Bias lines in this technology also need to be investigated.

6.2.5 Si-Pak^{TM} Package

Although the initial simulations for the 25- and 40-Gb/s work in Chapter 5 is encouraging, a final design is not done and measured data has not yet been acquired. It will be important to see how well the modeling can predict the RF behavior at the higher frequencies. There may be some amount of work to iterate upon these designs to meet all of the performance requirements.

A few other areas of future work are also necessary for the further integration of this technology into other systems. The issue of the reliability of these components has largely been untouched. The power handling has not been adequately characterized. Measurements are planned for the near future, however time ran out to include this work here. We assume that larger power levels will be required for many meaningful

applications that is possible using the current transmission-line topologies. Designs will be necessary which trade additional loss or mismatch for the ability to handle greater power levels. The tolerance to vibrations, temperature, and other environmental stresses remains to be see.

The electrical performance possible using this technology is better than that of the other transmission line technologies for a given size, loss, and isolation constraint. Although the remaining challenges regarding the practicality of this technology are important, high-quality transmission lines and components are readily designed and their behavior predicted using the techniques outlined here. Additionally, actuation akin to that seen in MEMS devices is potentially useful to this technology.

We believe that the results of this thesis show that this 3-D microcoaxial circuit technology opens up abilities for improved quality of existing passive components, enabling of entirely new components, as well as entire heterogeneously integrated microwave and millimeter-wave front ends.

Bibliography

[1] M. Lukić, S. Rondineau, Z. Popović, and D. Filipović, "Modeling of realistic rectangular μ-coaxial lines," IEEE Trans. Microwave Theory Tech., vol. 54, no. 5, pp. 2068–2076, May 2006.

[2] I. Jeong, S.-H. Shin, J.-H. Go, J.-S. Lee, and C.-M. Nam, "High-performance air-gap transmission lines and inductors for millimeter-wave applications," IEEE Trans. Microwave Theory Tech., vol. 50, no. 12, pp. 2850–2855, Dec. 2002.

[3] J.-B. Yoon, B.-I. Kim, Y.-S. Choi, and E. Yoon, "3-D construction of monolithic passive components for RF and microwave ICs using thick-metal surface micromachining technology," IEEE Trans. Microwave Theory Tech., vol. 51, no. 1, pp. 279–288, Jan. 2003.

[4] R. Chen, E. Brown, and C. Bang, "A compact low-loss Ka-band filter using 3-dimensional micromachined integrated coax," in 2004 Proc. Of IEEE Int. Conf. on MEMS, Maastricht, The Netherlands, Jan. 2004, pp. 801–804.

[5] I. Llamas-Garro, M. Lancaster, and P. Hall, "Air-filled square coaxial transmission line and its use in microwave filters," IEE Proc.-Microw. Antennas Propag., vol. 152, no. 03, pp. 155–159, June 2005.

[6] S. P. Natarajan, T. M. Weller, and A. M. Hoff, "Integrated micro coaxial air-lines with perforations," in 2006 Proc. Of IEEE MTT-S Int. Microwave Simp. Dig., San Francisco, CA, U.S.A., June 2006, pp. 424–427.

[7] S. Xu and P. Zhou, "FDTD analysis for satellite BFN consisting of rectangular coaxial lines," in Proc. Asia-Pacific Microwave Conf., Hong Kong, Dec. 1997, pp. 877–880.

[8] H. Oh-Hashi, H. Yukawa, and M. Miyazaki, "A compact Ku-band power combining network using rectangular coaxial line technology," in 1997 Proc. IEEE MTT-S Int. Microw. Symp. Dig., Denver, CO, U.S.A., June 1997, pp. 409–412.

[9] A. Cohen, G. Zhang, F.-G. Tseng, U. Frodis, F. Mansfeld, and P. Will, "EFAB: rapid, low-cost desktop micromachining of high aspect ratio true 3-d MEMS," in 1999 Proc. IEEE MTT-S Int. Mirco Electro Mechanical Systems, Orlando, FL, U.S.A., Jan. 1999, pp. 244–251.

[10] R.Chen, "Micro-fabrication techniques," Wireless Design and Development, pp. 16–20, Dec. 2004.

[11] J. Reid and R. Webster, "A 60 GHz branch line coupler fabricated using integrated rectangular coaxial lines," in 2004 Proc. IEEE MTT-S Int. Microwave Symp. Dig., June 2004, pp. 441–444.

[12] ——, "A compact integrated V-band bandpass filter," in 2004 Proc. Of IEEE AP-S Int. Symp., Monterey, CA, U.S.A., July 2004, pp. 990–993.

[13] R. T. Chen and E. R.Brown, "An ultra-compact low loss 30-GHz micromachined coaxial filter," in Proc. 35th European Microwave Conf., Paris, France, Oct. 2005.

[14] J. Reid, E. D. Marsh, and R. T. Webster, "Micromachined rectangular coaxial transmission lines," IEEE Trans. Microwave Theory Tech., vol. 54, no. 08, pp. 3433–3442, Aug. 2006.

[15] J. R. Reid and R. T. Webster, "A 55-GHz bandpass filter realized with integrated tem transmission lines," in 2006 Proc. of IEEE MTT-S Int. Microwave Simp. Dig., San Francisco, CA, U.S.A., June 2006, pp. 132–135.

[16] ——, "A 6-port 60 GHz coupler for an RN^2 beam former," in Proc. 2006 IEEE Antennas Propag. Soc. Int. Symp., Albuquerque, NM, U.S.A., July 2006, pp. 1985–1988.

[17] E. D. Marsh, J. R. Reid, and V. S. Vasilyev, "Gold-plated micromachined millimeter-wave resonators based on rectangular coaxial transmission lines," IEEE Trans. Microwave Theory Tech., vol. 55, no. 01, pp. 78–84, Jan. 2007.

[18] T. H. Lee, Planar Microwave Engineering: A Practical Guide to Theory, Measurement, and Circuits. Cambridge, UK: Cambridge University Press, 2004.

[19] ——, The Design of CMOS radio-frequency integrated circuits, 2nd ed. Cambridge, UK: Cambridge University Press, 2004.

[20] J. Hubert, J. Schoenberg, and Z. B. Popovic, "High-power hybrid quasi-optical Ka-band amplifier design," in 1995 Proc. of IEEE MTT-S Int. Microwave Simp. Dig., Orlando, FL, U.S.A., May 1995, pp. 585–588.

[21] K. Matsunaga, I. Miura, and N. Iwata, "A CW 4 watt Ka-band power amplifier utilizing mmic multi-chip technology," in IEEE GaAs IC Symposium Tech., Monterey, CA, U.S.A., Oct. 1999, pp. 153–156.

[22] H. T. Kim, W. Choi, and Y. Kwon, "V-band MMIC oscillator array," Electron. Lett., vol. 41, no. 08, pp. 481–483, Apr. 2005.

[23] D. L. Ingram, Y. C. Chen, I. Stones, D. Yamauchi, B. Brunner, P. Huang, M. Biedenbender, J. Ellion, R. Lai, D. C. Streit, K. F. Lau, and H. C. Yen, "Compact W-band solid state MMIC high power sources," in 2000 Proc. of IEEE MTT-S Int. Microwave Simp. Dig., Boston, MA, U.S.A., June 2000, pp. 955–958.

[24] J. B. Hacker, J. Bergman, G. Nagy, G. Sullivan, C. Kadow, H. K. Lin, A. C. Gossard, M. Rodwell, and B. Brar, "An ultra-low power InAs/AlSb HEMT W-band low-noise amplifier," in 2005 Proc. of IEEE MTT-S Int. Microwave Simp. Dig., Long Beach, CA, U.S.A., June 2005, pp. 1029–1032.

[25] M. W. Chapman and S. Raman, "A 60-GHz uniplanar MMIC 4× subharmonic mixer," IEEE Trans. Microwave Theory Tech., vol. 50, no. 11, pp. 2580–2588, Nov. 2002.

[26] T. Hirose, K. Makiyama, K. Ono, T. M. Shimura, S. Aoki, Y. Ohashi, S. Yokokawa, and Y. Watanabe, "A flip-chip MMIC design with coplanar waveguide transmission line in the W-band," IEEE Trans. Microwave Theory Tech., vol. 46, no. 12, pp. 2276–2282, Dec. 1998.

[27] F. T. Ulaby, Fundamentals of Applied Electromagnetics. Upper Saddle River, NJ, U.S.A.: Prentice Hall, 2001, pp. 40–49.

[28] D. Sherrer and J. Fisher, "Coaxial waveguide microstructures and the method of formation thereof," U.S. Patent 7 012 489, Mar. 14, 2006.

[29] K. J. Vanhille, D. L. Fontaine, C. Nichols, Z. Popović, and D. S. Filipović, "Ka-band miniaturized quasi-planar high-q resonators," in press, IEEE Trans. Microwave Theory Tech., June 2007.

[30] K. Vanhille, D. Filipović, C. Nichols, D. Fontaine, W. Wilkins, E. Daniel, and Z. Popović, "Balanced low-loss Ka-band μ-coaxial hybrids," in 2007 Proc. IEEE MTT-S Int. Microwave Symp. Dig., Honolulu, HI, U.S.A., June 2007.

[31] K. J. Vanhille, D. L. Fontaine, C. Nichols, D. S. Filipović, and Z. Popović, "Quasi-planar high-Q millimeter-wave resonators," IEEE Trans. Microwave Theory Tech., vol. 54, no. 6, pp. 2439–2446, June 2006.

[32] D. S. Filipović, Z. Popović, K. Vanhille, M. Lukić, S. Rondineau, M. Buck, G. Potvin, D. Fontaine, C. Nichols, D. Sherrer, S. Zhou, W. Houck, D. Fleming, E. Daniel, W. Wilkins, V. Sokolov, and J. Evans, "Modeling, design, fabrication, and performance of rectangular μ-coaxial lines and components," in 2006 Proc. IEEE MTT-S Int. Microwave Symp. Dig., San Francisco, CA, U.S.A., June 2006, pp. 1393–1396.

[33] M. Lukic and D. S. Filipovic, "Modeling of surface roughness effects on the performance of rectangular μ-coaxial lines," in ACES Conference, Miami, FL, U.S.A., Mar. 2006.

[34] M. V. Lukic and D. S. Filipovic, "Modeling of 3-d surface roughness effects with application to μ-coaxial lines," IEEE Trans. Microwave Theory Tech., vol. 55, no. 3, pp. 518–525, Mar. 2007.

[35] K. J. Vanhille, D. L. Fontaine, C. Nichols, D. S. Filipović, and Z. Popović, "A capacitively-loaded quasi-planar Ka-band resonator," in Proc. 36th European Microwave Conf., Manchester, U.K., Sept. 2006, pp. 495–497.

[36] M. Lukic, D. Fontaine, C. Nichols, and D. Filipovic, "Surface-micromachined Ka-band phased-array antenna," in Antenna Applications Symposium, Monticello, IL, U.S.A., Sept. 2006.

[37] M. V. Lukic and D. S. Filipovic, "Integrated cavity-backed Ka-band phased array antenna," in IEEE AP-S International Symposium, Honolulu, HI, U.S.A, June 2007.

[38] T. A. Driscoll, "Algorithm 756: A matlab tool box for schwarz-christoffel mapping," AMC Trans. Math. Softw., vol. 22, no. 2, pp. 168–186, 1996.

[39] S. Ramo, J. Whinnery, and T. V. Duzer, Fields and Waves in Communication Electronics, 2nd ed. New York, U.S.A.: John Wiley and Sons, Inc., 1998, pp. 2,558–567.

[40] H. A. Wheeler, "Formulas for the skin effect," Proc. IRE, vol. 30, no. 9, pp. 412–424, Sept. 1942.

[41] F. Alessandri, P. Capece, and R. Sorrentino, "Theory and experiment of rectangular coaxial line discontinuities and junctions," in 1990 Proc. IEEE MTT-S Int. Microwave Symp. Dig., vol. 1, Dallas, TX, U.S.A., May 1990, pp. 259–261.

[42] S. Xu, X. Wu, W. Guo, and Z. Li, "Scattering characteristics of rectangular coaxial line branching directional couplers," IEEE Microwave Guided Wave Lett., vol. 3, pp. 6–8, Jan. 1993.

[43] ——, "Scattering characteristics of rectangular coaxial line discontinuities," IEE Proc. Microw. Antennas Propag., vol. 142, pp. 257–264, June 1995.

[44] J. Jin, The finite element method in electromagnetics, 2nd ed. New York, NY, U.S.A.: John Wiley and Sons, Inc., 2002, pp. 19–43.

[45] B. Notaros, B. D. Popovic, J. P. Weem, R. A. Brown, and Z. Popovic, "Efficient large-domain MoM solutions to electrically large practical EM problems," IEEE Trans. Microwave Theory Tech., pp. 151–159, Jan. 2001.

[46] J. L. Volakis, A. Chatterjee, and L. C. Kempel, Finite Element Method for Electromagnetics. New York, NY, U.S.A.: John Wiley and Sons, Inc., 1998.

[47] M. N. O. Sadiku, Numerical Techniques in Electromagnetics, 2nd ed. Boca Raton, FL, U.S.A.: CRC Press, 2001.

[48] G. Carchon, W. De Raedt, and B. Nauwelaers, "Accurate transmission line characterization on high and low-resistivity substrates," in 2001 Proc. IEEE MTT-S Int. Microwave Symp. Dig., Phoenix, AZ, U.S.A., June 2001, pp. 1539–1542.

[49] G. Carchon, W. De Raedt, and E. Beyne, "Compensating differences between measurement and calibration wafer in probe-tip calibraitons," in 2002 Proc. IEEE MTT-S Int. Microwave Symp. Dig., Seattle, WA, U.S.A., June 2002, pp. 1837–1840.

[50] G. F. Engen and C. A. Hoer, "Thru-reflect-line: An improved technique for calibrating the dual six-port automatic network analyzer," IEEE Trans. Microwave Theory Tech., vol. MTT-27, no. 12, pp. 987–993, Dec. 1979.

[51] R. B. Marks, "Formulations of the basic vector network analyzer error model including switch terms," in 50th ARFTG Conf. Dig., Portland, OR, U.S.A., Dec. 1997, pp. 115–126.

[52] F. Gardiol, Microstrip Circuits. NY, U.S.A.: John Wiley and Sons, 1994, pp. 78–80.

[53] M. Odyniec, Ed., RF and microwave oscillator design. Norwood, MA, U.S.A.: Artech House, 2002, pp. 35–36.

[54] G. Conciauro, M. Guglielmi, and R. Sorrentino, Advanced Modal Analysis. Chichester, England: John Wiley & Sons, LTD, 2000, pp. 190–193.

[55] G. Matthaei, L. Young, and E. Jones, Microwave filters, impedance-matching networks, and coupling structures. New York, NY, U.S.A.: McGraw-Hill, Inc., 1964, pp. 651–723.

[56] J. Krupka, M. Tobar, J. Hartnett, D. Cros, and J.-M. L. Floch, "Extremely high-q factor dielectric resonators for millimeter-wave applications," IEEE Trans. Microwave Theory Tech., pp. 702–712, Feb. 2005.

[57] A. Gopinath, "Maximum Q-factor of microstrip resonators," IEEE Trans. Microwave Theory Tech., pp. 128–131, Feb. 1981.

[58] P. J. Bell, N. D. Noivik, R. A. Saravanan, N. Ehsan, V. M. Bright, and Z. Popovic, "Flip-chip-assembled air-suspended inductors," IEEE Trans. Adv. Packag., pp. 148–154, Feb. 2007.

[59] G. L. Ragan, Microwave Transmission Circuits, 1st ed., G. L. Ragan, Ed. New York, NY, U.S.A.: McGraw-Hill, 1948.

[60] R. V. Snyder, "New application of evanescent mode waveguide to filter design," IEEE Trans. Microwave Theory Tech., vol. MTT-25, pp. 1013–1021, Dec. 1977.

[61] C. A. Tavernier, R. M. Henderson, and J. Papapolymerou, "A reduced-size silicon micromachined high-Q resonator at 5.7 GHz," IEEE Trans. Microwave Theory Tech., pp. 2305–2314, Oct. 2002.

[62] K. Strohm, F. Schmuckle, B. Schauwecker, J.-F. Luy, and W. Heinrich, "Silicon micromachined RF MEMS resonators," in 2002 Proc. IEEE MTT-S Microwave Symposium Digest, Seattle, WA, U.S.A., June 2003, pp. 1209–1212.

[63] X. Gong, A. Margomenos, B. Liu, S. Hajela, L. Katehi, and W. Chappell, "Precision fabrication techniques and analysis on high-Q evanescent-mode resonators and filters of different geometries," IEEE Trans. Microwave Theory Tech., pp. 2557–2566, Nov. 2004.

[64] S. Hajela, X. Gong, and W. J. Chappell, "Widely tunable high-Q evanescent-mode resonators using flexible polymer substrates," in 2005 Proc. IEEE MTT-S Microw. Symp. Dig., Long Beach, CA, U.S.A., June 2005, pp. 2139–2142.

[65] L. Rigaudeau, P. Ferrand, D. Baillargeat, S. Bila, S. Verdeyme, M. Lahti, and T. Jaakola, "LTCC 3-D resonators applied to the design of very compact filters for Q-band applications," IEEE Trans. Microwave Theory Tech., pp. 2620–2627, June 2006.

[66] C.-Y. Chi and G. Rebeiz, "Conductor-loss limited stripline resonator and filters," IEEE Trans. Microwave Theory Tech., pp. 626–630, Apr. 1996.

[67] J. Papapolymerou, J.-C. Cheng, J. East, and L. Katehi, "A micromachined high-Q X-band resonator," IEEE Microwave Guided Wave Lett., pp. 168–170, June 1997.

[68] M. Hill, J. Papapolymerou, and R. Ziolkowski, "High-Q micromachined resonant cavities in a K-band diplexer configuration," IEE Proc.-Microw. Antennas Propag., pp. 307–312, Oct. 2001.

[69] K. Strohm, F. Schmuckle, O. Yaglioglu, J.-F. Luy, and W. Heinrich, "3D silicon micromachined RF resonators," in 2003 Proc. IEEE MTT-S Microwave Symposium Digest, Philadelphia, PA, U.S.A., June 2003, pp. 1801–1804.

[70] M. Stickel, P. Kremer, and G. Eleftheriades, "High-Q silicon micromachined cavity resonators at 30 GHz using the split-block technique," IEE Proc. Microw. Antennas Propag., pp. 450–454, Oct. 2004.

[71] D. Pozar, Microwave Engineering, 2nd ed. New York, U.S.A.: John Wiley and Sons, Inc., 1998, pp. 300–350.

[72] Ansoft HFSS 9.2.1 User Manual, Ansoft, 2004.

[73] F. Gardiol, Introduction to Microwaves. MA, U.S.A.: Artech House, 1983, pp. 136–142.

[74] A. Brannon, J. Breitbarth, and Z. Popovic, "A low-power, low phase noise local oscillator for chip-scale atomic clocks," in 2005 Proc. IEEE MTT-S Int. Microwave Symp. Dig., Fort Worth, TX, U.S.A., June 2005, pp. 1535–1538.

[75] A. F. Celliers and J. A. G. Malherbe, "Design curves for -3-db branchline couplers," IEEE Trans. Microwave Theory Tech., vol. MTT-33, no. 11, pp. 1226–1228, Nov. 1985.

[76] J. Lange, "Interdigitated stripline quadrature hybrid," IEEE Trans. Microwave Theory Tech., vol. MTT-17, no. 12, pp. 1150–1151, Dec. 1969.

[77] R. Waugh and D. LaCombe, "'Unfolding' the lange coupler," IEEE Trans. Microwave Theory Tech., vol. MTT-20, no. 11, pp. 777–779, Nov. 1972.

[78] K. Sachse and A. Sawicki, "Quasi-ideal multilayer two- and three-strip directional couplers for monolithic and hybrid MICs," IEEE Trans. Microwave Theory Tech., vol. 47, no. 9, pp. 2339–2345, Sept. 1999.

[79] C.-Y. Chi and G. Rebeiz, "Design of lange-couplers and single-sideband mixers using micromachining techniques," IEEE Trans. Microwave Theory Tech., vol. 45, no. 2, pp. 291–294, Feb. 1997.

[80] R. Chadha and K. C. Gupta, "Compensation of dicontinuities in planar transmission lines," IEEE Trans. Microwave Theory Tech., vol. MTT-30, no. 12, pp. 2151–2156, Dec. 1982.

[81] S.-C. Wu, H.-Y. Yang, N. G. Alexopoulos, and I. Wolff, "A rigorous dispersive characterization of microstrip cross and t junctions," IEEE Trans. Microwave Theory Tech., vol. 38, no. 12, pp. 1837–1844, Dec. 1990.

[82] C. Person, L. Carre, E. Rius, J. P. Coupez, and S. Toutain, "Original techniques for designing wideband 3D integrated couplers," in 1998 Proc. IEEE MTT-S Int. Microwave Symp. Dig., vol. 1, Baltimore, MD, U.S.A., June 1998, pp. 119–122.

[83] S.-F. Chang, J.-L. Chen, W.-L. Chen, and H.-P. Hwang, "A new MMIC broadside coupler using an array of air-bridges for directivity enhancement," IEEE Microwave Wireless Compon. Lett., vol. 14, no. 6, pp. 304–306, June 2004.

[84] W. P. Ou, "Design equations for an interdigitated directional coupler," IEEE Trans. Microwave Theory Tech., vol. MTT-23, no. 2, pp. 253–255, Feb. 1975.

[85] D. D. Paulino, "Design more accurate interdigitated couplers," Microwaves, pp. 34–38, May 1976.

[86] V. Teppati, M. Goano, and A. Ferrero, "Conformal-mapping design tools for coaxial couplers with complex cross section," IEEE Trans. Microwave Theory Tech., vol. 50, no. 10, pp. 2339–2345, Oct. 2002.

[87] J. W. Osenbach, M. Dautartas, E. Pitman, C. Nijander, M. Brady, R. Schlenker, T. Butrie, S. Scrak, B. Auker, D. Kern, S. Salko, D. Rinaudo, C. Whitcraft, and J. F. Dormer, "Low cost/high volume laser modules using silicon optical bench technology," in Proc. 48th Electronic Components and Technology Conf., Seattle, WA, U.S.A., May 1998, pp. 581–587.

[88] M. C. Wu, "Micromachining for optical and optoelectronic systems," Proc. IEEE, vol. 85, no. 11, pp. 1833–1856, Nov. 1997.

[89] D. W. Sherrer, N. Brese, J. Fisher, C. Gaebe, N. A. Heiks, J. Getz, J. Rasnake, and E. S. Simon, "Wafer level packaging technology for 10 Gbps TOSAs," in Proc. 55th Electronic Components and Technology Conf., Lake Buena Vista, FL, U.S.A., 2005, pp. 1325–1332.

[90] C. Schuster, D. M. Kuchta, E. G. Colgan, G. M. Cohen, and J. M. Trewhella, "Packaging design and measurement of 10 Gpbs laser diode on high-speed silicon optical bench," in 12th IEEE Topical Meeting on Electrical Performance of Electronic Packaging, Princeton, NJ, U.S.A., Oct. 2003, pp. 63–66.

[91] R. S. Tucker and D. J. Pope, "Circuit modeling of the effect of diffusion on damping in a narrow-stripe semiconductor laser," IEEE J. Quantum Electron., vol. QE-19, no. 7, pp. 1179–1183, July 1983.

[92] S.-S. Park, M. K. Song, S. G. Kang, and N. Hwang, "High frequency modeling for 10Gpbs DFB laser diode module packaging," in Proc. 46th Electronic Components and Technology Conf., Orlando, FL, U.S.A., 1996, pp. 884–887.

[93] J. Lee, S. Nam, S. H. Lee, and J. Jeong, "A complete small-signal equivalent circuit model of cooled butterfly-type 2.5 Gbps DFB laser modules and its application to improve high frequency characteristics," IEEE Trans. Adv. Packag., vol. 25, no. 4, pp. 543–548, Nov. 2002.

[94] B. M. Notaros, M. Djordjevic, and Z. Popovic, "Generalized CoCo antennas," in Antenna Applications Symposium, Monticello, IL, U.S.A., Sept. 2006.

[95] D. Sherrer and J. Fisher, "Coaxial waveguide microstructures and the method of formation thereof," U.S. Patent US2004/0 263 290A1, Dec. 30, 2004.

[96] Y.-H. Chun, J.-Y. Moon, B.-S. Ko, T.-J. Baek, S.-C. Kim, B.-O. Lim, J.-K. Rhee, and D.-H. Shin, "A novel V-band 90° hybrid using surface micromachining technology," Microwave Opt. Technol. Lett., vol. 48, no. 04, pp. 770–771, Apr. 2006.

[97] I. Llamas-Garro and A. Corona-Chavez, "Micromachined transmission lines for millimeter-wave applications," in 2006 Proc. Of IEEE CONIELECOMP, Mexico, Feb. 2006, pp. 15–20.

[98] X. Gong, A. Margomenos, B. Liu, W. Chappell, and L. Katehi, "High-Q evanescent-mode filters using silicon micromachining and polymer stereolithography (SL) processing," in 2004 Proc. IEEE MTT-S Microwave Symposium Digest, Fort Worth, TX, U.S.A., June 2004, pp. 433–436.

[99] V. Teppati, M. Goano, A. Ferrero, V. Niculae, A. Olivieri, and G. Ghione, "Broad-band coaxial directional couplers for high-power applications," IEEE Trans. Microwave Theory Tech., vol. 51, no. 3, pp. 994–997, Mar. 2003.

[100] K. Sachse, A. Sawicki, and G. Jaworski, "Theoretical and experimental investigations of a bilevel Lange coupler," in 1998 Proc. 12th Int. Microwave Radar Conf., vol. 1, Krakow, Poland, May 1998, pp. 32–36.

[101] C. H. Cox III, E. I. Ackerman, G. E. Betts, and J. L. Prince, "Limits on the performance of rf-over-fiber links and their impact on device design," IEEE Trans. Microwave Theory Tech., vol. 54, no. 2, pp. 906–920, Feb. 2006.

[102] K. Sato, S. Kuwahara, Y. Miyamoto, and N. Shimizu, "40 Gbit/s direct modulation of distributed feedback laser for very-short-reach optical links," Electron. Lett., vol. 38, no. 15, pp. 816–817, July 2002.

[103] J. Schlafer and R. B. Lauer, "Microwave packaging of optoelectronic components," IEEE Trans. Microwave Theory Tech., vol. 38, no. 5, pp. 518–523, May 1990.

[104] D. Swanson and W. Hoefer, Microwave circuit modeling using electromagnetic field simulation. Norwood, MA, U.S.A.: Artech House, Inc., 2003, pp. 193–196.

[105] D. Kajfez and P. Guillon, Eds., Dielectric Resonators, 2nd ed. Tucker, GA, U.S.A.: Noble Publishing, 1998.

[106] J. Brauer and G. Lizalek, "Microwave filter analysis using a new 3-D finite-element modal frequency method," IEEE Trans. Microwave Theory Tech., pp. 810–818, May 1997.

[107] D. Kajfez and E. Hwan, "Q-factor measurement with network analyzer," IEEE Trans. Microwave Theory Tech., pp. 666–670, July 1984.

[108] R. Roberts, Low phase noise microwave oscillator design. Boston, MA, U.S.A.: Artech House, 1991.